Published in final edited form as:
IEEE Trans Magn. 2010 July 1; 46(7): 2523–2558. doi:10.1109/TMAG.2010.2046907.

Biomedical Nanomagnetics: A *Spin* Through Possibilities in Imaging, Diagnostics, and Therapy

Kannan M. Krishnan
Department of Materials Science, University of Washington, Seattle, WA 98195-2120 USA

Abstract

Biomedical nanomagnetics is a multidisciplinary area of research in science, engineering and medicine with broad applications in imaging, diagnostics and therapy. Recent developments offer exciting possibilities in personalized medicine provided a truly integrated approach, combining chemistry, materials science, physics, engineering, biology and medicine, is implemented. Emphasizing this perspective, here we address important issues for the rapid development of the field, i.e., magnetic behavior at the nanoscale with emphasis on the relaxation dynamics, synthesis and surface functionalization of nanoparticles and core-shell structures, biocompatibility and toxicity studies, biological constraints and opportunities, and *in vivo* and *in vitro* applications. Specifically, we discuss targeted drug delivery and triggered release, novel contrast agents for magnetic resonance imaging, cancer therapy using magnetic fluid hyperthermia, *in vitro* diagnostics and the emerging magnetic particle imaging technique, that is quantitative and sensitive enough to compete with established imaging methods. In addition, the physics of self-assembly, which is fundamental to both biology and the future development of nanoscience, is illustrated with magnetic nanoparticles. It is shown that various competing energies associated with self-assembly converge on the nanometer length scale and different assemblies can be tailored by varying particle size and size distribution. Throughout this paper, while we discuss our recent research in the broad context of the multidisciplinary literature, we hope to bridge the gap between related work in physics/chemistry/engineering and biology/medicine and, at the same time, present the essential concepts in the individual disciplines. This approach is essential as biomedical nanomagnetics moves into the next phase of innovative translational research with emphasis on development of quantitative *in vivo* imaging, targeted and triggered drug release, and image guided therapy including validation of delivery and therapy response.

Index Terms

Biomedical engineering; diagnostics; imaging; magnetic relaxation; nanotechnology; small particles; superparamagnetism; therapy

I. Introduction

TWO of the many grand challenges in biomedicine are to detect disease at the earliest possible time, prior to its ability to cause damage, and to deliver treatment at the right place, at the right dose and at the right time. The former requires advances in diagnostics and imaging and the latter would benefit from new modalities of treatment including targeted drug delivery, possibly, with a triggered release. In this context, it is worth mentioning that targeted delivery

Corresponding author: K. M. Krishnan (kannanmk@u.washington.edu).

Color versions of one or more of the figures in this paper are available online at http://ieeexplore.ieee.org.

would minimize adverse toxicity when compared to general intravenous administration where the chemotherapeutic agents, in spite of being very toxic, are delivered at ~ 10–100 ppm level to the regions of interest [1]. In addition, another ongoing challenge in biomedical nanoscience is to build from the "bottom up", especially *in vivo*, a complex hierarchy of structures using nanoscale building blocks. The physical principles of this process of self-assembly that nature does so well—transforming the genetic code (DNA) into the fundamental biological building blocks (cells) and then constructing the complete organism—is, as yet, not well understood. Here, we comprehensively address these issues emphasizing the use of magnetic nanoparticles that can be synthesized with high monodispersity, exploiting their size-dependent physical characteristics, functionalized for biocompatibility and their magnetic properties optimized to combine both therapeutic and diagnostic (hence, called *theranostic* probes in personalized medicine) functionalities.

In general, current synthetic protocols allow the size range of nanoparticles to be selectively tailored to enable very high levels of interaction with a variety of biomolecules. For example, nanoparticles can bind to a single or a small number of biological entities such as proteins (5–50 nm), genes (10–100 nm) and viruses (20–450 nm). They can also interact with a single cell-receptor or penetrate cells (10–100 μm). Further, magnetic nanoparticles provide unprecedented levels of new functionality. For example, by manipulating magnetic nanoparticles with external field gradients, applications can be opened up in guided transport/delivery of drugs and genes, as well as immobilization and separation of magnetically tagged biological entities. Magnetic nanoparticles also resonantly respond to an alternating or time-varying magnetic field. The Brownian relaxation of larger particles can be used for biological sensing or triggered drug release and exploiting the Néel relaxation of superparamagnetic [2] particles is an effective way to heat up the nanoparticles and the surrounding tissue by transferring energy to them from the external magnetic field. In this way, localized heat can be delivered to targeted sites such as tumors; a form of cancer therapy called hyperthermia [3]. Alternatively, such heating can be combined with chemotherapy or radiation [4], for a mild increase in tissue temperature is known to enhance the destruction of malignant cells and thereby increase the effectiveness of the chemo-radiation treatment while minimizing dose [5]. These are a few of the many possibilities (Fig. 1) that magnetic nanoparticles offer as imaging, diagnostic and therapeutic tools in biomedicine [6]–[10] as well as in other areas of life sciences [11], [12].

Ultimately, to address the first grand challenge in biomedicine, mentioned earlier, it is important to develop approaches for the earliest detection and monitoring, *in vivo*, of markers for cancer and other disease such as atherosclerosis. Presently, clinical imaging methods lack the spatial resolution for early detection based purely on lesion anatomy. Hence, all the imaging methods use a contrast enhancement agent, comprised of a signal amplifying material conjugated to a targeting agent, to identify molecular markers expressed by specific malignancies. Contrast agents based on nanoparticle technologies are candidates for these molecular imaging modalities and especially, have been shown to be very effective in magnetic resonance imaging applications. For example, highly lymphotropic superparamagnetic nanoparticles have been used in MRI imaging to reveal [13] small nodal metastases in patients with prostate cancer not detectable by any other non-invasive methods. Similarly, targeted nanoparticles were used for quantitative imaging with MRI of sparse molecular epitopes [14]. Finally, magnetic nanoparticles with dual functionality—cross-linked iron oxide combined with a near-infrared optically detectable fluorochrome—were used for preoperative and intra-operative imaging of a brain tumor [15]. Broadly speaking, these approaches form the basis of the emerging discipline of molecular imaging [16] which can be defined as the "visual representation, characterization and quantification of biological processes at the cellular and sub-cellular level within intact living organisms" and the images produced reflect cellular and molecular pathways and *in vivo* mechanisms of disease present in environments

that are physiologically authentic. In this context, details of contrast enhancement in magnetic resonance imaging and the emerging technique of magnetic particle imaging are also discussed in later sections (Section VI).

Magnetic materials are known to play a significant role in biology [17] and medicine [18]. Biochemically precipitated magnetite [19], also known as biogenic magnetic nanoparticles, has been found in tissues of various organisms including bacteria, algae, insects, birds and mammals. Many of these diverse organisms use biogenic magnetite to sense the earth's magnetic field for orientation and navigation [20]; however, the details of such magnetoreception [21] are still in debate. Complementing these biogenically synthesized magnetic nanoparticles, beginning in the 1960s when the first stable ferrofluids was prepared in the laboratory [22], numerous chemical methods for their size-controlled synthesis in either organic or polar solvents have been developed [23]–[26]. We shall address the chemical synthesis of magnetic nanoparticles and core-shell structures, emphasizing their design (Section III) and surface functionalization (Section V). Before that, in Section II, we introduce some general concepts of nanoscience and nanotechnology and review size-considerations both in terms of magnetic behavior and biological constraints. These nanoparticles are an excellent system to illustrate a key point in the physics of self-assembly: the convergence of competing energies on the nanometer lengths scale and how the self-assembly process can be controlled by a single parameter, i.e., nanoparticle size and distribution (Section IV). Finally, biomedical applications, including diagnostics, therapy and imaging, are discussed in Section VI.

II. Nanomagnetism in the Context of Biomedicine

A. Brief Remarks on Nanoscience and Nanotechnology

Over the past decade, nanoscience and nanotechnology has captured the imagination of scientists, engineers, governments, funding agencies, investors, industry, and the public alike [27]. There is much hyperbole: for example, cars (Tata Nano in India), retail chains (Nano Universe in Japan) and even microfabricated nanotoilets [28] have all been associated with the term nano. From a scientific point of view the principal question to ask is, when does miniaturization become nanoscience and nanotechnology? Or, as we make the size smaller, are there characteristic length scales below which phenomena, normally observed in macroscopic dimensions, would be substantially different? In general, to answer this question we could look at three representative phenomena: quantum, electrostatic and magnetic behavior of materials. It is well known in quantum mechanics [29] that the ideal model of a "particle in a box" gives rise to energy level spacings, $3h^2/8ml^2$ (where h is the Planck constant and m is the mass of the particle) that are inversely proportional to the size, l, of the box. Setting these energy level spacings of the order of the thermal energy, k_BT, (25 meV at room temperature), we get a characteristic size $l^* \sim 7$–10 nm. In fact, this model has been readily applied to semiconductor quantum dots that can be synthesized to emit colors across the entire range of the visible spectrum [30]. Similarly, when objects are made very small there is an energy associated with transferring a single electron to them. This charging energy, called Coulomb blockade [31], is given by $2e^2/\varepsilon d$ where d is the diameter of the particle. Again, setting this energy of the order of k_BT, we get $d^* \sim 9$ nm. Lastly, of particular relevance to this paper, magnetic moments can be destabilized by thermal energy, a phenomenon referred to as superparamagnetism. The spin-flip energy barrier for such reversal is proportional to the volume (see next section). Again, at room temperature and typical measurement times of 100 s, we can obtain a characteristic radius, $a^* \sim 5$ nm or diameter, $d^* \sim 10$ nm; note that the nanoparticles we synthesize for biomedical applications (Section III) are in this size range.

An alternative, thought-provoking way to define the length scales where nanoscience and nanotechnology become operative is to look at traditional disciplines. On some reflection, it

is clear that below a critical length scale, say ~ 10 nm, it is difficult to distinguish between what is, for example physics, chemistry or biology. Perhaps, it makes sense to suggest that it is precisely this length scale, below which it is difficult to distinguish between traditional disciplines, where nanoscience and nanotechnology are predominant. Nevertheless, as will be illustrated in the rest of this paper, to carry out significant work in biomedical nanomagnetics, it is imperative to have a multidisciplinary perspective and bring a coordinated expertise in physics, chemistry, biology, materials science, etc., to the problem at hand. In this spirit, we will start by discussing magnetic behavior as a function of size, including superparamagnetism, and then address size-constraints in biology, in the context of *in vivo* biomedical applications.

B. Superparamagnetism and Size-Dependent Magnetic Behavior

There are clearly two limits to magnetic behavior of materials as a function of size and dimensionality. At one end of the spectrum (bulk) the microstructure determines the magnetic (hard and soft) behavior. Generally, the microstructure is a function of the processing method and our understanding of it is qualitative and empirical at best. At the other end, as the length scales approach the size of domain wall-widths (nanostructures), lateral confinement (shape and size) and inter-particle exchange effects dominate, until finally, at atomic dimensions quantum-mechanical tunneling effects are expected to predominate [32].

Considering only dipolar interactions between magnetic particles, the spin-flip barrier for a small magnetic object [34] is a product of the square of the saturation magnetization, M_s and its volume ($V \sim a^3$).

Thus, for small volumes the magnetic reversal energy is small enough that the moment becomes unstable, or thermally activated. As a first approximation of this characteristic size, one can set the simple magnetization reversal energy equal to the thermal energy, i.e., $M_s^2 a^3 \sim k_B T \sim 25$ meV at room temperature, and for typical ferromagnets obtain a characteristic length $a \sim 5$–10 nm, below which ferromagnetic behavior gives way to superparamagnetism (Fig. 2(a)). In practice, this length is found to vary among different materials. In real materials, changes in magnetization direction occur via activation over an energy barrier and associated with each type of energy barrier is a different physical mechanism and a characteristic length. These fundamental lengths are the crystalline anisotropy length ($l_K \sim \sqrt{J/K}$), the magnetostatic length ($l_s \sim \sqrt{J/(2\pi M_s^2)}$) and the applied field length ($l_H \sim \sqrt{2J/H M_s}$). Here J is the inter-atomic exchange, K is the anisotropy constant of the bulk material and H the applied field. In principle, if multiple barriers are present, for a given time, the one with the shortest characteristic length determines the material's properties [35]. For a general anisotropy, K, a characteristic time for reversal, τ, is determined as $\tau \sim \tau_0 \exp(KV/k_B T)$; see Fig. 2(b). If the measurement time (typically 100 s) is considered, one can then determine a characteristic size (V_{sp}) at room temperature or, for a given volume, a characteristic temperature called the blocking temperature, T_B, that defines a transition from ferromagnetic to a thermally unstable or superparamagnetic behavior (Fig. 2(c)). For slightly larger particles, it is also important to consider what is the critical size that determines whether it is favorable to be uniformly magnetized (single domain), or to break into multiple domains to minimize their overall energy. Using theories for domain stability in fine particles [36] and bulk properties available in the literature, one can determine the characteristic size up to which single domains are stable [37]. This series of magnetic “phases” as a function of size is shown (Fig. 3) for different ferromagnets and includes a “single domain” size (D_{sd}) below which the material will not support a multi-domain particle [38] and a size (D_{sp}) defined by the superparamagnetic effect [39] below which a spontaneous flip in magnetization occurs due to thermal effects at room temperature.

C. Biological Constraints and Opportunities

For *in vivo* applications, it is important that magnetic nanoparticle formulations have the ability to overcome the main biological barriers that prevent them from reaching their targets [40]. Examples of such barriers include the protective exclusion by the blood-brain barrier [41] or the vascular endothelium; the typically higher osmotic pressure [42] in cancer lesions causing the outward flow of any therapeutic agents and the clearance from circulation by the reticulo-endothelial system (RES) [43]. Like macroscopic biomaterials [44], host and material response is a concern for nanoparticles and their surfaces. Interestingly, in some areas these constraints have enabled easy targeting, for example in the liver and kidneys, due to size-selective filtering by these organs.

Cells are the building blocks of biology and even though they are tens of microns in size, their interactions with external objects, such as nanoparticles, take place at their extremities, i.e., the cell walls. The cell walls or the plasma membranes are bilipid layers, typically ~5–10 nm in thickness. The transport of objects such as nanoparticles into the cells may be accomplished by the formation of vesicles, derived from folds or invaginations of the plasma membrane. These processes, broadly classified as endocytosis [45] (uptake of fluids, dissolved solutes and suspended macromolecules) and phagocytosis [46] (uptake of particulate matter, with specialized cells capable of "eating" particles as large as 0.5 μm in diameter), have to be considered, especially for *in vivo* applications. In most animals/mammals, phagocytosis is a protective/policing mechanism, where a variety of phagocytes, including macrophages and neutrophils, wander through the blood and tissue and phagocytize invading organisms, dying cells and debris, including any nanoscale objects introduced through the vasculature. Such mammalian phagocytosis is enhanced by blood-borne factors, such as a family of proteins called opsonins, that *in vivo* not only coat the nanoparticles but signal their presence as well. Such opsonin-tagged particles are then recognized and bound by receptors on the surface of the phagocytes prior to uptake.

A significant benefit of nanoparticles is that they can be injected and circulate for extended periods of time within the vasculature providing access to areas of the body not otherwise accessible. After injection, magnetic nanoparticles circulating within the blood, transfer to the interstitial fluid (extravasations), then to the lymph (drainage) and eventually return to the blood via lymphatic vessels through chains of lymph nodes [47]. The rapid delivery of nanoparticles in the blood to the interstitium of the tissues is also based on diffusion and the sizes of the pores of the capillary; hence, the endothelial cells lining their walls regulate the permeability of the agents. Blood capillaries are different in various organs and may be broadly classified into four categories [48] (Fig. 4). In the brain the endothelial cells lining the vasculature (Fig. 4(a)) are connected with a tight junction (blood brain barrier, BBB) and even small molecular contrast agents cannot diffuse into the extravascular space. This is how the brain protects itself against infection. Therefore, to penetrate the BBB,[1] any nanoscale package (comprised of the nanoparticle core and all molecules functionalized on its surface) has to be extremely small, i.e., of the order of 2 nm (see Section VI-D). The majority of tissues (muscle, skin, lung and connecting tissue) have continuous capillaries (Fig. 4(b)) and particles/molecules larger than 8–10 nm cannot diffuse into these tissues. Charge and concentration further complicate this simple picture. Note that a pore size of ~6 nm, can accommodate a macromolecule of ~20 kDa in size, if it were globular and ~50 kDa if it were a linear-shaped molecule.

[1]Other ways to disrupt the BBB by osmotic means are either biochemical using substances such as bradykinin or physical by high-intensity focused ultrasound pulses. Alternatively, active approaches such as attaching the protein "transferrin" or specific antibodies results in "transcytosis" of nanoparticles through the BBB.

Foreign bodies, such as macromolecules or nanoparticles, less than 50 nm in diameter are filtered and excreted from the kidneys (renal filtering), which have fenestrated capillaries (Fig. 4(c)). Such fenestrated capillaries are also found in gastrointestinal mucosa, endocrine and exocrine glands. Larger particles, diameter >200 nm, are cleared in the liver and spleen where sinusoidal capillaries are present (Fig. 4(d)). In other words, blood filtration by the reticulo-endothelial system (RES) establishes a lower (<50 nm) and upper (>200 nm) bound for nanoparticle circulation. Note that because of its role in blood-filtration, the kidney can be readily, and passively, targeted; i.e., if magnetic nanoparticles, including the functionalized molecules on their surface, are below a critical size they will be automatically delivered to the kidney. Similarly, it is also well known that tumor capillaries are more permeable than continuous capillaries and are nearly fenestrated, enabling indirect tumor targeting and delivery of nanoscale packages. This is known as the enhanced permeation and retention (EPR) effect [49], which refers to the fact that the vasculature supplying cancer lesions may be highly permeable and tumors lack an effective lymphatic drainage system. The EPR effect especially allows nanoparticles in the size range 10–100 nm to preferentially accumulate in tumors and is an emerging strategy for nanoparticle-mediated targeting or delivery [50]. Other approaches for specific cell-targeting include pH-sensitive and thermosensitive liposomes which can selectively release the cytotoxic agents in the targeted area due to local changes [51] in pH (see Section VI-D) or due to forced local heating [52] (hyperthermia).

Conversely, rapid clearance of nanoparticles from circulation can substantially reduce their biomedical functionality. Active clearance of nanoparticles is mainly due to their recognition by macrophages of the mononuclear phagocyte system [53]. Nanoparticles have a large surface to volume ratio and tend to absorb plasma-proteins (opsonization), which are easily recognized by macrophages making them vulnerable to rapid clearance before reaching their target. Negatively charged and essentially neutral particle surfaces provide the largest circulation times [47]. Progress in reducing the rapid clearance and enhancing the circulation time has been achieved by developing coatings of high-density polymers [54] and by the creation of liposomes containing glycoproteins, albumins or derivatives of poly-ethylene-glycol (PEG) [55]. Such PEG-coated nanoparticles (liposomes) are in an intermediate size range. They are small and hydrophilic enough to slow down opsonization and reticuloendothelial absorption, but large enough to avoid renal filtering [56]. The overall size of the nanoparticles (hydrodynamic size), surface charge and functionalization play a large role in their distribution [57] and circulation time [7]; however, these parameters may change upon interaction with blood constituents.

In summary, it is important that magnetic nanoparticle formulations have the ability to overcome the main biological barriers that prevent them from reaching their targets [40]. However, intravenous injection of nanomaterials introduces new concerns such as dosage, distribution and circulation times making their use and development similar to pharmaceuticals. Of consequence to this work are possible changes in magnetic behavior upon injection and interactions with cells such as specific binding and endocytosis. These interactions can also result in nanoparticle agglomeration or regions of high concentration with inter-particle interactions leading to altered magnetic properties; for *in vivo* applications, these should be avoided or, at least, appropriately included in modeling the magnetic behavior. It seems appropriate to learn from nature and design long-circulating magnetic carriers based on healthy erythrocytes (red blood cells) that evade the macrophages of the immune system and transport oxygen over a life span of 100–120 days. Many physicochemical and physiological factors control this long circulation time of red blood cells. These include surface characteristics (surface charge, membrane phospholipids composition, surface antigens) and bulk properties (shape and deformability); for example, red blood cells protect their surface, avoid opsonization and macrophage surveillance with a protective coating of hydrophilic oligosaccharide groups. They are also deformable which allows them to bypass the spleenic filtration process.

Translating these and other microbial surface strategies would be effective in the engineering of long-circulating, macrophage-evading, functionalized magnetic nanoparticles [58].

III. Chemical Synthesis of Magnetic Nanoparticles and Core-Shell Structures

Nanostructured materials in the size-range identified in Fig. 3, which can be considered to be zero-dimensional objects, can be made by three distinct approaches—metallurgy, lithography and chemical synthesis. The metallurgical approach involves the synthesis of alloys by rapid solidification that on subsequent annealing phase segregate with a microstructure on the nanometer length scale. Such an approach is used for preparing very soft [59] or very hard [60] magnets. The former is achieved by creating nanoscale crystallites that are randomly oriented but interact strongly to give a very small effective anisotropy by directional averaging. On the other hand, large anisotropies and coercivities very close to the theoretical maximum can be obtained by creating isolated magnetic nanostructures dispersed in a non-magnetic matrix [61]. For biomedical applications, where isolated nanoparticles in free form are required, such metallurgical methods are not very attractive. The alternative, well-known method to create nanoscale objects is by lithography. This top-down approach, carried out with either electrons or photons, is both time consuming and expensive but recent developments in nanoimprint lithography (NIL) [62] using prefabricated stamps, appropriate deposition, followed by particle release hold much promise, especially for making synthetic antiferromagnetic particles [63] of any shape, incorporating multiple layers and with size >100 nm. The third approach, discussed here, is to chemically synthesize nanoparticles, including a wide-range of metals, alloys, core-shell structures or oxides, and this can now be carried out with a high degree of reproducibility with control of size, shape, narrow size-distribution and morphology to obtain tailored magnetic properties.

Biomedical applications require magnetic particle cores with several well-defined and reproducible structural, physical, chemical and pharmacological properties. In general, the requirements include: (i) non-toxic material (ii) good response to an applied static/dynamic field tailored for the specific application, (iii) negligible remanence to ensure minimal or no magnetic interactions and agglomeration when the external field is switched off, (iv) well-defined size, monodispersity and preferably, the smallest size possible because smaller particle have larger "total" surface areas for functionalization, (v) good structural and chemical stability under different *pH* and redox conditions, (vi) ease of production and (vii) minimal cost. Further, the surface of the particles should, when necessary, be modified to (a) stabilize the colloidal dispersions, (b) ensure biocompatibility and prevent non-specific interactions with the medium and, (c) facilitate the attachment of functional groups that are necessary for applications based on interactions ranging from non-specific (ionic, hydrophobic/hydrophilic, hydrogen bond), through group-specific (chelating, dye ligand) to specific-affinity (avidin-biotin, antigen-antibody, enzyme-inhibitor, etc.) interactions. The design, chemical synthesis and development of such optimized magnetic particles, or nanovectors [64], for biomedical diagnostics and therapy are discussed in this section. We begin with Co and $Co_{core}Au_{shell}$ nanoparticles, which are model systems for synthesizing highly monodisperse particles from metal-organic precursors. This is followed by magnetic oxides, mainly magnetite and MnO. The former is the really important nanoparticle for *in vivo* applications in biomedicine. Those familiar with such chemical synthesis, surface functionalization and cytotoxicity, and would like to focus on applications may skip directly to Section VI.

A. La Mer Synthesis of Highly Monodisperse Nanoparticles: Cobalt as a Model System

The classic study by La Mer and Dinegar [65] has shown that the colloidal synthesis of monodisperse nanocrystals consisting of three components (precursors, organic surfactants and solvents) requires a single, temporally discrete nucleation event, followed by the slower, controlled growth on existing nuclei. The principal advantage of this method is that highly

monodisperse nanoparticles are synthesized; the main disadvantage is that the synthesis is carried out in organic, non-polar solvents and the particles are hydrophobic requiring a further phase transfer to make them hydrophilic. The required growth parameters can be achieved by the rapid addition of reagents (precursors) into a hot coordinating solvent containing surfactants (Fig. 5(a)). The temperature is kept high enough to decompose the reagents, transforming them into active atomic or molecular species (monomers) with concentration above the nucleation threshold. This supersaturation is relieved by a short burst nucleation of nanocrystals. Upon nucleation the concentration of monomers in solution drops below the critical concentration for nucleation; the existing nuclei then grow by the incorporation of additional monomers present in the solution. For crystalline nanocrystals to form in this thermolysis process, the constituent atoms should be able to rearrange, overcome thermal barriers, and anneal during the growth. Hence, the temperature for growth of the nanocrystals must be chosen to be high enough to promote this atomic rearrangement and annealing. However, nanocrystals melt [66] at substantially lower temperatures (reduction of the melting temperature, T_M, by a factor of 1/2, compared to the bulk, is often observed for nanocrystals 2–3 nm in diameter) which is driven by the fact that in the nanoscale the surface energy of the liquid phase is much smaller than the corresponding solid with crystallographic facets, edges or corners. Thus, inorganic colloidal nanocrystals can be grown at substantially lower temperatures where organic molecules such as surfactants are stable. For this synthesis to be effective, appropriate precursors such as organometallic compounds, that rapidly decompose to produce monomers, need to be identified. The best precursors are simple molecules (e.g., metal carbonyls) with “leaving groups” (e.g., CO) that readily depart leaving behind the desired monomers. Another important parameter influencing crystal growth is the strength with which the surfactant molecules adhere to the surface of the growing crystal [67]. The adhesion should be strong enough to protect the crystals with a monolayer coating, on average, to prevent them from agglomeration but, locally, weak enough to allow the surfactant to exchange on and off the surface of the growing crystal [68]. The latter ensures that regions of the surface of the crystal are accessible for growth. Examples of such surfactants that “dynamically solvate” the new crystal include alkyl phosphine oxides, alkyl phosphinic acids, fatty acid and amines and some nitrogen containing aromatics. In addition, the surfactants form complexes with the reactive monomer species. The diffusion rate and stability of these complexes in solution, as well as the adhesion of the surfactants to the growing nanocrystal surface are both temperature dependent. Hence, choosing the right temperature is key to controlling the growth of the nanocrystals. The variation in growth rate as a function of size has been studied in detail [69]. For small sizes with very high surface energies, the crystals are unstable due to the large number of surface atoms and lead to negative growth. At large sizes, with small surface/volume ratios, the crystals are stable and grow. The critical size, where the crystals neither grow nor shrink, depends on the concentration of monomers, with high monomer concentrations forming smaller sizes. The peak in growth rate with size is simply an effect of the geometric factor (growth of larger crystals require the incorporation of many more atoms compared to smaller crystals). Moreover, if the monomer concentration is high, smaller crystals will grow more rapidly than larger ones. This leads to a spontaneous narrowing of the size distribution; a process called size-distribution focusing [70] that has been well demonstrated in experiments [71].

In general, to obtain monodisperse nanocrystals, it is desirable to temporally separate the nucleation from the growth step (Fig. 5(b)) and essentially, the nucleation must occur on a short time scale (as in the rapid injection of precursors). Alternatively [72], such synthesis can also be accomplished by mixing the reagents at a temperature low enough to preclude any reaction. Then the chemical reaction is accelerated by the increase in solution temperature at a controlled rate to achieve the required supersaturation, which is followed by the burst nucleation. The temperature is then adjusted to keep the rate at which the reagents react to be less than the rate at which the material is added to the existing nuclei. Thus the supersaturated

state is never revisited and there is no further nucleation. Again, as in the injection method, the size distribution of the nanocrystals is limited by the short time period during which the nuclei are formed. Adjusting the reaction conditions, which include time, temperature and concentrations of surfactants and precursors, in a systematic way allows good control of the crystal structure [73] and nanocrystal size in the synthesis. In general, tailoring the ratio of the concentration of precursors to that of the surfactant controls the size since a high surfactant/precursor ratio favors the formation of a larger number of smaller nuclei and thus a smaller nanocrystal size. Alternatively, the particle size can also be controlled either by the binding strength or the steric bulkiness of the surfactant stabilizer. Short chain surfactants (e.g., tributylphosphines) allow faster growth resulting in bigger particles while bulkier ones (e.g., trioctylphosphines) slow the rate of materials being added to the nanocrystals leading to smaller size. Similarly, using a pair of surfactants, one (e.g., carboxylic acid) which binds tightly to the nanocrystal surface and hindering growth and the other (e.g., alkylphosphine) binding weakly and promoting growth, has also been shown to be an effective way to control size.

When carbonyls are decomposed in the presence of stabilizing surfactants, in the limit of slow growth rates under thermodynamic control, equilibrium nanocrystals with spherical shapes (Fig. 5(c)) and broad size distributions are formed. Many such systems also exhibit a second growth phase called Oswald ripening [74] where the high surface energy of the small particles promote their dissolution and the materials are re-deposited on the larger nanocrystals. This also increases the size distribution. If the growth rate is further increased beyond this focusing regime, nanocrystals with a variety of anisotropic shapes (such as disks, rods, etc.) are formed [75], [76]. Such kinetic control of shape [77] can be further facilitated using selective adhesion of surfactants [78]. The rate of adhesion of surfactants and their dynamic exchange rate in solution are different for different crystallographic faces of a faceted crystal. Organic molecules that preferentially adhere to specific crystallographic planes can be used to modify their relative growth rates when compared to the rest resulting in anisotropic shapes. This approach has been demonstrated [26] for the growth of *hcp* cobalt disks (Fig. 5(d)) by injecting cobalt carbonyl into a mixture of trioctylphosphine oxide (TOPO) and oleic acid. At a fixed oleic acid concentration, the diameter of the nanodisk is proportional to the concentration of TOPO. High-resolution electron microscopy images (Fig. 5(e)) show that the short direction of the nanocrystal is along the (0001) direction of the *hcp* cobalt crystal, demonstrating that TOPO stabilizes the non-basal planes and decreases their growth rates. A much simpler process to generate such cobalt nanodisks using a linear amine, instead of TOPO, has also been developed [79]. In summary, in such thermal decomposition synthesis the surfactants play a critical role in controlling the final morphology of the nanoparticles (details can be found elsewhere) [67].

B. Synthesis of Magnetic Oxide Nanoparticles

Iron oxides are a well-studied magnetic material for use in biological applications and their biocompatibility has been well documented [80], [81]: acute and chronic studies show no hepatotoxicity (damage to the liver and a parameter used to determine toxicity of drugs) in rats receiving large dosages of iron oxide particles [82]. Iron oxide nanoparticles, albeit with very large size distributions, are commercially available and have FDA approval for use as MRI contrast enhancers [83]. Metallic and alloy nanoparticles have very good structural and magnetic properties; however, in addition to being susceptible to oxidation, which substantially changes the magnetic characteristics, their enhanced toxicity also prevents them from being considered for *in vivo* applications [84]. On the other hand, ferrimagnetic oxides of iron, $\gamma - Fe_2O_3$ (maghemite) and Fe_3O_4 (magnetite), are biocompatible and in various stages of clinical trials [85], primarily as MRI contrast agents, and a number of successful methods have been developed to prepare them as nanoscale particles. A common preparation method is Massart's co-precipitation [86] of Fe^{2+} and Fe^{3+} by a base, such as NaOH, in an aqueous solution [87].

This method has the advantage of being able to prepare large quantities but is limited by the difficulty in tailoring the size or the size distribution of the nanoparticles, as there are only kinetic factors to control in the synthesis. Alternatively, they can be prepared by the thermal decomposition of a solution of Fe^{3+} chelate in the presence of hydrazine [88] or by the sonochemical decomposition of hydrolyzed Fe^{2+} salts followed by heat treatment [89]. These methods are limited by the fact that the pH of the reaction mixture has to be adjusted during both the synthesis and purification stages and the preparation of smaller, superparamagnetic (<20 nm) nanoparticles is difficult. Surfactant molecules in solution spontaneously result in tight spherical aggregates called micelles (diameter ~1–10 nm) or microemulsions (diameter ~10–100 nm). On the outside, these micelles can expose either the hydrophilic part of the surfactant to a polar solvent (direct micelle) or the hydrophobic part to a non-polar solvent (inverse or reverse micelle). In the latter case, formed in a non-polar hydrocarbon solvent, a pool of water can be readily stabilized inside the micelle, resulting in a constrained nanoreactor of a well-defined size for the formation of nanoparticles. Using aerosol or sodium dioctylsulphosucinate as the surfactant system in iso-octane to form reverse micelles, a number of spherical magnetic nanoparticles, including $\gamma - Fe_2O_3$ and Fe_3O_4, with sizes in the range of 5–50 nm and a size-distribution > ±10%, have been prepared by the oxidation of ferrous salts [90], [91]. These methods though very popular, generally produce a broader size distribution.

Alternatively, to prepare highly monodisperse magnetite particles, the solution phase decomposition of iron precursors at elevated temperatures has also been successfully extended to prepare oxide nanoparticles. For example, the rapid injection of an iron cupferrous complex, $FeCup_3$, into trioctylamine at 300°C results in the synthesis of $\gamma - Fe_2O_3$ nanoparticles [94]. Alternatively, the injection and decomposition of iron pentacarbonyl to form monodisperse iron particles, followed by their mild oxidation using trimethylamine N-oxide, results in $\gamma - Fe_2O_3$ nanoparticles with a narrow size distribution [95]. In practice, the injection of $Fe(CO)_5$ is followed by a long incubation period before the nucleation takes place as a sudden burst. This is because $Fe(CO)_5$ in the presence of oleic acid forms a number of intermediate species, which function as the monomer complex [96]. As their concentrations increase beyond the nucleation threshold, burst nucleation takes place and the nuclei then grow into nanocrystals. Interestingly, as a result, this synthesis is more reproducible as it is independent of the rate of the initial rapid injection. Moreover, the synthesis parameters in this two-step process can be modified to produce Fe_3O_4 (magnetite). The size can be controlled by varying the molar ratio of the surfactant (oleic acid) to iron pentacarbonyl (Fig. 6(f)–(h)) with higher ratios of surfactant to iron pentacarbonyl resulting in larger particles. However, higher ratios of surfactant to iron pentacarbonyl also increase the time prior to nucleation. Therefore, higher concentrations of surfactant also cause an increase in the size distribution due to the extension of the nucleation process and limit the maximum size of monodisperse nanoparticles achievable with this method to ~12 nm. To synthesize larger magnetite nanoparticles (~30 nm diameter), an alternative procedure involving the high temperature pyrolysis [97], [222] of the metal fatty acid salt (ferric oleate), the corresponding fatty acid (oleic acid) and a hydrocarbon solvent (octadecene) can also be implemented. This is a two-step process: preparation of ferric-oleate followed by the synthesis of Fe_3O_4 nanoparticles, and produces larger (diameter >15 nm) ferromagnetic particles at room temperature, albeit with a much broader size distribution.

Monodisperse magnetite particles can also be directly synthesized [25] from a high temperature (265°C) reaction of iron acetylacetonate in phenyl ether in the presence of alcohol, oleic acid and oleylamine. Using these smaller magnetic particles as seeds, larger monodisperse magnetite nanoparticles, without any size-selection procedure, up to ~20 nm diameter can be synthesized. The quantity of nanoparticle seeds can be used to control the final size of the magnetite nanoparticles. These as-synthesized Fe_3O_4 nanoparticles, can be transformed either to $\gamma - Fe_2O_3$ by annealing in O_2 or to $\alpha - Fe$ by annealing in a mixture of Ar and H_2.

For reproducible magnetic characteristics, it is important to distinguish between magnetite (Fe_3O_4) and maghemite (Fe_2O_3). It is difficult to unequivocally distinguish between the crystal structures of magnetite and maghemite from standard X-ray $\theta - 2\theta$ scans. However, in addition to channeling methods in electron microscopy [98], [99] the oxidation state of Fe in the nanoparticles can be determined by measuring the electron energy-loss spectrum of the Fe $L_{3,2}$ edge in a TEM (Fig. 6(d)). For the forward scattering geometry in a TEM, dipole selection rules ($\Delta l = \pm 1$) apply. Then, the ratio of the $L_3(2p^{3/2} \rightarrow d)$ to $L_2(2p^{1/2} \rightarrow d)$ transitions is a very good measure of the iron oxidations state [100].

Magnetic nanoparticles synthesized in organic solvents are coated with a layer of surfactants (oleic acid, TOPO, etc.) to keep them stable, but this also prevents the particles from dispersing in aqueous solutions. For biological applications nanoparticles must be water-soluble. A robust protocol [101] for the transfer of oleic acid coated nanoparticles to the aqueous phase with the biocompatible co-polymer, Pluronic F127, has been developed. Phase transfer of nanoparticles is nontrivial as this process may result in agglomeration [102], either due to their strong van der Waals and/or magnetostatic interactions, thereby negating the benefits of the initial monodispersity. The success of the phase transfer protocol can be routinely evaluated by dynamic light scattering (DLS) measurements to ensure that the majority of the particles are individually transferred. For monodisperse nanoparticle transfer, we expect the hydrodynamic radii of the particles to increase by ~23 nm (Fig. 7), corresponding to the typical size of a F127 micelles [103]. Moreover, no changes have been detected in the saturation magnetization of the nanoparticles with values remaining as high as 96% of the theoretical value before and after Pluronic-F127 coating and phase transfer.

The surface coating of nanoparticles is very important in determining their fate for both *in vitro* and *in vivo* applications. Numerous other coatings of amphiphilic molecules are being developed, another example being poly(maleic anhydride-alt-1-octadecene) (PMAO), which consists of alternating hydrophilic-hydrophobic groups in the form of anhydride and 16-carbon length alkane units, respectively [270]. Anhydride rings are bi-functional, they can participate in reaction with mono-amine or hydroxyl terminated poly(ethylene glycol) (PEG) and also hydrolyze in water to release carboxylic acid groups that can be used for bio-conjugations [271]. It is important, for *in vivo* applications, to test the stability of the particles not only in water but also in biological medium (typically, Dulbecco's Modified Eagle Medium (DMEM) with 10% fetal bovine serum (FBS) is used). Further, care should be taken to determine whether the inorganic nanoparticles are individually coated or they are composites consisting of multiple cores. In the latter case, interparticle magnetic interactions can arise and complicate the interpretations/tailoring of their magnetic relaxation dynamics. However, a standardized approach to design nanoparticles, prepared in organic solvents and coated with amphiphilic polymers, for biomedical applications has been recently proposed [272].

C. Core-Shell Structures

The strategies developed for the synthesis of nanoparticles in homogenous solution can be generalized by separating the stages of particle nucleation from its subsequent growth. When the nuclei are different from the available monomer materials, particles composed of binary elements are synthesized provided conditions suitable for heterogeneous nucleation can be generated in solution. Further, depending on the solubility of metals in each other at the reaction temperature, these structures can grow along two different pathways, either by surface diffusion to form a core-shell structure or through inter-diffusion to form alloy particles. The final morphology of such binary particles is dependent on their bulk thermodynamics: for immiscible heterogeneous systems core-shell structures (Fig. 5(f)–(i)) are obtained, while miscible systems lead to alloy nanoparticles [104]. Since the biological applications of ferromagnetic transition metal (e.g., Fe, Co and Ni) nanoparticles are limited by their poor

biocompatibility and resistance to oxidation, preparing them in core-shell morphology may be desirable. One approach to chemical stabilization is the deposition of insulating shells on the nanoparticles surface to prevent the reaction of oxygen with the surface atoms. Usually, an inert silica coating on the surface of magnetic nanoparticles reduces their aggregation in a liquid and improves the chemical stability. At the same time, the silanol surfaces can be modified with various coupling agents to covalently attach specific bioligands to the surfaces of the magnetic nanoparticles [105], [106]. In addition to silica, noble metals can also be deposited on the magnetic particles. The advantages of coating gold as the shell on the magnetic core include exceptional stability of aqueous dispersions; easy surface modification that allows the preparation of nonaqueous colloids; easy control of inter-particle interactions, both in solution and within structures through shell thickness. Further, if the shell can provide additional functionality, such as sensitivity to optical probes [107] and other biomolecules, it would be highly desirable for a number of applications.

Chemical synthesis of gold-coated magnetic nanoparticles have been reported by different groups [108]–[111]. However, in addition to reproducibility, the growth processes do not lend themselves to the production of uniformly coated core-shell particles because the synthesis environment is rich in oxygen and the presence of water accelerates the formation of cobalt hydroxide. Moreover, in these methods, the use of a strong reducing agent (borohydride) makes the reduction reaction too rapid to form a uniform shell. It is also possible that instead of forming a shell, individual Au nanoparticles are formed. Using pre-made cobalt nanoparticles as seeds, a gold shell has been grown in solution by slowly reducing a low-reactivity gold precursor with a weak reducer under mild conditions (85–105°C) to form $Co_{core}Au_{shell}$ nanoparticles. The characterization of such $Co_{core}Au_{shell}$ nanoparticles is non-trivial and a number of complementary methods have to be employed to unequivocally confirm the core-shell morphology. For example, the contrast of the particles in routine transmission electron microscopy (TEM) images (not shown)—lighter core and darker shell—suggests the core-shell structure is formed. High resolution TEM imaging show a single crystal Co core uniformly surrounded by multiple gold grains, suggesting that gold has multiple nucleation sites on cobalt seeds during synthesis (Fig. 5(g)). The image clearly shows the structure of the shell, but the core is not well resolved due to it being both in a different crystallographic orientation and embedded inside the thin shell. Lattice spacing of 0.204 nm and 0.102 nm, directly measured from the image, corresponds to fcc Au (002) and (004) planes. An inverse Fourier transform analysis was performed on separate images from different regions of the Au shell, and the projected symmetry of local images fits well to fcc Au structure as well. The observation of Co – $L_{2,3}$ edges in electron energy-loss spectroscopy using a 1 nm probe focused on the core, (and absence of the peak when focused on the shell) can confirm the distinct chemical nature of the core (Co) and shell (Au) [112].

Complementing a detailed TEM analysis, bulk structural and magnetic properties of these nanoparticles can also be investigated, on powder form samples, by X-ray diffraction (XRD) and superconducting quantum interference device (SQUID) magnetometry, and the optical properties, in solution form, by UV-Visible spectrophotometry. The temperature dependent magnetization measurements show a narrow peak at 55 K, suggesting the magnetic size of the particle is about 6 nm with a narrow size distribution by comparing with pure cobalt nanoparticle measurement (Fig. 5(h)). At lower temperatures (5 K) the nanoparticles show hysteresis behavior consistent with the ferromagnetic state (Fig. 5(h), inset). In addition to the intrinsic magnetic properties of the cobalt core, the gold nanoshell brings in unique biocompatibility and near infrared optical activity. The plasmon-derived optical resonance of the gold shell can be dramatically shifted in wavelength from the visible region into infrared over a wavelength range that spans the region of highest physiological transmissivity. From UV-visible spectra, pure Co nanoparticles show a continuous increase in intensity with decreasing wavelength and no peak is observed; pure Au nanoparticles show a characteristic

peak around 530 nm; however, a relatively strong peak at 680 nm was observed for the Au shell absorbance of these Co-Au core-shell nanoparticles (Fig. 5(i)). This red shift from 530 nm to 680 nm compared to similar size individual gold nanoparticles provides a distinct optical signature for these core-shell particles and confirms the existence of the core-shell structures.

Since the activation energy for heterogeneous nucleation is generally lower compared to homogeneous nucleation, in a heterogeneous solution with seed crystals under mild condition, it is preferable for the existing monomers to nucleate on the seeds rather than self-nucleate [113]. However, if the reaction condition is really vigorous, self-nucleation will occur spontaneously. A highly reactive monomer, over-saturated precursor, or a significantly high reaction temperature may also induce this condition. In practice, several aspects have to be considered to synthesize binary nanoparticles. First, low monomer reactivity and concentration is preferred to avoid the occurrence of self-nucleation. Second, the reaction temperature has to be low enough to prevent self-nucleation but high enough to bring the original surfactant coatings on seed surface into a dynamic state, allowing for the occurrence of heterogeneous nucleation. Third, attention has to be paid to the effects of temperature on the inter-diffusion of these two materials. Compared to the homogeneous solution, the activation energy of the nucleation on seeds in a heterogeneous solution is dependent on the wetting angles and the size of the seeds [114]. The wetting angle of gold on a cobalt surface, based on their surface and interfacial energies, is ~ 40°. On a spherical cobalt nanoparticle with a curved surface, optimal nucleation of an Au shell is observed experimentally for cobalt seeds 5–8 nm in diameter [115].

Larger cobalt seeds induce higher heterogeneous nucleation rate, resulting in less control on the growth process of the core-shell nanoparticles. This limitation on synthesizing larger $Co_{core}Au_{shell}$ nanoparticles can be overcome by using an alternative synthesis driven by a displacement reaction on the surface of cobalt nanoparticles (Fig. 8). Here, the surface of the cobalt nanoparticle is sacrificed sequentially as the reducing agent for the gold metal deposition on its surface. Hysteretic magnetic properties of nanoparticles depend critically on their size and since the size of the magnetic core decreases with time in this displacement reaction, magnetic measurements provide a unique and systematic way to monitor the formation of the $Co_{core}Au_{shell}$ morphology. As expected, starting with a ferromagnetic particle, the coercive field can be seen to decrease as the reaction progresses [116].

Another core-shell nanoparticle of interest as a T_1 MRI contrast agent is an MnO nanoparticle core coated with a silica shell. A typical T_1 MRI contrast agent is a high moment, ionic species such as chelated Gd complexes. However, these are difficult to target and do not show any time dependence. $MnO_{core}Silica_{shell}$ can be functionalized for specific targeting (Section V) and the shell can be modified to control the release of Mn^{2+}, over time, at mildly acidic cellular pH (see Section VI-E for details). The synthetic procedure for preparing MnO nanoparticles is a modified version of a method proposed by Park *et al.* [117]. A stock solution of the Mn-surfactant complex was prepared by reacting 0.2 g of $Mn_2(CO)_{10}$ with 2 mL of oleylamine at 100°C. The stock solution was cooled to room temperature and 10 mL of trioctylphosphine was added. The resulting solution was kept at 280°C under vigorous stirring for 1 h. The initial yellowish color of the solution gradually turned brownish black, indicating that nanoparticles were generated. The reaction mixture was then cooled to room temperature and the nanoparticles were obtained by adding ethanol, followed by centrifugation. The nanoparticles could be redispersed in non-polar solvents such as hexane or toluene. The nanocrystals were monodisperse and ~10 nm in diameter as confirmed by TEM (Fig. 9(a), inset). Moreover, the peaks in the XRD $\theta - 2\theta$ scans were indexed as single-phase MnO (Fig. 9(a)). Bulk MnO with the rock salt structure is antiferromagnetic with the Néel temperature, $T_N = 122$ K. However, these single-phase, pure, monosize MnO nanoparticles ~10 nm in diameter show anomalous behavior at low temperature. Scaling analyses [118] of these MnO nanoparticles point at a

spin-glass-like state with the freezing temperature of ~30 K [119]. Further, investigation [120] of these MnO nanoparticles by polarized neutron diffraction with XYZ-polarization analysis revealed no long-range ordering down to 3.5 K. However, a broad magnetic peak appeared close to Q = (1/2,1/2,1/2) signifying short-range antiferromagnetic correlations. The correlation length was found to be about 2.4 nm at T = 3.5 K. The correlation length decreases rapidly with increasing temperature and becomes about 0.7 nm at T = 250 K. DC and AC (100 Hz ≤ f ≤ 10 kHz) magnetic moments were measured in the Quantum Design PPMS. Magnetization curves were measured in fields up to 90 kOe over the temperature range from 10 K to 330 K, and showed spontaneous magnetization, M_s, determined by extrapolating the high-field magnetization back to H = 0, and hysteresis up to ~250 K (Fig. 9(b)). However, taking into account that the moment of Mn^{2+} is $5\mu_B$, the magnitude of M_s indicates that only a small fraction of Mn atoms contribute to M_s: ~1% at T < 30 K and ~0.2% at 50 < T < 250 K. The observation of a ferromagnetic state with the Curie temperature T_C ~ 250 K, considerably higher than the Néel temperature of bulk MnO, may be explained using a hypothesis that defect- (surface-) mediated indirect exchange, similar to that found in dilute magnetic oxides [121], [122] is possible in transition metal oxide nanoparticles. Finally, the MnO nanoparticles were coated with silica using tetraethyl orthosilicate (TEOS) (Fig. 9(c)). The core-shell particles were precipitated with excess hexane and collected by centrifugation [123].

D. Other Synthesis Methods

Several noteworthy biological organisms [19]–[21] have developed an extraordinary ability to direct the molecular-level synthesis of crystalline inorganic materials on the nanometer scale, under environmentally benign and mild reaction conditions, with control over size, shape, crystal structure, chemical composition, orientation and organization. Biologically synthesized nanocrystals are naturally biocompatible and, in addition, the proteinaceous shells or lipid vesicles that enclose the inorganic core provide a readymade platform for surface modification. For example, exposed functional groups such as amino acids can be chemically modified for the attachment of a variety of ligands, including peptides, for specific binding and targeting. However, while such chemical approaches allows the incorporation of a variety of functional groups, genetic approaches for the site-specific functionalization are preferred as they are gentler with respect to the preservation of the protein activity. Broadly, there are two such approaches for the synthesis of magnetic nanoparticles: a biogenic [124] one that is based on culturing and modifying the biomineralization of naturally occurring bacterial magnetosomes [125] and a biomimetic [126] one that entails the utilization of naturally occurring protein cage architectures with high symmetry to act as constrained reaction environments for the synthesis and encapsulation of nanoscale inorganic materials [127]. In the latter case, phage display methodologies have been used for the identification of specific peptide sequences that not only bind but also control the chemistry and morphology of growth of a specific inorganic material. By incorporating these peptide sequences inside the protein cages, controlled growth of a number of magnetic nanocrystals, ranging from ferrimagnetic magnetite to hard magnetic alloys of FePt [128] and CoPt [129], representing the wide range of magnetic properties (from soft to hard), have been demonstrated.

Magnetic nanoparticles with larger moments are often preferred for magnetic sensing and to avoid space restrictions in high magnetic field gradient separators. As we have seen for the chemical synthesis methods, increasing the size of nanoparticles beyond a certain limit (~20 nm) results in a rapid loss of monodispersity. Also, increasing the size of the nanoparticle beyond the critical size for superparamagnetism (Fig. 3) results in the particles having a remanent magnetization causing them to spontaneously aggregate due to magnetostatic interactions. A possible and often-used solution is to incorporate the nanoparticles in a host matrix, such as dextran, to create a larger microsphere [130]. However, this also has limitations

arising from the difficulties in controlling their number-density, monodispersity and magnetic response. An alternative approach is top-down microfabrication, such as nanoimprint lithography [131], that can be used to fabricate monodisperse nanoparticles with tai-lorable magnetic characteristics (strongly magnetic, zero remanence), by patterning ferromagnetic multilayer structures followed by release and stabilization in solution [132]. The in-terlayer magnetostatic interactions can be adjusted to achieve zero-remanence and, in effect, create a synthetic antiferromagnetic nanoparticle.

IV. Self-assembly

All biological organisms are to a large extent self-assembled. In nanoscience and nanotechnology there is also substantial interest in self-assembly as a “bottoms up” manufacturing strategy, which can be accomplished at room temperature and under mild conditions. It is well known that self-assembly requires competing attractive and repulsive weak forces to be deployed in just the right way but a systematic understanding is, as yet, absent. Even though biological self-assembly is quite complex, the underlying physical principles can be understood by studying nanoparticle self-assembly even in polar solvents. Highly monodisperse cobalt nanocrystals, coated with surfactant, are excellent model systems to study the physics of self-assembly. With competing van der Waals (long-range) attractive forces from the polarizable metallic cores, steric repulsion from the surfactant chains, magnetostatic dipolar interactions and entropic or depletion forces, they give rise to an intriguing variety of self-assembly possibilities on varying a single parameter: the nanoparticle size and size distribution. They illustrate very well two of the most important ideas, i.e., the dominant role of weak forces and the convergence of various competing energies (of the order of zepto or 10^{-21} J) that are important in furthering our understanding of the complex self-assembly processes in biology. Note that self-assembly processes require a delicate balance between weak attractive and repulsive forces and are quite different from agglomeration, where the attractive forces dominate. Needless to say, such agglomeration could lead to unintended consequences in *in vivo* applications of magnetic nanoparticles; however, agglomeration can be minimized by using superparamagnetic nanoparticles that have zero remanent magnetization. Finally, self-assembly of magnetic nanoparticles bound to cells has been proposed as a mechanism for tissue engineering. For example, construction and harvesting of multilayered keratinocyte sheets using magnetite nanoparticles has been demonstrated [6] but the details are beyond the scope of this paper.

Self-organization of nanoparticles into ordered monolayers of “crystals” on surfaces is driven by a combination of evaporation, convection and inter-particle interaction forces. As the evaporation front passes over a hydrophilic surface at a controlled rate, the particles dispersed in solution are pulled towards the drying front by convection and then deposited there as the drying front becomes very thin. Capillary forces subsequently pull the particles together into ordered arrays. However, arrays of nanocrystals exhibit a surprising richness in form and symmetry as a function of their size, size-distribution and shape [133]–[135]. Here, we summarize the different arrays observed with Co nanocrystals and interpret our results in terms of critical, but well-defined, inter-particle interactions.

The magnetic behavior of cobalt nanocrystals, including their interactions, plays an important role in determining the self-assembly. Small (diameter, $d < 70$ nm) [136] Co nanocrystals are single domain, i.e., the exchange interaction couples all the atomic magnetic moments, and they can be considered as a single large magnetic dipole. In each nanocrystal this magnetic dipole may favour specific crystallographic orientation depending on its magnetocrystalline anisotropy (cubic ε – Co or uniaxial *hcp* – Co). The magnetocrystalline energy is a product (KV) of the anisotropy constant (K) and the nanocrystal volume (V). When compared to the thermal energy, $k_B T$, it determines the magnetic stability of the nanocrystals; typically the

magnetic relaxation time depends exponentially on the particle volume [137]. As a result, at room temperature, particles smaller than a critical size (diameter <10 nm for Co) have magnetic dipole moments that are free to rotate in any direction (superparamagnetic on the time scale of routine SQUID measurements); in larger particles the magnetic dipole moment is fixed along the easy directions of anisotropy (ferromagnetic). Such ferromagnetic particles, with time constants for rotation in solution shorter than the time for self-organization, favour arrangements that minimize their magneto-static energy arising from the interaction of their magnetic dipoles.

Superparamagnetic ε – Co nanocrystals (diameter ~8–9 nm) assemble into hexagonal close packed 2-D arrays (Fig. 10(b)). This behavior may be explained by the classical first order phase transition (i.e., melting and freezing) as a function of concentration (thermodynamic variable). The total internal energy for this system consists of the sum of the van der Waals, steric repulsion, magnetostatic energy and other second-order terms that include hydrophobic attraction between surfactants. The hydrophobic attraction is negligible in nonpolar solvents, and at room temperature the magnetostatic energy between superparamagnetic particles is also negligible. A preliminary calculation shows that $k_B T$ is on the same order of magnitude (10^{-21} J) as the van der Waals energy. The steric repulsion term (also of the order of $k_B T$) will further reduce the total internal energy. It is then reasonable to assume that $k_B T$ is larger than the total internal energy and the self-assembly of the system can be approximated by the hard-sphere model [138]. Typically, as the solvent evaporates and the volume fraction [139] increases, the particles undergo a first order phase transition, where the thermodynamic variable in concentration and not temperature, and freeze into close-packed, hexagonally ordered arrays.

With rapidly increasing surface to volume ratio we observe that this hard-sphere approximation breaks down for very small ε – Co nanocrystals (~4 nm). The self-assembly is now dominated by the steric forces between the surfactant molecules on their surface and leads to the formation of square nanoparticle arrays (Fig. 10(a)). Oleic acid, with an 18-carbon atom backbone (chain length 2.3 nm), was the surfactant used for stabilization. The observed inter-particle separation (2.5 nm) for these small crystallites is less than twice the theoretical chain length of oleic acid; at equilibrium separation the surfactant tails between neighboring particles are compressed (interpenetrate by 2.1 nm)—a process that would decrease the entropy of the system. For particle sizes of interest and inter-particle distances observed, four-fold is favoured over six-fold coordination to minimize the surfactant-overlap volume. An alternative, but less-likely explanation involves the role of the polyhedral shapes [140], along low symmetry directions such as (625), on the nanocrystal assembly.

On the other hand, a bimodal combination of 4 and 10 nm particles leads to a controlled entropic attraction between larger particles [141]. There are two contributions to the entropy of the system: a configurational component arising from the spatial arrangement of the nanoparticles and a vibrational component dominated by the contribution from the smaller nanoparticles, provided the sums of the volumes of small spheres and large spheres are comparable. To first order, the larger size spheres will then adopt those configurations that maximize the entropy of the small spheres. This can be accomplished either if the large spheres touch each other or if the large spheres preferentially touch the surface (Fig. 10(d)). The former is akin to a fictitious attractive force between larger particles (also called depletion or excluded-volume force) and the latter is equivalent to a preferential “wetting” of the surface by the larger particle. This simple argument[2] predicts a size-dependent segregation of the ordered arrays with the smaller

[2]Alternatively, for heterogeneous mixtures of colloids in solution, size-selective precipitation from kinetic considerations could also contribute to such nanocrystal segregation. Controlled precipitation should determine under which conditions, if any, such kinetic effects become important.

size nanocrystals delegated to the periphery of the hexagonal array of the larger particles. This is indeed observed for the case of our ε – Co nanocrystals with a bimodal size-distribution (Fig. 10(e)). Larger ε – Co particles (~18 nm) are ferromagnetic at room temperature and show open hysteresis loops. Consequently, the collection of particles (each considered as adipole) are observed to self-organize such that the net magneto-static energy is minimized. The dipoles are observed to assemble in a tip to tail linear chain orientation; further, the chains fold into loops in order to close the stray magnetic field (Fig. 10(h)). Electron holography measurements [134] indicate that the field lines are channelled parallel to the particle chains, confirming that the magnetostatic forces dominate and lead to the resulting self-assembled linear arrays (Fig. 10(f), (g)). Similarly, shape and magnetocrystalline anisotropy compete in hcp-cobalt to determine the resulting magnetization direction in disk shaped particles. Our calculations suggest that shape anisotropy is dominant and magnetization lies in the plane of the disk when the thickness to diameter ratio is less than one-half. The magneto-static energy is then minimized when neighboring particles have anti-parallel spins. In practice, nanodisks show lyotropic behavior and a spiral spin-order [142].

V. Functionalization:Specific Targeting, Biocompatibility and Cytotoxicity

All biomedical applications of magnetic nanoparticles arise from the combination of their magnetic properties with biological relationships and phenomena. Naturally, the convergence of these two areas is most pronounced at the surface of the magnetic nanoparticle where it interfaces with its biological environment. By manipulating the nanoparticle surface it is possible to induce a wide range of biological responses, and the importance of the surface functionalization of the magnetic nanoparticles, especially for *in vivo* biomedical applications, cannot be overemphasized. One important example of the potential benefits of combining magnetic properties and tailored surface properties relates to a common problem in cancer therapy, namely that most current anti-cancer agents do not differentiate between cancerous and normal cells [143]. In fact, the inability to administer therapeutic agents such that they selectively reach their targets without any collateral damage has largely accounted for the discrepancy [144] between the tremendous progress made in fundamental cancer biology [145] and its poor translation into the clinic. Current estimates [1] are that only ~ 10-100 ppm of intravenously administered drugs or contrast agents is able to reach their target *in vivo*. Thus, to increase the efficacy per dose of any therapeutic or imaging contrast formulation, it is important to increase its targeting selectivity [146].

A number of ligands have been identified for such ligand-targeted-therapeutics [147] in anti-cancer therapy and the following example illustrates this approach. Extensive and compelling experimental evidence [148] substantiates the critical role that angiogenesis—the process of inducing and sustaining the growth of new blood vessels—in promoting tumor growth. As such, tumor angiogenesis offers a uniquely attractive therapeutic target and, for some time, cancer researchers have worked to starve tumors by blocking angiogenesis with mixed success [149], [150]. However, a class of membrane proteins, $\alpha_v\beta_3$-integrin, is highly over-expressed only on newly growing blood vessels or neovasculature, but not in established ones. Nanoparticle encapsulated liposomes, coated with an appropriate $\alpha_v\beta_3$-binding ligand, such as Tetrac [151] or RGD peptides [152], to target the neovasculature and embedded with a mutant form of the Raf$^{\mu}$ – 1 gene has been shown to disrupt the normal activity of the Raf-1 gene by blocking endothelial signaling and angiogenesis in response to multiple growth factors [153]. An alternative approach is passive cancer targeting through the enhanced permeation and retention (EPR) effect [49]. This is based on the fact that the vasculature supplying cancer lesions may be highly permeable and tumors lack an effective lymphatic drainage system. The EPR effect especially allows nanoparticles in the size range 10–100 nm to preferentially accumulate in tumors and is an emerging strategy for nanoparticle-mediated targeting or delivery [154]. Other approaches for specific cell-targeting include pH-sensitive and

thermosensitive liposomes which can selectively release the cytotoxic agents in the targeted area due to local changes [155] in pH or due to forced local heating [156] (hyperthermia).

A. Biocompatibility and Toxicity of Nanoparticles

At the very outset it should be pointed out that magnetic nanoparticles are classified as medical devices for regulatory purposes and as per the US-FDA should conform to ISO 10993 guidelines. In general, toxicology effects broadly classified as chemical, biological or physical, are all dose dependent. For magnetic nanoparticles the chemical toxicity may be inorganic (from the metal or their salts/oxides) or organic (from the functional coatings). The biological toxicity is typically associated with a threshold dose below which the organism is able to fight the toxin such as by excretion, metabolisation or isolation. Alternatively, it may be associated with a minimum observation time window for which the effect of the toxin is not observed. In this context, of particular concern is the release of the toxins inside the cell followed by interactions with the chromosomal DNA and transferring the cell into a cancer cell. Physical toxicity includes heat and vibration; for example, heat can be generated by magnetic nanoparticles in response to an alternating magnetic field (see Section VI-A). Finally, toxicity of a substance depends on various factors including its physical form, the pathway of administration, the time of exposure, the number of exposures and the organ(s) involved. For further details either see a comprehensive review [157] of the toxicity of magnetic nanoparticles or an appropriate textbook [158].

Magnetic particles used *in vivo* in biomedicine interface with living tissues and biological fluids and by definition can be classified as biomaterials. Broadly, biomaterials are divided as biotolerant, bioinert, bioactive or biocompatible. The body reacts to biotolerant materials by encapsulating them; typical examples are PMMA, silicon and glass and include the silica-coated nanoparticles (see Section III-C) discussed earlier. Bioinert materials have minimal interactions with surrounding tissue—stainless steel, titanium and aluminum oxide are good examples. Bioactive materials, when placed *in vivo*, interact with the bone or soft tissue; however, none of the magnetic nanoparticles are presently known to be bioactive. A biocompatible material produces a specific and well-defined host response, which is necessarily non-toxic.

The toxicity of magnetic particles depends on materials and morphological parameters including composition, degradation, oxidation, size, shape, surface area and structure. When compared to micron-sized particles, it is generally accepted that nano-sized particle can be more toxic because they have larger surface area (hence, more reactive), for a given mass, to interact with cell membranes and deliver any toxic substance [159]. They are also retained for longer periods in the body (more circulation or larger clearance time) and, in principle, can be delivered deeper into the tissue due to their size [160]. The surface coating and their morphology play an important role in determining nanoparticle toxicity. Oleic acid, commonly used as a surface coating in synthesizing nanoparticles with narrow size distributions (see Section III), is hydrophobic and cytotoxic [161]. However, if the oleic acid is used alone without the nanoparticle core it is found to be nontoxic; this underscores the role of the conformal arrangement of the oleic acid on the surface of the nanoparticles in determining their toxicity. Alternatively, if the oleic acid is PEGylated the cytotoxicity disappears [162]. Similarly, the oleic acid covered nanoparticles can be coated with a triblock polymer containing PEO chains (see Fig. 9) and made hydrophilic. Such nanoparticles coated with triblock copolymers are biocompatible and suitable for *in vivo* applications provided the PEO chain lengths are larger than 2 kDa [163]. Other important factors that determine the toxicity of nanoparticles are the surface charge [164] and the propensity of transition metals to produce free radicals that lead to oxidative processes [165] and cellular damage. However, in the case of iron, the healthy human body contains on average 3–5 g in bound hemoglobin form and all

the proposed therapeutic interventions (see Section VI) require far lower concentrations. Moreover, the toxicities that are of concern arise from local effects due to prolonged oxidative stress and inflammation.

Determination of nanoparticle toxicity requires testing in both *in vitro* and *in vivo* conditions. *In vitro* cell culture assays are more sensitive to toxicity than body tissue. They are used first before animal testing to understand mechanisms of cellular toxicity, determine which cell functions are adversely affected and the possible causes of toxicity. Subsequent *in vivo* testing, consistent with regulatory guidelines [166], can determine the response of the overall biological organism. Cytotoxicity measurements [167], originally designed for rapid and inexpensive analysis of soluble pharmaceuticals, are a critical part of nanoparticle development and are generally quantified with colorimetric assays [168]–[172]. Even if the coating polymer and the nanoparticle materials may themselves be individually non-toxic, the method of coating may greatly affect the cytotoxicity of the resulting coated-nanoparticle. In general, performing *in vitro* cytotoxicity characterization with nanoparticles is not straightforward. Depending on the nanoparticles and the assay used, possible interactions include: a) increasing apparent cell dosaging due to agglomeration and settling of nanoparticles in cell culture [173]; b) erroneous increase or a decrease in cell viability due to nanoparticle interference with the development of colorimetric assays [174] and c) interference due to fluorescence or absorbance of nanoparticles at the same wavelength of the assay dye. Careful experimental design is required to address these issues.

The commonly used cell culture assays can be divided into two main categories: assays measuring metabolic activity expressed as mitochondrial function and those involving membrane integrity. To assay for mitochondrial damage different tetrazolium salts, such as (3-(4,5-Dimethylthi-azol-2-yl)-2,5-diphenyltetrazolium bromide (MTT) and 3-(4,5-dimethylthiazol-2-yl)-5-(3-carboxymethoxyphenyl)-2-(4-sulfophenyl)-2H-tetrazolium, inner salt (MTS), that penetrate both the cell and mitochondrial membranes, are used. Initially these salts are yellow in color but mitochondrial activity metabolizes these salts to form blue, insoluble formazan crystals that are clearly visible in healthy cells. The quantity of formazan is directly proportional to the number of visible cells and after a specific period of time (say, 3 h) the formazan can be solubilized and quantified. Alternatively, if the cell membranes are damaged the contents of the cell can leak out and can be measured. For example, the enzyme lactose dehydrogenase (LDH) is present in the cytosol of the cell and can be measured extracellularly only if the cell is damaged. The LDH assay is not ideal for the detection of threshold dose for the onset of toxicity but can reliably be used to infer the dose at which the cells can no longer survive. In general, such *in vitro* testing is a complex task but should be integral to any development of magnetic particles for biomedical applications. To detect interference of nanoparticles with results, complementary cytotoxicity assays are used. Concurrent assays are performed on the same samples, by separating cells and supernatant, with viability assayed directly on cells and cytotoxicity assayed with the lactate released into the medium.

A detailed overview of assessing cytotoxicity of iron oxide nanoparticles can be found in the literature [167]. Here, we present a brief description of such assays applied to testing of Pluronic F127 coated magnetite nanoparticles synthesized in our laboratory. We used MTT and MTS assays in the presence of phenazine methosulfate (PMS) that measure mitochondrial activity, as well as resazurin to assay cell viability. The MTT assay requires the formation of a water-insoluble formazan crystal, which can interact with various reagents [175]. A lactate dehydrogenase (LDH) assay was used to determine cytotoxicity via cell membrane integrity [176]. A typical result [177] derived from such methods, with mean standard deviations, confirming that the particles are non-toxic, is shown in Fig. 11. Concurrent assays are performed on the same samples, by separating cells and supernatant, with viability assayed

directly on cells and cytotoxicity assayed with the lactate released into the medium. Moreover, relevant controls need to be identified and tested simultaneously. In addition to basic positive (agents that kills 100% of cells) and negative (no nanoparticles or toxic agents) controls, cell viability can also be affected irrespective of whether nanoparticles are taken up or not. Toxic agents can be released from nanoparticle surfaces that are normally unaccounted for. As a result, culture media exposed to nanoparticles should be centrifugally or magnetically separated from the nanoparticles (but including any remnants released from nanoparticles) and then again used to incubate a separate set of control cells. More on such uptake-dependent and -independent effects can be found elsewhere [167].

We conclude with a brief discussion of the cellular toxicity of manganese in light of their proposed use as magnetic resonance detectable contrast agents in the human body (Section VI-D). The adult human body contains 10–20 mg of manganese, most of which is concentrated in the liver, kidneys, pancreas and bone. Manganese is an important catalyst and cofactor in many enzymatic processes active in the mitochondria as well as those involved in the synthesis of fatty acids, cholestrol, mucopolysaccharides (important constituent of skeletal and cartilage structural matter), and glycoproteins that coat body cells and protect them against invading viruses. However, ingestion of large amounts of manganese is poisoning and chronic overexposure can produce a progressive, permanent neurodegenerative disorder, with few options for treatment and no cure [178]. Historically, toxic effects in animals discouraged the early development of manganese-enhanced magnetic resonance imaging (MEMRI) [179]. The MSDS for $MnCl_2$ suggests that doses as low as 93 mg/kg for rats or 38 mg/kg for mice show significant adverse effects and mortality rates. However, current MEMRI experiments are being performed at similar doses, or higher, with good results and few adverse effects reported. For example, Aoki *et al.* have been able to reliably administer up to 175 mg/kg intravenously in rats up to 250 g body weight [180], and in mice up to 25 g body weight with only minor and temporary side effects that resolved slowly over 30–60 min after administration. Particular experimental details and procedures, such as the concentration of the $MnCl_2$ solution, the rate of infusion and the route of administration, temperature of the solution and anesthetic levels seem to play an important role in determining the maximum effective dose that can be safely administered without major side effects [181]. Overall, the use of Mn^{2+} should be undertaken with minimal dose and the utmost caution; the brain is the major target organ for Mn^{2+} toxicity and it retains Mn^{2+} much longer than other tissues.

VI. Magnetic Nanoparticle Applications in Biomedicine

The range of applications of magnetic nanoparticles in biomedicine can be broadly divided into *in vitro* and *in vivo* categories (Fig. 12). Recently, there has been tremendous activity in the area of *in vitro* diagnostics involving, for example, SQUID assays [273], magnetoresistive and cantilever sensors [274]–[276], as well as many magnetic manipulation [277] and separation [278] techniques. The same can be said about tissue engineering. These technologies are best dealt with in other independent reviews [279]. Here, in keeping with the emphasis of this paper on work done in our laboratory, these applications in imaging, diagnostics and therapy, illustrating the fundamental principles involved, are discussed along with detailed experimental methods, where appropriate, in the sections that follow.

A. Magnetic Fluid Hyperthermia

Magnetic fluid hyperthermia [182]–[184] (MFH) is a form of localized heating to 42–46°C, using magnetic nanoparticles, that can kill or damage tumor cells. The processes responsible for heat generation in magnetic nanoparticles are either hysteretic or relaxation losses. Multi-domain particles with $D > D_{sd}$ (see Fig. 3) respond to an external field by Bloch wall displacements and the resulting hysteresis loop, that is a measure of the energy dissipated during one magnetization cycle (and hence, the local temperature rise), depends strongly on

the sample prehistory and the magnitude of the applied field. As a result, these particles are not suitable for MFH and instead, smaller single-domain or superparamagnetic particles with tailored relaxation behavior using alternating magnetic fields are preferred (the physics of MFH is described later in this section). Note that most cytotoxicity or biocompatibility (cell killing or survival) studies (see Section V-A) in preclinical tissue cultures are performed under standard biological conditions where cells are supplied with nutrients and oxygen, under normal pH (~7.4) and standard growth temperatures (37.5°C). However, except for growth temperature, these conditions will differ inside many tumors. In fact, inside many tumors nutrients and oxygen are in short supply and the pH is well below that of normal tissue. It is now well established that such nutritional deprivation, low oxygen content (also called hypoxicity) and low pH tend to make cells more heat sensitive [185], [186]. This is one of the principal motivations to suppose that some tumors, at least, should be more heat sensitive, compared to normal tissue, suggesting localized hyperthermia as a mode of treatment.

Like other current treatments of cancer that strive to preferentially destroy malignant cells without impairing normal tissue, there is a limiting dose. For example, surgery removes cancerous cells but must be limited in scope to protect vital tissue parts. Radiation destroys malignant cells by exposing them to lethal doses of X-rays but dosage must be limited to prevent excessive damage to normal tissue within the treated volume. Chemotherapy using anti-cancer drugs kills individual cancer cells but is systemic in nature and the limiting dose is defined by the cell system most sensitive to the specific drug being used. Hyperthermia, in the form of localized heating can also kill cancer cells but, as in the above, it is the response of normal tissues that determines what “dose” of heat can be applied. The dose response curves for hyperthermia look similar to those for radiation or drug dose, but the critical cellular target of thermal inactivation is not yet known [187]. Note that hyperthermia differs significantly from thermoablation, which employs higher temperatures, up to 56°C, to crudely destroy cells leading to necrosis, coagulation and carbonization [188]. It is recognized that hyperthermia alters the functions of many structural and enzymatic proteins within cells that affect cell growth and differentiation, which can induce apoptosis [189], [190]. In hyperthermia, both temperature and time at the elevated temperature determine the cell survival rate. The relationships are non-linear and hence, instead of a single or even a linear combination of physical variables, a complete record of time and temperature is necessary to define the heat dose. However, all mammalian cells are susceptible to elevated temperatures and their survival rate, which decreases with exposure time, is further reduced with increasing temperature above 41°C (See Hahn, 1984) [183].

In addition to delivering heat, hyperthermia offers additional treatment options by enhancing the effects of chemo-radiation treatments, exhibiting particular synergy between the applications of heat and X-ray radiation [191]. Under appropriate conditions [192], cytotoxicity is enhanced by at least two orders of magnitude when cells subject to X-rays are also exposed to sustained temperatures either before or after irradiation. Alternatively, it takes ~30% less radiation dose (referred to as a dose modification of 1.3) to kill the same fraction of cells when they are also subjected to hyperthermia. This is because hypoxic cells are notoriously resistant to X-ray radiation but heat destroys hypoxic cells as efficiently as normal cells. Again, by preferential heating of the tumor volume, the benefits of combining heating with radiation can be enhanced. The synergy between heat and radiation dose, as well as various cytostatic treatments, has been validated by a number of preclinical studies [193], [194]. However, the time between treatments and the sequence of their application are important [195]. For example, when radiation and heat treatment are combined, best results are obtained for simultaneous applications but this may be difficult to realize in clinical practice. Similarly, combinations of hyperthermia and chemotherapy and interactions of heat with a wide range of chemotherapeutic drugs have been found, with many orders of magnitude enhancement in efficacy, even for moderate increases in temperature [196]. There are also reports that heated

cells provoke an enhanced form of immune response [197], [198]. This is a subject of ongoing investigations and such arguments of antigenicity also apply to other forms of therapy such as X-ray radiation. It is suggested that heat shock proteins chaperon tumor antigens and, based on this hypothesis, a number of mechanisms for antitumor immunity induced by hyperthermia has been proposed [199]. More details can be found in the literature [200], [201].

In practice, it is technically challenging to induce and sustain temperatures clearly above the systemic temperature of 37.5°C in a defined target volume. Perfusion counteracts the temperature rise and perfusion rates, though they vary widely in tumors with leaky vasculatures, are ~ 5–15 mL min^{-1} per 100 g of tissue. Therefore, reaching therapeutic temperatures of 42–44°C in the critical parts of tumors requires a specific heating power, SHP ~ 20–40 W kg^{-1} in the local target region [202] (for comparison, the human basal metabolic rate is ~ 1 W kg^{-1}). The cooling action of flowing blood must also be taken into consideration, and furthermore, blood flow rates will vary during hyperthermia treatment. Taken together, these effects invariably result in non-uniform temperature distributions. In some tumors, at T > 43°C, for extended periods, *t*, of heating (*t* > 30 min), the blood flow may altogether stop completely [203].

Several clinical studies conducted recently have questioned the need to achieve a minimum temperature of 43°C in the target volume and, in fact, effectiveness of hyperthermia at lower temperatures has been reported [204]. Nevertheless, even though the exact temperature that has to be reached for the clinical efficacy of hyperthermia is unclear, attempts should be made to achieve temperatures as high—within the range of 42–46°C—and as uniform as possible. Finally, for hyperthermia to be truly effective, monitoring the temperature distribution during heating may be essential but remains an ongoing challenge.

Just as in other modes of therapy such as radiation, localized hyperthermia is delivered in fractional courses and not as a single dose. Moreover, heating is not instantaneous and before a tumor reaches the target temperature (42–46°C), some time must be spent at lower temperatures. *In vitro* studies of cells show complicated, yet consistent, responses to heat treatments in different temperature regimes. If the cells are treated at $T \geq 43°C$ for a short time, the surviving cells are much more sensitive to subsequent heat treatments even at lower temperatures. This is referred to as step-down heating [205]–[207]. However, if the initial heating is at $T < 43°C$, then cells are resistant to heating at any other subsequent temperatures. Finally, even if cells are heated for any time to $T \geq 43°C$ but then incubated at ~ 37°C for ~100 h, they are much more resistant to heating compared to cells that have not been previously heat-treated. The behavior in the last two cases, referred to as thermotolerance, is the subject of ongoing investigations. It is known that the expression of several genes can be upregulated or downregulated by heat, amongst them, for example, is the family of heat shock proteins [208], which play a critical role in thermotolerance [209]. Finally, thermotolerance has been demonstrated to occur in both normal tissue and in tumors *in vivo* [210]. Thus, excessive heating at the beginning of a treatment cycle, even for a short period of time, can lead to step-down heating. This may be beneficial but could also lead to unexpected toxicity in healthy tissues. On the other hand, initial slow heating, for example, while the patient is being set up, can lead to significant thermotolerance. For hyperthermia to be effective, it is important that the initial heating be rapid. Moreover, during treatment care should be taken to ensure that the spatial distribution of temperature in tumors and normal tissues is as controlled and uniform as possible.

To achieve local heat generation in tissues using magnetic fluid hyperthermia (MFH) we exploit the heat generated when an electromagnetic field interacts with matter. The details of this mechanism depend on the characteristics of the field, i.e., amplitude and frequency, and the materials properties of the nanoparticles comprising the magnetic fluid being used. When

an alternating field of sufficiently high frequency is applied, the magnetization of a superparamagnetic particle lags behind the applied field (Fig. 13(a)). As a result of this phase lag, the susceptibility, $\chi = \chi' - i\chi''$, is an imaginary quantity with the real part, χ', representing the in-phase component, and the imaginary part, χ'', the quadrature or loss-component are given by

$$\chi'(\omega)=\frac{\chi_0}{1+(\omega\tau)^2} \tag{6.1}$$

and

$$\chi''(\omega)=\frac{\chi_0\omega\tau}{1+(\omega\tau)^2} \tag{6.2}$$

where χ_0 is the dc magnetic susceptibility.

Note that χ' decreases with increasing frequency but the imaginary part, χ'', peaks at an angular frequency $\omega = 2\pi f = 1/\tau$, where τ is the relaxation time of the particles. The relaxation time

$$\tau=\frac{\tau_B\tau_N}{\tau_B+\tau_N} \tag{6.3}$$

is a weighted average between the Néel, τ_N and Brownian, τ_B relaxations (Fig. 13(c) and (d), respectively), which are defined as

$$\tau_N=\frac{\sqrt{\pi}}{2}\tau_0\frac{\exp(KV/k_BT)}{(KV/k_BT)^{1/2}} \tag{6.4}$$

and

$$\tau_B=\frac{3\eta V_H}{k_BT} \tag{6.5}$$

where η is the viscosity of the matrix fluid, k_B the Boltzmann constant, T the absolute temperature (K), V_H, the hydrodynamic volume of the particle which includes any non-magnetic layer, V the magnetic volume and τ_0 the attempt time here equal to 10^{-9} s. The specific loss power for a monodisperse sample of superparamagnetic particles can be written as

$$P=\pi\mu_oH_0^2\chi''f=\chi_0H_0^2\mu_o\pi\frac{2\pi f^2\tau}{1+(2\pi f\tau)^2} \tag{6.6}$$

where χ_0 is the initial DC susceptibility, H_0 is the field amplitude, f is the frequency of the measurement and τ is the relaxation time. However, for real ferrofluids polydispersity must be taken into account. Polydispersity of particle size can be modeled with a lognormal distribution

$$g(R)=\frac{1}{\sqrt{2\pi}\sigma R}\exp\left(\frac{-(\ln(R/R_0))^2}{2\sigma^2}\right) \tag{6.7}$$

where ln R_0 is the median and σ the standard deviation of ln R. The volumetric heat release rate of a polydispersion is now

$$\overline{P}=\int_0^\infty Pg(R)dR. \tag{6.8}$$

Based on this physical model, we now briefly discuss recent measurements of the specific loss power (SLP) of magnetite nanoparticles with narrow size distributions. A clear dependence of the SLP on particle size and the need to match the mean nanoparticle size to the applied frequency to achieve the maximum heating rates are demonstrated.

Experimental Details—Spherical iron oxide nanoparticles were synthesized in our labs with a protocol described in Section III-B. As-synthesized particles are not soluble in aqueous solutions therefore they were coated with Pluronic F127 in order to transfer them from a non-polar organic solvent to the aqueous buffer, phosphate buffered saline (Fig. 7). Ferrofluids were concentrated by evaporating the solvent under a gentle argon stream. A Phillips 420 Transition Electron Microscope (TEM), operating at an accelerating voltage of 120 keV, was used to routinely characterize nanoparticles size and shape. Their size and distribution were also routinely determined by dynamic light scattering. 10 nm iron oxide particles were shown to be magnetite (Fe_3O_4) by comparing the ratios of L_3 to L_2 transitions in electron energy-loss spectroscopy. Particle size and size distribution were determined magnetically by fits to room temperature magnetization curves, collected with a VSM, using the Chantrell method [211]. To accommodate the possible variation in the phase of the iron oxide as a function of size, we conservatively assumed 75 emu/g at saturation in all calculations to determine the mass of the magnetic portion of the sample. Alternatively, iron concentrations of phase-transferred nanoparticles were confirmed with Jarell Ash 955 Inductively Coupled Plasma—Atomic Emission Spectrophotometer (ICP). Mass of the iron oxide nanoparticles was determined assuming all the iron was in Fe_3O_4 phase and was in good agreement with the values determined magnetically. Four different nanoparticle samples (Fig. 14(a)) were measured and the data is shown in the table. Note that there is a difference between the particle size determined from TEM and from the Chantrell fitting based on magnetization measurements. This difference may be due to the error in the assumption of 75 emu/g for these samples. Alternatively, this may indicate that there is a magnetic dead layer on the particles. Because of this possibility, we have used the diameter, polydispersity (σ) and concentration (φ) determined magnetically throughout our calculations.

Calorimetric measurements were made on a modified induction heater with a 3 turn, water-cooled, copper pipe. Calorimetric measurements were performed at 400 kHz with various ac-field amplitudes (12.4, 16.3, 21.9, 24.5 kA/m). Approximately 0.5 mL of ferrofluid was used per measurement and placed in an insulated Falcon tube. Temperature was monitored with a Cu-Cu/Ni thermocouple with an ice bath reference (However, in recent experiments the thermocouple has been replaced with a highly sensistive optical pyrometer to avoid any eddy

current effects). Experiments were run for 300 s with 1 s intervals. The first ~60 s were run before the field was turned on in order to collect the background temperature. The temperature of the ferrofluid sample was measured as a function of time and the specific loss power (SLP) was calculated as

$$\mathrm{SLP\,(W/g)} = c\frac{m_{\mathrm{sample}}}{m_{\mathrm{ironoxide}}}\left(\frac{dT}{dt}\right) \tag{6.9}$$

where c is the heat capacity of water, m_{sample} is the mass of the sample and $m_{\mathrm{ironoxide}}$ is the mass of the iron oxide in the sample measured magnetically and dT/dt is the slope of the heating curve.

The SLP measured for the samples at varying ac field amplitudes are shown in Fig. 14(b). The data fit well to the square law as expected, indicating the good quality of the measurements. Plots of the SLP for the various σ values measured for the samples are shown in Fig. 14(c). The calculations were done for a salt-water solvent having a specific heat of 4.19 J g^{-1} K^{-1}, mass density 1.027 g m^{-3} and viscosity 0.0010 kg m^{-1} s^{-1}. Non-magnetic layer thickness was set to 12 nm corresponding to the thickness of the surfactant and Pluronic coating. Magnetic field conditions were set at f = 400 kHz and H_0 = 24.5 kA/m. The figure shows that as polydispersity increases, SLP decreases very rapidly. Additionally, there is a narrow size range which yields extremely high heating rates with a peak, for these specific experimental conditions, for particles with diameters ~12.5 nm. The SLP for Samples 1–4, including the size distribution based on magnetization measurements, are also plotted against the theoretical values (scaled to match the data). All the samples are in good agreement with the theoretical values except for Sample 1 which has a heating rate much higher than expected. The data shows that that heating rate indeed depends on particle size, although not enough sample sizes were measured to observe a peak in SLP for these measurement conditions. This is the first time a size dependant effect has been demonstrated. It is possible that higher heating rates are achievable by increasing the magnetic core of the particle to approximately 12.5 and further decreasing the polydispersity of the sample.

Finally, for *in vivo* applications of MFH, in addition to the physics of heating, the vast number of known magnetic materials is strongly limited by biocompatibility considerations such as non-toxicity, sufficient chemical stability, especially of the coatings and stable magnetic properties in the bioenvironment, appropriate circulation times and finally, harmless biodegradability. As a result, the majority of the investigations of MFH are concentrated on the magnetic iron oxides, magnetite (Fe_3O_4) and maghemite ($\gamma - Fe_2O_3$), which are known to be well tolerated by the human body. In the case of such oxides, inductive heating is not an issue as the material is poorly conducting and, in nanoparticle form, is also physically too small to sustain a closed eddy current loop. However, the electrical conductivity of biological tissue is sufficiently high that an alternating magnetic field may generate eddy currents and cause a non-selective heating of both cancerous and normal tissue. The heat generated by such induced eddy currents is proportional to the square of the product (HfD), where H is the field amplitude, f is the applied frequency and D is the diameter of the induced current loop in the body. Thus, for any fixed diameter of the induced current loop, an upper limit of the heat tolerated by the body is defined in terms of the product, H.f, of the field amplitude and the frequency. Experimentally, this limit has been estimated [214] to be $H.f \sim 4.9 \times 10^8$ $Am^{-1}s^{-1}$. This product has to be considered[3] in determining the conditions for optimizing the specific heating power

[3]Some people doubt that this value is really the absolute maximum. In the literature, there is evidence for use of higher values (2–5 × more) without deleterious effects.

(see next section) for a given nanoparticle-applicator combination in a MFH system. Note that sustained application of ferromagnetic resonance, with required frequencies in the GHz range, is out of consideration because of the deleterious side effects of such high frequencies on healthy tissue.

B. Drug Delivery With Triggered Release

Ideally, a magnetically responsive drug carrier, such as a nanoparticle, should have the following important characteristics [215], [216]. It should be small enough (size < 1.4 μm) to permit capillary-level distribution and a uniform perfusion of the target. It should have an adequate response to magnetic fields and field-gradients that are technically feasible, especially for the flow rates found in physiological systems. In humans, these are 0.05 cm/s (in capillaries) and 2 cm/s (in arteries). Magnetic drug carriers should not only be able to carry a wide variety of chemical agents but also have adequate space to accommodate significant quantities such that they are able to deliver the required drugs without excessive magnetic carrier loading. Drug release rates at the target site should be controllable and predictable. In fact, it would be beneficial to have a release mechanism that can be triggered by an external stimulus. Carrier surface characteristics should maximize their biocompatibility and minimize antigenicity. After delivery, the carriers should be easily biodegradable or cleared from the body. Finally, the method of injection should ensure that carriers enter the target/tumor vasculature before being cleared by the RES.

Poly (*N*-isopropylacrylamide) or p-NIPAAM is one of the most studied temperature-sensitive polymers [217], [218] and, in aqueous solution, it is well-known to exhibit a sharp phase transition, called the lower critical solution temperature (LCST), at a temperature in the range of 298–310 K depending on the composition. Below the LCST, the p-NIPAAM random coil chains are hydrated, hydrophilic in nature, and swollen (Fig. 15(b)). Above the LCST, the chains become hydrophobic, dehydrated but weakly hydrogen-bonded with water molecules and collapsed (Fig. 15(a)). At T < LCST, in the swollen or open configuration, they can be loaded with drug molecules and as the temperature is raised, i.e., T > LCST, when they collapse, they can release or squeeze the drug molecules out. By coating iron oxide nanoparticles with p-NIPAAM, their local temperature can be raised by externally applied ac fields, a mild form of heating, to trigger the local release of the drugs.

Experimental Details—As synthesized, iron oxide nanoparticles are coated with surfactants, typically oleic acid (Section III-B). Well-defined p-NIPAAM, separately synthesized by the reversible addition fragmentation chain transfer process (RAFT) [219], was used to coat these particles by a surfactant exchange method. Exchange was conducted in dimethylformamide (DMF). Iron oxide nanoparticles (10 mg) were dispersed in DMF (1 ml, 1:1) and the mixture was heated at 70°C for 1 h, and later sonicated for 5 min. p-NIPAAM was dissolved in 3 ml of DMF and added to the iron oxide solution. The mixture was heated at 70° C for 3 days and centrifuged. The precipitate was washed two times with DMF and then re-dispersed in distilled de-ionized water (4 ml). The black solid was dissolved in water and dialyzed against water using a dialysis membrane of MW cutoff of 20 k for 48 h. These p-NIPAAM-coated nanoparticles [220] were characterized by ac susceptibility and dynamic light scattering (DLS).

The changes in the hydrodynamic volume of the p-NIPAAM-coated iron oxide nanoparticles as a function of temperature, associated with their swelling and collapse with increasing temperature from below to above the LCST, can be detected by using frequency dependent magnetic measurements. The temperature dependent physical behavior is monitored by measuring the imaginary component of the magnetic susceptibility, χ'', above and below the LCST of p-NIPAAM. A clearly defined peak in χ'' as a function of frequency correlates with

swelling and collapse of p-NIPAAM. Note that in order to monitor the changes in hydrodynamic volume by Brownian rotation the nanoparticles must be ferrimagnetic at room temperature. Hence, magnetite nanoparticles synthesized by the decomposition of metal fatty acid salts in non-aqueous solvents [221], such as octadecene, producing bigger ferromagnetic particles are better suited for this work. Room temperature ferrimagnetism of the nanoparticles was confirmed by hysteresis measurements using vibration sample magnetometry (VSM). Typical open loops with a coercivity of ~35 Oe were observed for these nanoparticles (average diameter ~33 nm, std. dev. 2.9 nm) as confirmed by transmission electron microscopy (TEM). For magnetite, based on bulk values of magnetocrystalline anisotropy (~ 1.3×10^5 ergs/cm^3) and a typical measurement time of 100 s, the characteristic diameter for superparamagnetic behavior can be estimated to be ~27 nm (see, Fig. 3).

For applications of nanoparticles involving their Brownian relaxation it is important to choose a measurement temperature below the nanoparticles' ferrimagnetic blocking temperature and above the carrier fluid's freezing temperature. Hence, control of nanoparticle size and selection of carrier fluid is important. Since the nanoparticles described above have a blocking temperature above room temperature, relaxation measurements can be performed in water, which is a prime requirement for bioapplications. For smaller nanoparticles, which have lower blocking temperatures (typically, $T_B < RT$) water/solvent freezing can prevent the nanoparticles from rotating freely and impede Brownian relaxation measurements. The Brownian relaxation time of the aqueous ferrofluid is altered when biomolecules or polymer coatings bind to its surface because of the change in the hydrodynamic radius of the biomolecule/polymer-magnetic nanoparticle compared with the magnetic particle alone. Hence binding of biomolecules/polymers to colloidal magnetic particles can be detected by measurement of the relaxation time of magnetic particles. A schematic representation of the measurements on p-NIPAAM coated magnetic particles, above and below LCST is shown in Fig. 15(d). Below LCST, the polymer is swollen and its hydrodynamic volume will be larger. Above LCST the polymer chains collapse and the hydrodynamic radius is smaller. These conformal changes should be evident from the relaxation measurement. Fig. 15(e) shows the frequency dependence of the imaginary part of the ac susceptibility at different temperatures. The most striking feature seen in these plots is the evolution and coexistence of two peaks arising from two relaxation processes in the system, one at about f_{rH} ~ 3900–5000 Hz (high frequency) and the other at f_{rL} ~ 850–2000 Hz (low frequency). The high frequency peak is attributed to the Brownian relaxation of individual nanoparticles and its shift to higher frequencies (~50–100 Hz) with increasing temperature reflects a decrease in their hydrodynamic volume due to the collapse of p-NIPAAM above LCST. However, this shift is very small because even though the hydrodynamic volume of the particle decreases, the change in viscosity of water over this temperature range is much larger (more than a factor of two) and dominates the response. The low frequency peak is attributed to the aggregation of the nanoparticles in the ferrofluid. At 280 K, the two peaks are not distinguishable. At intermediate temperatures both the peaks coexist showing the relaxation of both individual and agglomerated particles. At 315 K, the high frequency peak becomes dominant. The effective hydrodynamic volume can be calculated using the frequency value of the maximum in the imaginary part of the susceptibility. As the temperature increases, the low frequency peak shifts to smaller values consistent with DLS results (not shown) [222] where it was found that the particle size is smaller below LCST, while with the increase in temperature, particle size also increases. However, an increase in temperature above LCST should collapse the p-NIPAAM molecules on the iron oxide nanoparticles. This collapse will also cause the nanoparticles to aggregate in solution with increase in temperature since the surface of the nanoparticles is now hydrophobic. In summary, such p-NIPAAM-coated magnetite particles hold promise for triggered release of drugs, where the triggering mechanism is heating via an externally applied ac field.

C. In Vitro Diagnostics Using AC Relaxation Dynamics

In addition to serving as a universal separation tool [223]–[225], magnetic nanoparticles can be used as labels for biosensing with many distinct advantages. The magnetic properties of the nanoparticles are stable over time and their magnetism is seldom affected by reagent chemistry or subject to photobleaching (which is a problem with optical fluorescent labeling). More importantly, there is also no significant magnetic background present in biological samples (they are weakly diamagnetic) and magnetic fields are not screened by aqueous reagents or biomaterials, thus eliminating any interference or background signals [226].

The response of magnetic nanoparticles, suspended in a liquid, to a small alternating field with a frequency, ω, given by its complex susceptibility, χ, depends on its relaxation either through the Brownian or Néel mechanism. Recall that the effective relaxation time ((6.3)) for larger particles is dominated by τ_B and is dependent on the hydrodynamic volume, V_H, of the particle and the viscosity, η, of the medium. The Néel relaxation time, τ_N, has been discussed earlier (Section VI-A). The Brownian, Néel and effective relaxation times for magnetite particles with $K = 20$ kJ/m^3, a chemical coating ~15 nm in thickness and suspended in water ($\eta = 10^{-3}$ Ns/m^2) are plotted as a function of size in Fig. 16. Note that a magnetic core, 20 nm in diameter, will correspond to a hydrodynamic radius of 25 nm. It is clear that the Néel relaxation time, τ_N, depends more strongly on the particle size than the Brownian relaxation time, τ_B. As mentioned, above a critical size, $\tau_B > \tau_N$, the Brownian relaxation dominates. For such blocked particles, the peak in the imaginary part of the magnetic susceptibility is determined by τ_B and is inversely proportional to the effective hydrodynamic volume of the particles:

$$\omega = \frac{1}{\tau_B} = \frac{k_B T}{3 V_H \eta} = \frac{k_B T}{4\pi R_H^3 \eta} \tag{6.10}$$

where R_H is the hydrodynamic radius of the magnetic nanoparticle. Therefore, if the hydrodynamic radius of the particle were to increase (Fig. 13(d)) as a result of the specific binding of a target molecule to the nanoparticle, τ_B will increase and the frequency at which the peak in the imaginary component of the susceptibility is observed will decrease. This sensing scheme for a specific affinity binding will work provided the nanoparticles are below the critical size for single domain behavior. Above this particle size, the relaxation no longer reflects the Brownian motion but is dominated by internal changes in magnetization due to domain wall motion. It is straight forward to see how this change in hydrodynamic radii, say due to specific binding, can be detected in solution by monitoring χ'' as a function of frequency. Details of this method to detect specific affinity binding of biotin-streptavidin [227] and related effects can be found in the literature. These and related experiments [228] confirm the theoretical prediction [229] of a potential biosensing scheme by demonstrating that the shift in the peak frequency of χ'' can serve as a sensitive measure of specific binding of targeted molecules in solution to functionalized magnetic particles.

D. Contrast Agents for MRI and Molecular Imaging

The intensity of MRI signal from a volume of tissue is a function of the extrinsic, user-selected imaging parameters and the inherent properties of the tissues. The latter includes the density of protons, ρ(H), the longitudinal relaxation time, T_1, in the direction of the stationary field, B_0, the transverse relaxation time, T_2, in the plane normal to B_0, the magnetic susceptibility and any motion of the tissue. In practice, for most soft tissues there is very little variation in the proton density, ρ(H), and hence, T_1 and T_2 have the most influence on image contrast. Therefore, T_1- and T_2-weighted images are interpreted in terms of tissue characteristics and used for diagnostic purposes. However, in many tissues, the intrinsic variations in T_1 and T_2

are also very small and hence, to image them external agents are routinely used to enhance contrast. Such contrast agents are administered orally, by inhaling or by intravenous injection. The choice of contrast agents for MRI depends on the mode of delivery that, in turn, depends on the tissue of interest. As a rule, positive contrast agents—those that influence T_1 relaxation to give brighter contrast—are easier to detect in the MRI images than negative contrast agents —those that influence T_2 to create darker contrast—and are preferred by doctors and radiologists.

In general, there are some important criteria that need to be met in the design of any MRI contrast agent [231]: (a) it must be able to favorably alter the parameters that determine contrast and must also do so efficiently, at low enough concentrations, to minimize dose and avoid any potential toxicity; (b) for the chosen mode of delivery, the contrast agent should have appropriate characteristics to be preferentially delivered to a specific tissue or organ, relative to the rest of the body. In other words, it must be possible to functionalize them for direct targeting or their size must be controllable, without adversely affecting their magnetic properties, for indirect targeting using local variations in the permeability of the vasculature. (c) In addition, potential agents must remain localized at the target site long enough for imaging to be performed, after which they must be cleared and excreted from the body in a reasonable time (several hours) to minimize any effects of potential chronic toxicity. (d) Finally, from a practical point of view, the contrast agents must have sufficient shelf life with stable magnetic properties *in vitro* for at least a few months.

The most effective contrast agents are those that have the greatest magnetic interaction with the hydrogen nuclei and affect their relaxation times [232]. Diamagnetic materials have very weak, negative, magnetic susceptibilities and include water, blood and most organic compounds. Their effects on MR imaging signals are negligible. Paramagnetic materials on the other hand have a net positive, magnetic susceptibility; the magnetic moment of the paramagnetic ion is proportional to the number of unpaired spins. Theoretically, its relaxivity contribution (see (6.8)), or the measure of how it influences the magnetic relaxation of neighboring protons, is proportional to $S(S + 1)$, where S denotes its spin quantum number. In addition, for paramagnetic ions to be used as successful relaxation/contrast agents, they must collectively retain their electron spins along the applied field direction for a sufficiently long time. Therefore, these ions with large spin quantum numbers and the longest spin relaxation times, such as Gd^{3+} ($S = 7/2$), Fe^{3+} ($S = 5/2$) and Mn^{2+} ($S = 5/2$) have been intensely studied as paramagnetic agents for contrast enhancement in MRI [233].

The interactions between a paramagnetic contrast agent and its neighboring protons (water molecules) are two-fold. The scalar or inner-space relaxation refers to the effects of the formation of a strong exchange interaction between water molecules and the paramagnetic ion. It is proportional to the number of water molecules that can bind to each paramagnetic ion in a given time. Therefore, the shorter the residence or interaction time of a single water molecule, the greater the exchange interaction with the paramagnetic ions, and the larger the relaxation enhancement. In practice, most of the metal ions are potentially toxic and to reduce their toxicity they are often administered in a chelated form. A chelate with a high affinity coefficient for the metal ions ensures the stability of the paramagnetic ion *in vivo* and reduces their acute toxicity. However, chelation also reduces the number of sites available for the water molecule to bind. In fact, chelated transition metal ions (Fe^{3+}, Mn^{2+}, etc.) lose all their inner coordination sites, and hence, most of the relaxation effects. On the other hand, the Lanthanides (e.g., Gd^{3+}) have a sufficiently large number of binding sites to bind with water molecules even after chelation. For example, chelated Gd-DTPA (diethylene tetramine pentacetic acid) is a highly stable, effective relaxation agent [234] that has been evaluated [235] and approved for human use. The second or outer-space relaxation is determined by the magnetostatic or dipole-dipole interactions between the paramagnetic ions and protons. It is determined by three parameters:

(a) the strength of the two magnetic moments, (b) the separation between the two dipoles and (c) the relative motion of the two dipoles. Since the magnetic moment of the proton is much smaller (by a factor of ~660) than that of the unpaired electron spin, the effect is dominated by the electron-proton interactions, i.e., proton-proton interactions can be neglected. Further, for a separation, d, between the electron and the proton, the dipolar field of the electron scales as d^{-3}; this orients the nearby protons, following which, the dipolar electron-proton interaction takes place, which also scales as d^{-3}. This effectively gives a d^{-6} dependence in the interaction energy and hence, the more closely the water molecule can approach a paramagnetic ion, the more efficient will be the relaxation enhancement. Clearly, access to the core of the contrast agent where the paramagnetic ion is situated and the use of carrier ligands that minimize the distance of closest approach are desirable [236]. Finally, the relaxation effect is proportional to the number of water molecules that can have dipolar interactions with the same paramagnetic ion. This will be determined by the rate at which the paramagnetic ion can rotate and translate in space.

In addition to the ionic contrast agents, fine, superparamagnetic particles, with significantly larger magnetic moments compared to chelated paramagnetic ions, are also used as contrast agents. When superparamagnetic particles are introduced into the body, then subjected to a magnetic field and temporarily magnetized, the magnetic field distribution in surrounding tissue is altered over distances and times that are long on an atomic scale. Because of their relatively larger magnetic moments (~ a few thousand μ_Bs), uperparamagnetic particles create large heterogeneous magnetic field (gradients) through which water molecules diffuse. Such diffusion causes a dephasing of the proton magnetic moments affecting their magnetization in MRI. Typically, such dephasing shortens their transverse relaxation times, T_2. Ferrimagnetic iron oxide crystals, in magnetite form, with core sizes below the superparamagnetic limit at room temperature are commonly used as MRI contrast agents [237]. Their size also ensures no remanent magnetization and avoids clustering in the absence of an applied field. They come in a range of sizes with different functional coatings and are referred to as superparamagnetic iron oxides, SPIO [238], ultrasmall SPIO or USPIO [239], monocrystalline iron oxide nanocompounds, MION [240], etc. Even though SPIOs are good T_2 contrast agents, their relatively large size and size distribution (volume weighted average diameter ~12 nm) [241] should be considered carefully for targeting and delivery to tissue. However, the low toxicity of Fe, which is normally handled in the various metabolic pathways, makes these agents very attractive. A standard clinical administration of 50–100 mg Fe or 0.01–0.02 mM Fe/kg is low compared to the Fe stored (3500 mg) in the body.

The addition of a contrast agent (solute) causes an increase in the longitudinal and transverse relaxation rates, $1/T_1$ and $1/T_2$, respectively of the nuclei of interest (protons) in the diamagnetic solvent (water). Their contributions are additive and given by the simple equation [242]:

$$(1/T_i)_{obs}=(1/T_i)_{dia}+(1/T_i)_c \; i=1,2 \tag{6.11}$$

where $(1/T_i)_{obs}$ is the observed relaxation rate in the presence of the contrast agent, $(1/T_i)_{dia}$ is the diamagnetic relaxation rate of the solvent alone in the absence of the contrast agents and $(1/T_i)_c$ is the additional contribution from the contrast agents (solute). For sufficiently dilute concentrations of the solute, solute-solute interactions can be neglected and the relaxation rates of the solvent are linearly dependent (Fig. 17(a)) on the concentration, [M], of the contrast agents:

$$(1/T_i)_{obs}=(1/T_i)_{dia}+R_i[M] \; i=1,2 \tag{6.12}$$

where the relaxivity, R_i is defined as the slope of the above linear dependence. The relaxivity, measured in units of $Mol^{-1}s^{-1}$ or $mMol^{-1}s^{-1}$, defines the ability of a fixed concentration of the contrast agent to increase the relaxation rate, which corresponds to a decrease in relaxation time.

Typical relaxivity data for a number of T_2 contrast agents are shown in Table I.

In addition to R_1 and R_2, R_2^* is also shown in the table. For MRI, two major types of pulse sequences are used. Spin echo sequences use two RF pulses to create the echo, which measures the signal intensity and is used to measure T_1 and T_2. On the other hand, gradient echo sequences use a single RF pulse followed by a gradient pulse to create the echo. In the latter case, the signal is affected by the inhomogeneity of the magnetic field and the timing parameters and hence, the combined effect of T_2 and the field inhomogeneity is measured as T_2^*.

Experimental Details—In this context, nanostructured inorganic nanoparticles and core-shell structures can be used as MRI contrast agents with the advantages of flexible surface modification characteristics [244] for targeting and particle dissolution. Specifically, manganese based nanoparticles have potential as T_1 contrast agents that can be "activated" when taken into cells. For example, Mn oxides or Mn carbonates are insoluble at pH ~ 7 but dissolve to release Mn^{2+} at the lower pH found in the endosome-lysosome pathway. The dissolution of Mn based particles in an acidic environment leads to large enhancement of the T_1 relaxation rate [245]. In addition, Mn^{2+} can leave the endosome-lysosome pathway to fill the entire cell leading to a much larger volume distribution of the contrast agent. Control of the rate of dissolution of Mn based nanoparticles can then control T_1 contrast signals, *in vivo* with time. Based on a study of five different coatings on MnO nanocrystals to test the release rate of the Mn^{2+} ions and change in relaxivity at pH 7 compared to pH 5, we have found that $MnO@SiO_2$ nanoparticles (Fig. 8) had the best dynamic range for contrast change when the pH was lowered. Both phantom and animal experiments were conducted. In the latter case, particles were injected into the brain of rats in the region of the thalamus [246], in order to test the rate of dissolution and subsequent neuronal tracing of the released Mn^2. Five rats received 100 nL of 16.8 mM $MnCl_2$ solution into the left hemisphere and $MnO@SiO_2$ solution into the right hemisphere. Images were acquired with an 11.7 T/31 cm horizontal bore magnet (Magnex Scientific Ltd., Abingdon, UK), which was interfaced to a Bruker Avance console (Bruker Biospin, Billerica, MA, USA). A Magnetization Prepared Rapid Gradient Echo (MP-RAGE) sequence was used. Sixteen coronal slices with FOV = 2.56 × 2.56 cm, matrix 256 × 256, thickness = 0.5 mm (TR = 4000 ms, Echo TR/TE = 15/5 ms, TI = 1000 ms, number of segments = 4, Averages = 8) were used to cover the area of interest at 100 μm in-plane resolution in 34 min. The $MnO@SiO_2$ nanoparticles showed the smallest relaxivity (0.3 $s^{-1}mM^{-1}$) at neutral pH, which was stable over time; moreover, they had the best dynamic range for contrast change when the pH was lowered. Time dependent relaxivity measurements at pH ~5.0 in acetate buffer solution showed values increasing to 2.44 $s^{-1}mM^{-1}$ by 53 min to 6.1 $s^{-1}mM^{-1}$ after 75 h. This final relaxivity is equivalent to $MnCl_2$ indicating that the particles had completely dissolved. The release rate of Mn^{2+} ions was faster for the first 5 h, subsequently slowing down after 10 h. MP-RAGE images of the rat brain (Fig. 18) showed that the signal intensity at the injection site of $MnO@SiO_2$ particles (right sides in images) increased with time consistent with the slow dissolution rate measured *in vitro*. The signal at the site of $MnCl_2$ injection (left sides of images) was elevated at the first image after injection and began to decrease slightly due to tracing of the Mn^{2+} ions to different parts of the brain. In summary, *in vivo* MRI of $MnO@SiO_2$ particles injected into the brain showed time-dependent signal changes consistent with the *in vitro* rates. The $MnO@SiO_2$ particles show the best potential for delaying the release of MRI contrast until specific biological processes have occurred, such as endocytosis.

The rapid delivery of chelated molecules and nanoparticles in the blood to the interstitium of the tissues is based on diffusion and the sizes of the pores of the capillary (Section II-C); hence, the endothelial cells lining their walls regulate the permeability of the agents. Charge and concentration further complicate this simple picture. The increased permeability of the tumor vasculature allows the delivery of contrast agents by indirect tumor targeting as has been discussed earlier (the EPR effect [49]). Fenestrated capillaries are also found in gastrointestinal mucosa, endocrine and exocrine glands. Finally, particles over 50 nm in diameter are largely cleared by the RES (Kupfer cells in the liver and macrophages in the spleen and lymph nodes) because these capillaries are sinusoidal (Fig. 4(d)) with pores larger than 100 nm. Including their surface modification for stability in the aqueous phase, nanoparticles of magnetite, in the form of colloids are typically in the 10–20 nm size range. In fact, nanoparticles of ~20 nm diameter are relatively large (20 nm corresponds to a globular protein molecule of ~720 kDa in size) that should be taken into consideration with respect to effective delivery. Size control of SPIO particles helps to prolong blood circulation time and control their biodistribution. For example, comparatively larger SPIO particles such as AMI-25 (80 nm) [81] and SHU-555A (60 nm) [247] are rapidly cleared from the blood circulation by the liver with a half-life of 8–10 min. They do not even reach the bone marrow or lymph nodes [248]. The threshold size for the RES of the liver and spleen is about 20 nm and hence, smaller SPIOs such as AMI-227 (20 nm) [249] with a half-life of 200 min and MION-46 (18–24 nm) [240] with a half-life of 180 min, remain in the blood long enough for a small fraction to leak into the interstitium and are then cleared by the mononuclear phagocyte system to subsequently accumulate in the lymph nodes. Thus, 20 nm diameter particles are used as intravenous agents for delivery to systemic lymph nodes [250].

Magnetoliposomes [251] or vesicles with a nanometer-size magnetic core, typically magnetite, wrapped in a phospholipids bilayer can function as MR contrast agents with the added advantage, due to their ability to encapsulate drugs and genes, of combining diagnostics and therapy. They are prepared by many different methods [252] and to improve circulation times PEGy-lated phospholipids complexes are incorporated in the bilayer. The latter have been effective in targeting the bone marrow [253]. In fact, liposomes have been studied as preferential contrast agents for the RES and have demonstrated [254], [255] specific contrast enhancement of the liver. However, liposome encapsulated T_1 agents such as those incorporating Gd-DTPA have weaker T_1 than the same concentration of free Gd-DTPA. The process of T_1 shortening, as discussed earlier, requires the direct interaction between protons and the magnetic components of the contrast agents. The restricted access of the extracapsular water molecules to the contrast agents in the interior of the liposomes makes them less effective. Additional problems arise due to the comparatively long half-life of several days for the hepatic clearance of Gd-DTPA and the associated potential toxicity [256]. Finally, a typical MION-46 agent, with mean particle diameter of 18–24 nm and $R_2 \sim 7200\ mM^{-1}s^{-1}$ is estimated to require a minimum concentration of 1.6×10^{-5} niM for visibility in MRI. This makes it potentially feasible to use them as labels for receptor contrast enhanced imaging.

E. Magnetic Particle Imaging: A Complementary Imaging Paradigm

As we have already seen, contrast agents and tracers used in medical imaging provide critical information for diagnostics and therapy. The two inter-related parameters that define the applicability of any medical imaging technique are spatial resolution and the sensitivity or detection threshold. The latter, in the case of contrast agents used in magnetic resonance imaging in both *in vitro* [257] and *in vivo* [258] applications, appear to be limited by the background signal from the host tissue. Alternatively, measurements of the magnetic relaxation of nanoparticles, proposed [259] as a novel tool for high-resolution *in vivo* diagnostics, while very sensitive, is associated with difficulties in back transforming the data to retrieve a high spatial resolution image. Magnetic particle imaging (MPI), in principle, overcomes these

limitations by using the magnetization response of superparamagnetic nanoparticles to generate a tomographic image that is characterized by both high spatial resolution and high sensitivity.

The concept [260] of MPI is straightforward as it depends on the nonlinearity of the magnetization curve for a superparamagnetic material and the fact that the magnetization is eventually saturated for any finite field, H_A, greater than the saturation field, H_s, i.e., $H_A > H_s$. In the absence of a static field that is constant over time, if the magnetic particles are subject to an oscillating or "modulating" field with frequency, f_o, and amplitude, H_f, their response, M(t), will vary with time and because it is non-linear, will contain higher harmonics (Fig. 19 (a)). Since the third[4] harmonic ($3f_o$) is strong and characteristic of the particle response, it can be exploited for signal detection. The other harmonic frequencies are separated from the signal by appropriate filtering. The spatial localization of the signal is accomplished by considering how the harmonic response varies when a static or time-constant magnetic field is superimposed on the modulating field. If the static field, H_A, is strong, the particle magnetization saturates and then the superposition of a small amplitude, $H_f \ll H_A$, modulating field results in a negligible change in the saturation magnetization. All the harmonics are then suppressed (Fig. 19).

To localize the MPI signal and to implement a spatial encoding scheme, these differences are exploited by superimposing a spatially varying static field, called the selection field on the modulating field. The selection field (Fig. 19(c)) is such that it vanishes at the center of the imaging device (referred to as the zero-field point or ZFP) and increases very rapidly in magnitude towards the edges (a strong field gradient is desirable). As a result, when the magnetic particles or tracers occupy the ZFP they produce a strong MPI signal. However, because of the large spatial field gradient any magnetic particle away from the ZFP would be magnetically saturated and contribute nothing to the MPI signal. A tomographic image is then formed by simply moving the sample within the selection field gradient or, conversely, moving the ZFP through the sample volume. In summary, MPI images are truly quantitative and are obtained by directly mapping the harmonic signal from magnetic nanoparticles or tracers when subjected to a combination of an oscillating/modulating field and static but spatially varying field gradient. Both the sensitivity and the spatial resolution are determined by the magnetic characteristics, M(H), of the particles. The former is proportional to the saturation magnetization, M_s, and the latter depends on the susceptibility, $\chi(\omega)$, of the superparamagnetic particles. $\chi(\omega)$ also depends on the mode of relaxation (Néel or Brownian) and hence, on the operating magnetic anisotropy, K, as well. Most importantly, the particle characteristics should be optimized to match the frequency of the modulating field.

The selection field, in its simplest form, can be set up by two permanent magnets facing each other to generate the ZFP [260]. Alternatively, simultaneous acquisition of the signal from multiple voxels, in a manner similar to magnetic resonance imaging [261], can be accomplished in two dimensions by generating a zero-field line (ZFL) using a system of multiple coils assembled on a circle [262]. Moreover, in practice, slow physical movement of the sample through the ZFP can be replaced by applying drive fields that can move the ZFP in an accelerated fashion through the sample volume [263].

As a first approximation, the theoretical resolution, R, for the MPI system is given by

[4]To be general—Other harmonics may also be used for signal generation. In fact, the strengths of higher harmonics will determine the spatial resolution of MPI.

$$R=2\,H_{mf}/X_s \tag{6.13}$$

where H_{mf} is the modulating field strength at which the material produces substantial higher harmonics. A reasonable first approximation for H_{mf} is obtained by equating the thermal energy with the Zeeman energy of the magnetite nanoparticles, giving H_{mf} ~ 400 A/m (~ 0.5 mT μ_0^{-1}) for particles 30 nm in diameter. X_s is the largest spatial derivative of the selection field component and corresponds roughly to the point of half of the maximum of the derivative of the magnetization curve of the particle. A value of X_s ~ 3.4 Tm^{-1} μ_0^{-1} (or 2.7 MA/m^2) is reasonable for the same particles giving R ~ 0.3 mm. In initial, proof-of-principle experiments, comparing the measured performance to the Langevin theory, applicable to these superparamagnetic magnetite nanoparticles, it was estimated [260] that the detection limit of the system was ~ 10 μmol Fe L^{-1} at a resolution of 1 mm. This is well within the dosage range allowed for medical use [81]. However, it is suggested that further improvements in the monodispersity of the magnetite nanoparticles and the recording electronics can lower the detection limits to 20 nmol Fe L^{-1}. These estimates of the detection limits are based on a comparison of the effective magnetization of MPI with MRI and neglects the dependence of the resolution on the signal to noise ratio (SNR). In fact, assuming that all the noise sources in the MPI system can be combined into a single source and represented by the resistance of the recording coils, the performance of the MPI system has been simulated [264]. Even though the resistance of the coils due to eddy current losses in the patient varies as the square of the frequency [265], an upper bound of the value of the noise at a frequency of 1 MHz was used. It was shown that a SNR ~10 in MPI can be achieved at 1 mm resolution for a concentration of 10 μmol Fe L^{-1} of 20 nm diameter magnetite nanoparticles [266] (Fig. 19(d)).

It is clear that the MPI signal strength and spatial resolution are both determined by the magnitude of the harmonic signal, which in turn, depends on the magnetization curve of the nanoparticles used as tracers. The magnetization curve of superparamagnetic particles, subject to an alternating field can be modeled using the Langevin function, $\mathcal{L}(\alpha)$, as

$$\frac{M}{M_0}=\int_0^\infty(\chi'-i\chi'')\mathcal{L}\left(\frac{\mu_0 v M_s H}{k_B T}\right)p(y)dy \tag{6.14}$$

modified to include the complex susceptibility, which is a function of the effective relaxation time, τ, arising from the Néel and Brownian processes. A log-normal size distribution, $p(y)$, has also been assumed. For these magnetite nanoparticles, the relationship between the third harmonic response and the MPI signal strength has been modeled [266] for an alternating field amplitude of 10 mT μ_0^{-1} at 50 kHz (f_0) and a simple sinusoidal receiving coil, consisting of 40 turns of wire wound around a 10 mm diameter NMR tube, tuned to resonate at 150 kHz ($3f_0$). Neglecting sample losses which are relatively small, the SNR per volume of magnetic particles, SNR_v, can be expressed as the ratio of the induced *emf* in the coil to the Johnson noise [267]

$$SNR_v=\frac{6\pi f_0 M_3 B_{axial}}{\sqrt{4k_B T R_{coil}\Delta f}} \tag{6.15}$$

where M_3 is the magnitude of the third harmonic of the magnetic nanoparticle magnetization in A/m, B_{axial} is the axial field produced by unit current in the receiving coil (2.25 mTμ_0^{-1}

A^{-1}), T is the coil temperature in Kelvin, R_{coil} is the AC coil resistance (0.238 Ohm), and Δf is the bandwidth of the receiver (1 kHz). The SNR performance as a function of particle size and frequency (Fig. 19(d)), including additional losses to account for the skin effect [268] at higher frequencies (R_{coil} ~ 0.836 Ohms at 1.5 Mhz ($3f_0$) and R_{coil} ~ 2.7 Ohms at 15 Mhz ($3f_0$)), shows that for a fixed frequency MPI system, there exists a maximum achievable sensitivity corresponding to an optimal nanoparticle size. Generally, the optimum particle size will be the largest particle that exhibits a magnetic relaxation time shorter than the period of the driving AC field. For the calculated optimal size of 16 nm (diameter), assuming that K = 25 kJ/m^3 and an alternating field amplitude of 10 mT μ_0^{-1} the predicted SNR is 1.1×10^{16} per particle volume. For a SNR ~5, this requires only 4.5×10^{-16} m^3 of materials or 2.4×10^{-9} g of magnetite. Finally, unlike sensitivity, the spatial resolution has no frequency dependence but depends on the particle size and the sharpness of the field gradient. As such, the resolution can be improved either by using larger particles or by reducing the RF field amplitude, with the understanding that sensitivity will suffer if the chosen particle diameter exceeds the optimum value.

To further test the modeling work described above, MPI signal performance was measured [269] using a custom-built transceiver that was specially designed for detecting the third harmonic of nanoparticle magnetization. During its operation, sample harmonics are excited using an air-cooled solenoid that is driven at 250 kHz using a commercial radio-frequency (RF) amplifier (Hotek Technologies, Model AG1017L). Harmonics are then detected using a smaller receiver coil and counter-windings that both reside coaxially inside. To narrow receiver bandwidth and provide optimal power transfer for harmonic detection, the receiver coil is tuned and matched to 50 Ω at 750 kHz. Induced harmonics are also amplified using ~24 dB of gain before detection with a commercial spectrum analyzer (Rohde & Schwarz, Model FSL303). During testing, the transceiver transmitter coil was driven with 10 W of RF power. To assess measurement variability, MPI signal testing was performed in triplicate. For each triplicate, 3 small cuvettes were filled with 100 μl of sample and their concentrations were measured. Sample cuvettes were then inserted into the transceiver coils. A peak in the harmonic signal vs. diameter is observed (Fig. 19(e)) indicating that there is an optimum nanoparticle diameter of ~15 nm for MPI at 250 kHz and in fact, choosing 15 nm particles leads to 30-fold gains in MPI signal per mg Fe over commercially available particles. While our best sample gives substantial improvement over commercial agents, its efficiency for MPI imaging at 250 kHz can be even further improved by narrowing its size distribution. We expect at least a factor of two improvements in efficiency by reducing σ from 0.22 to our targeted value of 0.1.

In summary, magnetic particle imaging compares very well with existing molecular imaging tools (Table II) that use a variety of electromagnetic radiation. Its projected spatial resolution is comparable to that of computed X-ray tomography, and if its sensitivity can be further enhanced it is expected to be as good as positron emission tomography. Moreover, the imaging is quantitative and can be obtained in real time; all these attributes make it a very promising development.

VII. Outlook and Challenges

The broad outlook for biomedical nanomagnetics is very promising as it moves into the next phase of innovative translational research with emphasis on development of quantitative *in vivo* imaging, targeted and triggered drug release, and image guided therapy including validation of delivery and therapy response. To be clinically successful, as has been discussed earlier, in addition to optimizing the physical properties of the nanoparticles or their surface modifications, it requires coordinated advances in multiple disciplines and methodologies including imaging, nanomagnetics, drug delivery, toxicity, particokinetics and pharmacological studies.

The first strategic objective is to tailor the properties of the nanoparticle core for optimal magnetic response (static or dynamic) within the biological size constraints. Numerous alloys of Fe and Co can be readily synthesized in nanoparticle form with superior magnetic properties. However, most of these are not biocompatible and even though they may possess enviable magnetic properties, typically, they are not suitable for *in vivo* applications. An alternative, practically viable strategy is to take a well-known magnetic material, e.g., magnetite, that has already been approved for human use such that when its size-dependent magnetic characteristics are optimized and its surface suitably functionalized, following appropriate cytotoxicity and particokinetics studies, it stands a very high chance of being readily used *in vivo*. One of the limitations of using a ferrimagnetic material such as magnetite is its relatively low saturation magnetization. Many applications only require a large magnetic moment ($M = M_s V$). Increasing the volume eventually makes the nanoparticles ferromagnetic at room temperature and prone to agglomeration. One way to overcome the problem of agglomeration is to exploit the fabrication of larger synthetic antiferromagnetic elements by nanofabrication methods (Section III-D). In addition, even though shape anisotropy is known to play an important role in magnetism, very little work has been done in synthesizing and utilizing nanoparticles with non-spherical shapes. This is a promising avenue for further work.

The second vital objective for *in vivo* applications is to ensure that the nanoparticles used, including their surface functionalization, should not show any cytotoxicity, nor should they affect cellular physiology and normal cell functionality. Assessing the biocompatibility of the nanoparticles is a nontrivial task[157] and significant effort is required to work with and develop standard assays to assess cytotoxicity, cell viability, nanoparticle uptake, cellular morphology and proliferation, etc. Further, unlike chemical drugs, nanoparticles can diffuse, settle and agglomerate. In cell culture studies these can be shown to be a function of systemic and particle properties including their number density, viscosity, particle shape and size, etc. Such agglomeration can affect the magnetic behavior as well. Further, preliminary work [173] has shown that when rates of diffusion and gravitational particle delivery are included, the trends and magnitude of cellular dose as a function of particle size and density differ significantly from those implied by “concentration” doses.

The role of conjugating the nanoparticles with appropriate small molecules for specific targeting (ligand-targeted therapeutics, Section V) cannot be overemphasized. This is equally true for drug delivery, imaging and especially image-guided therapy. In fact, the successful development of the emerging technique of magnetic particle imaging (Section VI-E), which shows great promise, will depend significantly on effective conjugation of selective molecular targeting agents on nanoparticle surfaces. Last, but not least, much work is still required in functionalization, evaluating and ensuring that the nanoparticles are biocompatible and have sufficiently large circulation times.

A specific challenge for hyperthermia is to develop a nanoparticle/applicator combination that minimizes nanoparticle dose. To accomplish this, in addition to optimizing the physics of heating (Section VI-A), further developments in realistic heating models, including perfusion, and systematic studies with phantoms are required. Further, adjuvant therapy combining magnetic fluid hyperthermia (MFH) with chemo-radiation strategies appears to hold the greatest promise in oncology. A holy grail in the field is to combine MRI with MFH, perhaps using existing MRI machines. For protons (^{1}H), the gyromagnetic ratio for the nuclear spins, $\gamma = 2.67 \times 10^8$rads s^{-1} T^{-1} and hence, for a field, $B_0 = 1$ T, the Larmor precessional frequency, f_L, is in the radio frequency range, i.e., $f_L = \omega_L/2\pi = 42.57$ MHz. Since resonant frequencies of nanoparticles scale inversely with size, to combine the two would be difficult. Moreover, this will require the development of ultra-small nanoparticle magnetic agents, typically < 1 nm in diameter. If magnetite is used, with crystallographic lattice parameter $a \sim 0.8$ nm, this raises challenging questions about fundamental ferrimagnetic correlation in structures smaller than

the unit cell as well as the role of surface anisotropies in determining their magnetic behavior. Alternatively, a more promising approach would be to combine MFH with recently proposed machines for MPI.

Finally, for *in vivo* applications, studies of the eventual biodistribution and clearance of the nanoparticles from the body are of paramount importance.

Acknowledgments

This work was supported in part by NSF, NIH, Murdock Charitable Trust, and the Guggenheim Foundation. I would also like to acknowledge the Rockefeller Bellagio Residency Fellowship and the Whitely Center where parts of this paper were written.

In the last decade, I have been very fortunate to have an outstanding group of students, post-docs and collaborators involved in this work. Specifically, I would like to acknowledge the contributions of my current and former students and post-docs: Prof. Yuping Bao, Dr. Marcela Gonzales, Yi-cheng Lee, Amit Khandhar, Mathew Ferguson, Tianlong Wen, Dr. Saikat Mandal, Dr. Suchita Kalale, Dr. A. B. Pakhomov; and collaborators Dr. M. Zeisberger, Prof. R. Narain, Prof. P. Stayton, Prof. A. S. Hoffman, Dr. A. Koretsky, Dr. L. Mitsumori, Prof. H. Calderon, Prof. D. Shindo, Dr. K. Minard, Dr. J. Simon and Prof. M. Rosenfeld. I am deeply indebted to all of them. Special thanks also to Prof. A. P. Alivisatos for introducing me to the field of nanoparticle synthesis and to Prof. U. O. Hafeli for a critical reading of this manuscript.

Last, but not least, I would like to acknowledge the IEEE Magnetics Society for the recognition as its Distinguished Lecturer in 2009. This manuscript is based largely on the contents of that lecture that I delivered in various forms to enthusiastic audiences in numerous institutions and chapters in over 20 countries.

References

1. Li KCP, Pandit SD, Guccione S, Bednarski MD. Molecular imaging applications in nanomedicine. Biomed Microdevelop 2004;6:113–116.
2. Subhankar B, Wolfgang K. Supermagnetism. J Phys D 2009;42:013001.
3. Gilchrist RK, et al. Selective inductive heating of lymph nodes. Ann Surg 1957;146:596–606. [PubMed: 13470751]
4. Maier-Hauff K, Rothe R, Scholz R, Gneveckow U, Wust P, Thiesen B, Feussner A, Deimling AV, Felix R, Jordan A. Intracranial thermotherapy using magnetic nanoparticles combined with external beam radiotherapy: Results of a feasibility study on patients with glioblastoma multiforme. J Neuro-Oncology 2007;81:53–60.
5. Hahn, GM. Hyperthermia and Cancer. New York: Plenum; 1982.
6. Ito A, Shinkai M, Honda H, Kobayashi T. Medical application of functionalized magnetic nanoparticles. J Biosci Bioeng 2005;100:1–11. [PubMed: 16233845]
7. Pankhurst QA, Connolly J, Jones SK, Dobson J. Applications of magnetic nanoparticles in biomedicine. J Phys D 2003;36:R167–R181.
8. Katz E, Willner I. Integrated nanoparticle-biomolecule hybrid systems: Synthesis, properties, and applications. Angew Chem Int Ed 2004;43:6042–6108.
9. Häfeli, UO. Smart nanoparticles in nanomedicine. In: Arshady, R.; Kono, K., editors. MML Series. Vol. 8. London, U.K.: Kentus Books; 2006. p. 77-126.
10. Andrä, W., et al. Application of magnetic particles in medicine and biology. In: Kronmüller, H.; Parkin, S., editors. Handbook of Magnetism and Advanced Magnetic Materials. Vol. 4. Chichester: Wiley; 2007.
11. Schütt A, et al. Applications of magnetic targeting in diagnosis and therapy—Possibilities and limitations: A mini-review. Hybridoma 1997;16:109–117. [PubMed: 9085137]
12. Falkenhagcn MD. Small particles in medicine. Artif Organs 1995;19:792–794. [PubMed: 8572997]
13. Harisinghani M, Barentsz J, Hahn PF, Deserno WM, Tabatabaei S, van de Kaa CH, de la Rosette J, Weissleder R. Noninvasive detection of clinically occult lymph-node metastases in prostate cancer. New Eng J Med 2003;348:2491–2499. [PubMed: 12815134]

14. Morawski AM, Lanza GM, Wickline SA. Targeted nanoparticles for quantitative imaging of sparse molecular epitopes with MRI. Magn Reson Med 2004;51:480–486. [PubMed: 15004788]
15. Kircher MF, Mahmood U, King RS, Weissleder R, Josephson L. A multimodal nanoparticle for preoperative magnetic resonance imaging and intraoperative optical brain tumor delineation. Cancer Res 2003;63:8122–8125. [PubMed: 14678964]
16. Massoud TF, Gambhir SS. Molecular imaging in living subjects: Seeing fundamental biological processes in a new light. Genes Dev 2003;17:545–580. [PubMed: 12629038]
17. Edmonds, DT. Electricity and Magnetism in Biological Systems. Oxford, U.K.: Oxford Univ Press; 2001.
18. Hafeli, U., et al. Scientific and Clinical Applications of Magnetic Carriers. New York: Plenum; 1997.
19. Blakemore R. Magnetotactic bacteria. Science 1975;190:377–379. [PubMed: 170679]
20. Wiltschko, R.; Wiltschko, W. Magnetic Orientation in Animals. Berlin; Springer: 1995.
21. Johnson S, Lohmann KJ. The physics and neurobiology of magnetoreception. Nature Rev Neurosci 2005;6:703–712. [PubMed: 16100517]
22. Rosensweig RE. Magnetic fluids. Sci Amer 1982;247:136–145.
23. Feldheim, DL.; Foss, CA, Jr. Metal Particles: Synthesis, Characterization and Applications. New York: Marcel Dekker; 2002.
24. Hyeon T. Chemical synthesis of magnetic nanoparticles. Chem Commun 2003:927–934.
25. Sun S, Zeng H. Size-controlled synthesis of magnetite nanoparticles. J Amer Chem Soc 2002;124:8204–8205. [PubMed: 12105897]
26. Puntes VF, Krishnan KM, Alivisatos PA. Colloidal nanocrystal size and shape control: The case of Co. Science 2001;291:2115. [PubMed: 11251109]
27. Berube, DM. Nanohype: The Truth Behind the Nanotechnology Buzz. New York: Prometheus; 2005.
28. Fujii T, Kaito T. Microsci Microanal 2005;11(suppl. 2):810.
29. Sproull, RL. Modern Physics. New York: Wiley;
30. Owens, FJ.; Poole, CP, Jr. Physics and Chemistry of Nanosolids. New York: Wiley; 2007.
31. Milbrook, GJ. Schrodinger's Machines: The Quantum Technology Shaping Everyday Life. New York: W.H. Freeman; 1997.
32. Falicov LM, Pierce DT, Bader SD, Gronsky R, Hathaway KB, Hopster HJ, Lambeth DN, Parkin SSP, Prinz G, Salamon M, Schuller IK, Victora RH. Surface, interface, and thin-film magnetism. J Mater Res 1990;5:1299.
33. Oesterhelt F, Oesterhelt D, Pfeiffer M, Engel A, Gaub H, Müller DJ. Unfolding pathways of individual bacteriorhodopsins. Science 2000;288:143–146. [PubMed: 10753119]
34. Himpsel FJ, Ortega JE, Mankey GJ, Willis RF. Magnetic nano-structures. Adv Phys 1998;47:511.
35. Kronmuller, H.; Seeger, A., editors. Modern Problems in Metal Physics II. Berlin: Springer; 1966.
36. Kittel C. Physical theory of ferromagnetic domains. Rev Mod Phys 1949;21:541–583.
37. Krishnan KM, Pakhomov AB, Bao Y, Blomqvist P, Chun Y, Gonzales M, Griffin K, Ji X, Roberts BK. Nanomagnatism and spin electronics: Materials, microstructure and novel properties. J Mater Sci 2006;41:793–815.
38. Frei EH, Shtrikman S, Treves D. Critical size and nucleation field of ideal. Ferromagnetic particles. Phys Rev 1957;106:446–455.
39. Bean CP. Hysteresis loops of mixtures of ferromagnetic micropowders. J Appl Phys 1955;26:1381–1383.
40. Jain RK. The next frontier of molecular medicine: Delivery of therapeutics. Nature Med 1998;4:655–657. [PubMed: 9623964]
41. Silva GA. Nanotechnology approaches for drug and small molecule delivery across the blood brain barrier. Surg Neurol 2007;67:113–116. [PubMed: 17254859]
42. Netti PA, Baxter LT, Boucher Y, Skalak R, Jain RK. Time-dependent behavior of interstitial fluid pressure in solid tumors: Implications for drug delivery. Cancer Res 1995;55:5451–5458. [PubMed: 7585615]
43. Klibanov AL, Maruyama K, Beckerleg AM, Torchilin VP, Huang L. Activity of amphipathic poly, ethylene glycol. 5000 to prolong the circulation time of liposomes depends on the liposome size and

is unfavorable for immunoliposome binding to target. Biochim Biophys Acta 1991;1062:142–148. [PubMed: 2004104]

44. Ratner, B.; Hoffman, AS.; Schoen, FJ.; Lemons, JE., editors. Biomaterials Science. San Diego, CA: Academic Press; 1996.
45. Perry MM, Gilbert AB. Yolk transport in the ovarian follicle of the hen, Gallus domesticus.: Lipoprotein-like particles at the periphery of the oocyte in the rapid growth phase. J Cell Sci 1979;39:257–272. [PubMed: 231041]
46. Boyles J, Bainton DF. Changes in plasma-membrane-associated filaments during endocytosis and exocytosis in polymorphonu-clear leukocytes. Cell 1981;24:906–914.
47. Weissleder R, Bogdanov A, Neuwelt EA, Papisov M. Long-circulating iron oxides for MR imaging. Adv Drug Del Rev 1995;16:321–334.
48. Okuhata Y. Delivery of diagnostic agents for magnetic resonance imaging. Adv Drug Del Rev 1999;37:121–137.
49. Matsumura Y, Maeda H. A new concept for macromolecular therapeutics in cancer-chemotherapy —Mechanism of tumoritropic accumulation of proteins and the antitumor agent smancs. Cancer Res 1986;46:6387–6392. [PubMed: 2946403]
50. Jain RK. Delivery of molecular and cellular medicine to solid tumors. Adv Drug Del Rev 2001;46:149–168.
51. Yatvin MB, Kreutz W, Horwitz BA, Shinitzky M. pH sensitive liposomes—Possible clinical implications. Science 1980;210:1253–1255. [PubMed: 7434025]
52. Sullivan SM, Huang L. Preparation and characterization of heat-sensitive immunoliposomes. Biochim Biophys Acta 1985;812:116–126. [PubMed: 3967009]
53. Allemann E, Gurney R, Doelker E. Eur J Pharm Biopharm 1973;39:173.
54. Brigger I, Dubernet C, Couvreur P. Nanoparticles in cancer therapy and diagnosis. Adv Drug Del Rev 2002;54:631–651.
55. Klibanov AL, Maruyama K, Torchilin VP, Huang L. Amphipathic polyethyleneglycols effectively prolong the circulation time of liposomes. FEBS Lett 1990;268:235–237. [PubMed: 2384160]
56. Larson DR, et al. Water-soluble quantum dots for multiphoton fluorescence imaging in vivo. Science 2003;300:1434–1436. [PubMed: 12775841]
57. Muller, RH.; Luck, M.; Harnisch, S.; Thode, K. Interaveneously Injected Particles Surface Properties and Interaction With Blood Proteins—The Key Determining the Organ Distribution. New York: Plenum Press; 1997.
58. Mitragotri S, et al. Red blood cell-mimicking synthetic biomaterial particles. Proc Nat Acad Sci 2009;106:21495–21499. [PubMed: 20018694]
59. Hertzer G. Grain structure and magnetism of nanocrystalline ferromagnets. IEEE Trans Magn 1989;25:3327–3329.
60. Coey, JMD., editor. Rare-Earth Iron Permanent Magnets. Oxford, U.K.: Oxford Univ. Press; 1996.
61. Crew DC, Girt E, Guilot M, Suess D, Schrefl T, Krishnan KM. Magnetic interactions and reversal behavior of Nd2Fe14B particles diluted in a Nd matrix. Phys Rev B 2002;66:184418.
62. Chou SY, Krauss PR, Renstrom PJ. Nanoimprint lithography. J Vac Sci Technol B 1996;14:4129–4133.
63. Hu W, Wilson RJ, Xu L, Han SJ, Wang SX. Patterning of high density magnetic nanodot arrays by nanoimprint lithography. J Vac Sci Technol A 2007;25:1294–1297.
64. Ferrai M. Defined as “A hollow or solid structure, with diameter in the 1–1000 nm range, which can hold drugs and detection agents. Targeting moeties can also be attached to the surface,”. Nature Rev: Cancer 2005;5:161. [PubMed: 15738981]
65. LaMer VK, Dinegar RH. Theory, production and mechanism of formation of monodispersed hydrosols. J Amer Chem Soc 1950;72:4847–4854.
66. Buffat P, Borel JP. Size effect on the melting temperature of gold particles. Phys Rev A 1976;13:2287–2298.
67. Bao YP, An W, Turner CH, Krishnan KM. The critical role of surfactants in the growth of cobalt nanoparticles. Langmuir 2009;26:478–483. [PubMed: 19743830]

68. Murray CB, Norris DJ, Bawendi MG. Synthesis and characerization of nearly monodisperse CdE, E = S, Se, Te. Semiconductor nanocrystallites. J Amer Chem Soc 1993;115:8706–8715.
69. Yin Y, Alivisatos AP. Colloidal nanocrystal synthesis and the organic-inorganic interface. Nature 2005;437:664–670. [PubMed: 16193041]
70. Reiss H. The growth of uniform colloidal dispersions. J Chem Phys 1951;19:482–487.
71. Peng X, Wickham J, Alivisatos AP. Kinetics of II-VI and III-V colloidal semiconductor nanocrystal growth: "Focusing" of size distributions. J Amer Chem Soc 1998;120:5343–5344.
72. Murray CB, et al. Colloidal synthesis of nanocrystals and nanocrystal superlattices. IBM J Res Develop 2001;45:47–56.
73. Bao Y, Beerman M, Pakhomov AB, Krishnan KM. Controlled crystalline structure and surface stability of cobalt nanocrystals. J Phys Chem B 2005;109(no. 15):7220–7222. [PubMed: 16851825]
74. Murray CB, Kagan CR, Bawendi MG. Synthesis and characterization of monodisperse nanocrystals and close-packed nanocrystal assemblies. Annu Rev Mater Sci 2000;30:545–610.
75. Peng, et al. Shape control of CdSe nanocrystals. Nature 2000;404:59–61. [PubMed: 10716439]
76. Puntes VF, Krishnan KM, Alivisatos AP. Synthesis of colloidal cobalt nanoparticles with controlled size and shapes. Top Catalysis 2002;19:145–148.
77. Pudzer A, et al. The effect of organic ligand binding on the growth of CdSe nanoparticles probed by ab initio calculations. Nano Lett 2004;4:2361–2365.
78. Yin Y, Alivisatos AP. Colloidal nanocrystal synthesis and the organic-inorganic interface. Nature 2005;437:664–670. [PubMed: 16193041]
79. Puntes VF, Zanchet D, Erdonmez C, Alivisatos AP. Synthesis of hcp-Co nanodisks. J Amer Chem Soc 2002;124:12874–12880. [PubMed: 12392435]
80. Muldoon LL, Sandor M, Pinkston KE, Neuwelt EA. Imaging, distribution, and toxicity of superparamagnetic iron oxide magnetic resonance nanoparticles in the rat brain and intracerebral tumor. Neurosurgery 2005;57:785–796. [PubMed: 16239893]
81. Weissleder R, Stark DD, Engelstad BL, Bacon BR, Compton CC, White DL, Jacobs P, Lewis J. Superparamagnetic iron oxide: Pharmacokinetics and toxicity. Amer J Roentgenol 1989;152:167–73. [PubMed: 2783272]
82. Bacon BR, Stark DD, Park CH, Saini S, Groman EV, Hahn PF, Compton CC, Ferrucci JT. Ferrite particles: A new magnetic resonance imaging contrast agent. Lack of acute or chronic hepatotoxicity after intravenous administration. J Lab Clin Med 1987;110:164–171. [PubMed: 3598345]
83. Geraldes CF, Laurent S. Classification and basic properties of contrast agents for magnetic resonance imaging. Contrast Media Mol Imag 2009;4:1–23.
84. Tartaj P. Encyclopedia of Nanoscience and Nanotechnology 2003;X:1–20.
85. Willard MA, Kurihara LK, Carpenter EE, Calvin S, Harris VG. Chemically prepared magnetic nanoparticles. Int Mater Rev 2004;49:125–170.
86. Massart R. Compt Rend Series C 1980;291:1–3.
87. Kang YS, Risbud S, Rabolt JF, Stroeve P. Synthesis and characterization of nanometer-size Fe3O4 and γ-Fe2O3. Chem Mater 1996;8:2209–2211.
88. Sapieszko RS, Matijevic E. Preparation of well-defined colloidal particles by thermal decomposition of metal chelates. J Colloid Interface Sci 1980;74:405.
89. Vijayakumar R, Koltypin Y, Felner I, Gedanken A. Sonochemical synthesis and characterization of pure nanometer-sized Fe3O4 particles. Mater Sci Eng Jun;2000 A286:101–105.
90. Inouye K, Endo R, Otsuka Y, Miyashiro K, Kaneko K, Ishikawa T. Oxygenation of ferrous-ions in reversed micelle and reversed micro-emulsion. J Phys Chem 1982;86:1465–1469.
91. Pileni MP. Nanosized particles made in colloidal assemblies. Langmuir 1997;13:3266–3276.
92. Klie RF, Browning ND. Characterization of oxygen ordering in, La, SrFeO3 by atomic resolution Z-contrast imaging and electron energy-loss spectroscopy. J Elect Microscopy 2002;51:S59–S66.
93. Gonzales M, Krishnan KM. Synthesis of magnetoliposomes with monodisperse iron oxide nanocrystal cores for hyperthermia. J Magn Magn Mater 2005;293:265–270.
94. Rockenberger J, Scher EC, Alivisatos AP. A new nonhydrolytic single-precursor approach to surfactant-capped nanocrystals of transition metal oxides. J Amer Chem Soc 1999;121:11595–11596.

95. Hyeon T, Lee SS, Park J, Chung Y, Na HB. Synthesis of highly crystalline and monodisperse maghemite nanocrystallites without a size-selection process. J Amer Chem Soc 2001;123:12798–12801. [PubMed: 11749537]
96. Gonzales-Weimuller, M. PhD thesis. University of Washington; Seattle: 2007.
97. Jana NR, Chen Y, Peng X. Size and shape controlled magnetic, Cr, Mn, Fe, Co, Ni oxide nanocrystals via a simple and general approach. Chem Mater 2004;16:3931–3935.
98. Krishnan KM. Atomic site and species determinations using channeling and related effects in analytical electron microscopy. Ultramicroscopy 1988;24:125–142.
99. Krishnan KM, Rez P, Thomas G. Crystallographic site occupancy refinements in thin film oxides by channeling enhanced microanalysis. Acta Crystallogr 1985;B41:396–405.
100. Krishnan KM. Fe L3/L2 near edge fine structure studies. Ultramicroscopy 1990;32:309.
101. Gonzales M, Krishnan KM. Phase transfer of highly monodisperse iron oxide nanocrystals with pluronic F127 for biological applications. J Magn Magn Mater 2007;311:59.
102. Euliss LE, et al. Cooperative assembly of magnetic nanoparticles and block copolypeptides in aqueous media. Nano Lett 2003;3:1489–1493.
103. Chandaroy P, Sen A, Alexandridis P, Hui SW. Utilizing temperature-sensitive association of Pluronic F-127 with lipid bilayers to control liposome-cell adhesion. Biochim Biophys Acta 2002;1559:32–42. [PubMed: 11825586]
104. Bao Y, Pakhomov AB, Krishnan KM. A general approach to synthesis of nanoparticles with controlled morphologies and magnetic properties. J Appl Phys 2005;97:10J317.
105. Liu Q, Xu Z, Finch JA, Egerton RA. Novel two-step silica-coating process for engineering magnetic nanoparticles. Chem Mater 1998;10:3936–3940.
106. Ulman A. Formation and structure of self-assembled monolayers. Chem Rev 1996;96:1533–1554. [PubMed: 11848802]
107. Lim JK, Eggeman A, Lanni F, Tilton RD, Majetich SA. Synthesis and single-particle optical detection of low-polydispersity plasmonic-super paramagnetic nanoparticles. Adv Mater 2008;20:1721–1726.
108. Jun L, Zhou W, Kumbhar J, Wiemann J, Fang J, Carpentier EE, O'Connor CJ. Gold coated iron, Fe@Au nanoparticles: Synthesis, characterization, and magnetic field induced self-assembly. J Solid State Chem 2001;159:26–31.
109. Cho S, Kauzlarich SM, Olamit J, Liu K, Grandjean F, Rebbouh L, Long GJ. Characterization and magnetic properties of core/shell structured Fe/Au nanoparticles. J Appl Phys 2004;95:6804–6806.
110. Lyon L, Fleming DA, Stone MB, Schiffer P, Williams ME. Synthesis of Fe oxide core/Au shell. Nanoparticles by iterative hy-droxylamine seeding. Nano Lett 2004;4:719–723.
111. Bao Y, Krishnan KM. Preparation of functionalized and gold-coated cobalt nanocrystals for biomedical applications. J Magn Magn Mater 2005;293:15–19.
112. Bao Y, Calderon H, Krishnan KM. Controlled synthesis and characterization of CocoreAushell nanoparticles with tailored optical and magnetic properties. J Phys Chem 2007;111:1941–1944.
113. Kashchiev D, Van Rosmalen GM. Review: Nucleation in solutions revisited. Cryst Res Technol 2003;38:555–574.
114. Kashchiev, D. Nucleation: Basic Theory With Applications. Oxford, U.K.: Butterworth-Heineman; 2000.
115. Bao, YP. PhD thesis. University of Washington; Seattle: 2005.
116. Mandal S, Krishnan KM. CocoreAushell nanoparticles: Evolution of magnetic properties in the displacement reaction. J Mater Chem 2007;17:372.
117. Park J, Kang EA, Bae CJ, Park JG, Noh HJ, Kim JY, Park JH, Park JH, Hyeon T. J Phys Chem B 2004;108:13594.
118. de Almeida JRL, Thouless DJ. Stability of the Sherrington-Kirkpatrick solution of a spin glass model. J Phys A: Math Gen 1978;11(no. 5):983–990.
119. Lee YC, Pakhomov A, Krishnan KM. Size-driven magnetic transitions in monodisperse MnO nanocrystals. J Appl Phys 2010;107:09E124.
120. Chatterji T, Su Y, Iles GN, Lee YC, Khandhar A, Krishnan KM. Antiferromagnetic spin correlations in MnO nanoparticles. J Magn Magn Mater. to be published.

121. Roberts KG, Varela M, Rashkeev S, Pantelides ST, Penny-cook SJ, Krishnan KM. Manipulating the magnetic structure of Co Core/CoO shell nanoparticles: Implications for controlling the exchange bias. Phys Rev B 2008;78:014409.
122. Griffin KA, Pakhomov AB, Wang CM, Heald SM, Krishnan KM. Intrinsic ferromagnetism in insulating cobalt doped anatase TiO[sub 2]. Phys Rev Lett 2005;94:157204. [PubMed: 15904182]
123. Lee Y, Tucciarone J, Koretsky AP, Krishnan KM. Dissolution of manganese oxide nanocrystals as MRI-T1 contrast agents. J Magn Magn Mater. submitted for publication.
124. Lang C, Schler D. Biogenic, Nanoparticles: Production, characterization, and application of bacterial magnetosomes. J Phys: Condens Mater 2006;18:S2815–S2828.
125. Lang C, Schuler D, Faivre D. Synthesis of magnetite nanoparticles for bio- and nanotechnology: Genetic engineering and biomimetics of bacterial magnetosomes. Macromol Biosci 2007;7:144–151. [PubMed: 17295401]
126. Klem MT, Young M, Douglas T. Mater Today Sep;2005 :28.
127. Kramer RM, Li C, Carter DC, Stone MO, Naik RR. Engineered protein cages for nanomaterial synthesis. J Amer Chem Soc 2004;126:13282–13286. [PubMed: 15479082]
128. Reiss BD, Mao C, Solis DJ, Ryan KS, Thomson T, Belcher AM. Biological routes to metal alloy ferromagnetic nanostruc-tures. Nano Lett 2004;4:1127–1132.
129. Klem MT, Willits D, Solis DJ, Belcher AM, Young M, Douglas T. Bio-inspired synthesis of protein-encapsulated CoPt nanoparticles. Adv Funct Mater 2005;15:1489–1494.
130. Horák D, Babič M, Macková H, Beneŝ MJ. Preparation and properties of magnetic nano- and microsized particles for biological and environmental separations. J Sep Sci 2007;30:1751–1772. [PubMed: 17623453]
131. Chou SY, Krauss PR, Renstrom PJ. Imprint lithography with 25-nanometer resolution. Science 1996;272:85.
132. Hu W, Wilson CRJ, Koh A, et al. High-moment anti-ferromagnetic nanoparticles with tunable magnetic properties. Adv Mater 2008;20:1479–1481.
133. Bao Y, Beerman M, Krishnan KM. Controlled self-assembly of colloidal cobalt nanocrystals. J Magn Magn Mater 2003;266:L245.
134. Gao Y, Bao YP, Beerman M, Shindo D, Krishnan KM. Superstructures of self-assembled cobalt nanocrystals. Appl Phys Lett 2004;84:3361–3363.
135. Puntes VF, Krishnan KM. Synthesis, structural order and magnetic behavior of self-assembled e-Co nanocrystal arrays. IEEE Trans Magn 2001;37:2210–2212.
136. Leslie-Pelecky DL, Rieke RD. Magnetic properties of nanostructured materials. Chem Mater 1996;8:1770–1783.
137. Dormann, JL.; Fiorani, D.; Tronc, E. Studies of the Magnetic Properties of Fine Particles and Their Relevance to Materials Science. New York: Elsevier; 1992.
138. Pusey PN, van Megen W. Phase-behaviour of concentrated suspensions of nearly hard colloidal spheres. Nature 1986;320:340–342.
139. Woodstock LV. Nature 1997;385:141–143.
140. Wang ZL, Dai ZR, Sun S. Polyhedral shapes of cobalt nanocrystals and their effect on ordered nanocrystal assembly. Adv Mater 2000;12:1944–1946.
141. Kaplan PD, Rouke JL, Yodh AG, Pine DJ. Entropically driven surface phase separation in binary colloidal mixtures. Phys Rev Lett 1994;72:582–585. [PubMed: 10056469]
142. Gao Y, Bao Y, Pakhomov AB, Shindo D, Krishnan KM. Spiral spin order of self-assembled Co nanodisk arrays. Phys Rev Lett 2006;96:137205. [PubMed: 16712029]
143. Nie S, Xing Y, Kim GJ, Simons JW. Nanotechnology applications in cancer. Ann Rev Biomed Eng Aug;2007 9:257–288. [PubMed: 17439359]
144. Langer R. Drug delivery and targeting. Nature 1998;392:5–10. [PubMed: 9579855]
145. Hanahan D, Weinberg RA. The hallmarks of cancer. Cell 2000;100(no. 1):57–70. [PubMed: 10647931]
146. Srinivas PR, Barker P, Srivastava S. Nanotechnology in early detection of cancer. Laboratory Investigation 2002;82(no. 5):657–662. [PubMed: 12004006]

147. Allen TM. Ligand-targeted therapeutics in anticancer therapy. Nature Rev Cancer 2002;2:750–763. [PubMed: 12360278]

148. Bouck N, Stellmach V, Hsu SC. How tumors become angiogenic. Adv Cancer Res 1996;69:135–174. [PubMed: 8791681]

149. Marshall E. Setbacks for Endostatin. Science Mar;2002 295(no. 5563):2198–2199. [PubMed: 11910086]

150. Couzin J. Nanoparticles cut tumors' supply lines. Science 2002;296:2314–2315. [PubMed: 12089416]

151. Mousa SA, Bergh JJ, Dier E, Rebbaa A, O'Connor LJ, Yalcin M, Aljada A, Dyskin E, Davis FB, Lin HY, Davis PJ. Tetraiodothyroacetic acid, a small molecule integrin ligand, blocks angiogenesis induced by vascular endothelial growth factor and basic fibroblast growth factor. Angiogenesis 2008;11:183–190. [PubMed: 18080776]

152. Mizejewski GJ. Role of integrins in cancer: Survey of expression patterns. Proc Soc Exp Biol Med 1999;222:124–138. [PubMed: 10564536]

153. Hood JD, Bednarski M, Frausto R, Guccione S, Reisfeld RA, Xiang R, Cheresh DA. Tumor regression by targeted gene delivery to the neovasculature. Science 2002;296:2404–2407. [PubMed: 12089446]

154. Matsumura Y, Maeda H. A new concept for macromolecular therapeutics in cancer chemotherapy: Mechanism of tumoritropic accumulation of proteins and the antitumor agent smancs. Cancer Res 1986;46:6387–6392. [PubMed: 2946403]

155. Yatvin MB, Kreutz W, Horwitz BA, Shinitzky M. pH-sensitive liposomes: Possible clinical implications. Science 1980;210(no. 4475):1253–1255. [PubMed: 7434025]

156. Sullivan SM, Huang L. Preparation and characterization of heat-sensitive immunoliposomes. Biochim Biophys Acta 1985;812(no. 1):116–126. [PubMed: 3967009]

157. Hafeli, UO.; Aue, J.; Damani, J. Laboratory Techniques in Biochemistry and Molecular Biology. In: Zborowski, M.; Chalmers, JJ., editors. Magnetic Cell Separation, ch 7. Vol. 32. New York: Elsevier; 2008.

158. Mulder, GJ.; Decker, L. Pharmaceutical Toxicology. London, U.K.: Pharmaceutical Press; 2006.

159. Gilmour PS, Ziesenis A, Morrison ER, Vickers MA, Drost EM, Ford I. Pulmonary and systemic effects of short-term inhalation exposure to ultrafine carbon black particles. Toxicol Appl Pharmacol 2004;195:35–44. [PubMed: 14962503]

160. Kreyling WG, Semmler-Behnke M, Möller W. Health implications of nanoparticles. J Nanopart Res 2006;8:543–562.

161. Yin H, Too HP, Chow GM. The effects of particle size and surface coating on the cytotoxicity of nickel ferrite. Biomaterials 2005;26:5818–5826. [PubMed: 15949547]

162. Hu F, Neoh KG, Cen L, Kang ET. Cellular response to magnetic nanoparticles “PEGylated” via surface-initiated atom transfer radical polymerization. Biomacromolecules 2006;7:809–816. [PubMed: 16529418]

163. Hafeli UO. Mol Pharm 2009;6(no. 5):1417–1428. [PubMed: 19445482]

164. Feride C. Interactions entre cellules et nanoparticules fonctionnal-isées. J Pharmacol Exp Ther 2006;318:108–116. [PubMed: 16608917]

165. Valko M, Morris H, Cronin MTD. Metals, toxicity and oxidative stress. Curr Med Chem 2005;12:1161–1209. [PubMed: 15892631]

166. Russell, WMS.; Burch, RL. The Principles of Humane Experimental Technique. London, U.K.: Methuen; 1959.

167. Soenen SJH, De Cuyper M. Assessing cytotoxicity of (iron oxide-based) nanoparticles: An overview of different methods exemplified with cationic magnetoliposomes. Contrast Media Mol Imag Oct; 2009 4(no. 5):207–219.

168. Carmichael J, DeGraff WG, Gazdar AF, Minna JD, Mitchell JB. Evaluation of a tetrazolium-based semiautomated colorimetric assay: Assessment of chemosensitivity testing. Cancer Res 1987:47936–47942.

169. Decker T, Lohmann-Matthes ML. A quick and simple method for the quantitation of lactate dehydrogenase release in the measurements of cellular cytotoxicity and tumor necrosis factor (TNF) activity. J Immunol Meth 1988;115(no. 1):61–69.

170. Denizot F, Lung R. Rapid color metric assay for cell growth and survival. J Immunol Meth 1986;89:271–277.

171. Legrand C. Lactate dehydrogenase (LDH) activity of the number of dead cells. J Biotechnol 1992;25:231–243. [PubMed: 1368802]

172. Mosmann T. Rapid colorimetric assay for cellular growth and survival: Application to proliferation and cytotoxicity assays. J Immunol Meth 1983;65:55–63.

173. Teeguarden JG, Hinderliter PM, Orr G, Thrall BD, Pounds JG. Particokinetics in vitro: Dosimetry considerations for in vitro nanoparticle toxicity assessments. Toxicol Sci 2007;95:300–312. [PubMed: 17098817]

174. Stern, S. Response to Questions on NCI Method GTA-2. Gonzales, M., editor. Vol. 1. Frederick, MD: 2007.

175. Ahmad S, Ahmad A, Schneider BK, White CW. Cholesterol interferes with the MTT assay in human epithelial-like (A549) and endothelial (HLMVE and HCAE) cells. Int J Toxicol 2006;25(no. 1): 17–23. [PubMed: 16510353]

176. Stern S, Potter T. NCL Method GTA-2 V.1 HEP G2 Hepatocarcinoma Cytotoxicity Assay. 2006

177. Gonzales M, Mitsumori L, Kushleika J, Rosenfeld M, Krishnan KM. Synthesis and cytotoxicity of monodisperse iron oxide nanoparticles made from the thermal decomposition of organometallics and aqueous phase transfer with Pluronic F127′. Contrast Media Mol Imag. 10.1002/cmmi.391

178. Crossgrove J, Zheng W. Manganese toxicity upon overexposure. NMR Biomed 2004;17:544–553. [PubMed: 15617053]

179. Wolf GL, Baum L. Cardiovascular toxicity and tissue proton T1 response to manganese injection in the dog and rabbit. Amer J Roentgenology 1983;141:193–197.

180. Aoki L, Wu YJL, Silva AC, Lynch RM, Koretsky AP. In vivo detection of neuroarchitecture in the rodent brain using manganese-enhanced MRI. NeuroImage 2004;22:1046–1059. [PubMed: 15219577]

181. Silva AC, Lee JH, Aoki L, Koretsky AR. Manganese-enhanced magnetic resonance imaging (MEMRI): Methodological and practical considerations. NMR Biomed 2004;17:532–543. [PubMed: 15617052]

182. Gilchrist RK. Selective inductive heating of lymph. Ann Surgery 1957;146:596–606.

183. Hahn GM. Hyperthermia for the engineer: A short biological primer. IEEE Trans Biomed Eng 1984;31:3–8. [PubMed: 6724607]

184. Wust P, Hildebrandt B, Sreenivasa G. Hyperthermia in combined treatment of cancer. Lancet Oncol 2002;3:487–497. [PubMed: 12147435]

185. Dewey, WC.; Freeman, ML.; Raaphorst, GP. Cell biology of hyperthermia and radiation. In: Meyn, RE.; Withers, HR., editors. Radiation Biology in Cancer Research. New York: Raven Press; 1980. p. 589-621.

186. Gerweck LE. Modification of cell lethality at elevated temperatures: The pH effect. Radiat Res 1977;70:224–235. [PubMed: 15298]

187. Jordan A, Scholz R, Schüler J, Wust P, Felix R. Arrhenius analysis of the thermal response of human colonic adenocarcinoma cells in vitro using the multi-target, single-hit and the linear-quadratic model. Int J Hyperthermia 1997;13(no. 1):83–88. [PubMed: 9024929]

188. Jordan A, Scholtz R, Wust P, Fähling H, Felix R. Magnetic fluid hyperthermia (MFH): Cancer treatment with AC magnetic field induced excitation of biocompatible superparamagnetic nanoparticles. J Magn Magn Mater 1999;201:413–419.

189. Bertone V, Barni S, Silvotti MG, Freitas I, Mathé G, et al. Hyperthermic effect on the human metastatic liver: A TEM study. Anticancer Res 1997;17:4713–4716. [PubMed: 9494594]

190. Christophi C, Winkworth A, Muralihdaran V. The treatment of malignancy by hyperthermia. Surg Oncol 1999;7:83–90. [PubMed: 10421511]

191. Werta A, Dewey WC. Relationship between growth rate, cell volume, cell cycle kinetics, and antigenic properties of cultured murine lymphoma cells. Int J Rad Biol 1970;19:467–477.

192. Hall, EJ.; Giaccia, EJ. Radiobiology for the Radiologist. 6th. CHIPS press; 2005.

193. Bull JMC. An update on the anticancer effects of a combination of chemotherapy and hyperthermia. Cancer Res 1984;44:4853–4856.

194. Dahl O. Interaction of hyperthermia and chemotherapy. Recent Results Cancer Res 1988;107:157–169. [PubMed: 3287520]

195. Overgaard J, Suit HD. Time-temperature relationship in hyperthermic treatment of malignant and normal tissue in vivo. Cancer Res 1979;39:3248–3253. [PubMed: 455307]

196. Urano M, Kuroda M, Nishimura Y. For the clinical application of thermochemotherapy. Int J Hyperther 1999;2:79–107.

197. Yanase M, Shinkai M, Honda H, Wakabayashi T, Yoshida J, Kobayashi T. Antitumor immunity induction by intracellular hyperthermia using magnetite cationic liposomes. Jpn J Cancer Res 1998;89:775–782. [PubMed: 9738985]

198. Ito A, Shinkai M, Honda H, Yoshikawa K, Saga S, Wakabayashi T, Yoshida J, Kobayashi T. Heat shock protein 70 expression induces antitumor immunity during intracellular hyperthermia using magnetite nanoparticles. Cancer Immunol Immunother 2003;52:80–88. [PubMed: 12594571]

199. Ito A, Shinkai M, Honda H, Wakabayashi T, Yoshida J, Kobayashi T. Augmentation of MHC class I antigen presentation via heat shock protein expression by hyperthermia. Cancer Immunol Immunother 2001;50:515–522. [PubMed: 11776373]

200. Menoret A, Chandawarkar Semin R. Heat-shock protein-based anticancer immunotherapy: An idea whose time has come. Oncol 1998;25:654–660.

201. Srivastava PK, Menoret A, Basu S, Binder RJ, Mc-Quade KL. Heat shock proteins come of age: Primitive functions acquire new roles in an adaptive world. Immunity 1998;8:657–665. [PubMed: 9655479]

202. Tilly W, Wust P, Rau B, Harder C, Gellermann J, Schlag P, Budach V, Felix R. Temperature data and specific absorption rates in pelvic tumours: Predictive factors and correlations. International Journal of Hyperthermia: The Official Journal of European Society for Hyperthermic Oncology, North American Hyperthermia Group 2001;17(no. 2):172–188.

203. Vaupel P, Kallinowski FPO. Blood flow, oxygen and nutrient supply, and microenvironment of human tumors, a review. Cancer Res 1989;49:6449–6465. [PubMed: 2684393]

204. van der Zee J, González González D, van Rhoon GC, van Dijk JD, van Putten WL, Hart AA. Comparison of radiotherapy alone with radiotherapy plus hyperthermia in locally advanced pelvic tumours: A prospective, randomised, multicentre trial. Dutch Deep Hyperthermia Group. Lancet 2000;355(no. 9210):1119–1125. [PubMed: 10791373]

205. Henle KJ. Sensitization to hyperthermia below 43 °C. Cancer Inst 1980;64:1479–1483.

206. Gerner EW, Schneider MJ. Induced thermal resistance in HeLa cells. Nature 1976;256:500–502. [PubMed: 1160994]

207. Henle KJ, Leeper DB. Interaction of hyperthermia and radiation in CHO cells: Recovery kinetics. Radiat Res 1976;66:505–518. [PubMed: 935340]

208. Schlesinger MJ. Heat shock proteins. J Biol Chem 1990;265:12111–12114. [PubMed: 2197269]

209. Li GC, Mivechi NF, Weitzel G. Heat shock proteins, thermotolerance, and their relevance to clinical hyperthermia. International Journal of Hyperthermia: The Official Journal of European Society for Hyperthermic Oncology, North American Hyperthermia Group 1995;11(no. 4):459–488.

210. Hahn GM. Cells and transformants with their survival responses to hyperthermia and to amphotericin B. Cancer Res 1980;40:3763–3767. [PubMed: 7438060]

211. Chantrell RW, Popplewell J, Charles SW. Measurements of particle size distribution parameters in ferrofluids. IEEE Trans Magn 1978;MAG-14:975–977.

212. A. Khandhar and K. M. Krishnan, unpublished.

213. nanoTherics, magneThermTM System.

214. Brezovich IA. Low frequency hyperthermia: Capacitive and ferromagnetic thermoseed methods. Med Phys Monograph 1988;16:82–111.

215. Gupta AK, Gupta M. Synthesis and surface engineering of iron oxide nanoparticles for biomedical applications. Biomaterials Jun;2005 26(no. 18):3995–4021. [PubMed: 15626447]

216. Kreuter J. Physicochemical characterization of polyacrylic nanoparticles. J Controlled Release 1991;16:169–176.
217. Housnia A, Narain R. Aqueous solution behavior of p(N-isopropyl acrylamide) in the presence of water-soluble macromolecular species. Eur Polym J 2007;43:4344–4354.
218. Hoffman AS, Stayton PS. Bioconjugates of smart polymers and proteins: Synthesis and applications. Macromol Symp 2004;207:139–151.
219. Le TPT, Moad G, Rizzardo E, Thang SH. Chem Abstr 1998;128:115390.
220. Narain R, Gonzales M, Hoffman AS, Stayton PS, Krishnan KM. Synthesis of monodisperse biotinylated p(NIPAAm)-coated iron oxide magnetic nanoparticles and their bioconjugation to streptavidin. Langmuir 2007;23:6299–6304. [PubMed: 17451262]
221. Jana NR, Chen Y, Peng X. Size- and shape-controlled magnetic (Cr, Mn, Fe, Co, Ni) oxide nanocrystals via a simple and general approach. Chem Mater 2004;16:3931–3935.
222. Kalele S, Narain R, Krishnan KM. Probing temperature-sensitive behavior of pNIPAAm-coated iron oxide nanoparticles using frequency-dependent magnetic measurements. J Magn Magn Mater May;2009 321:1377–1380.
223. Bucak S, Jones DA, Laibinis PE, Hatton TA. Protein separations using colloidal magnetic nanoparticles. Prog 2003;19:477–484.
224. Pamme N, Wilhelm C. Continuous sorting of magnetic cells via on-chip free-flow magnetophoresis. Lab Chip 2006;6:974–980. [PubMed: 16874365]
225. Safarik I, Safarikova M. Use of magnetic techniques for the isolation of cells. J Chromatography B 1999;722:33–53.
226. Larsson K, Kriz K, Kriz D. Magnetic transducers in biosensors and bioassays. Analusis Sep;1999 27, Biosensors(no. 7):617–621.
227. Chung SH, Hoffmann A, Bader SD. Biological sensors based on Brownian relaxation of magnetic nanoparticles. Appl Phys Lett 2004;85:2971–2973.
228. Bao Y, Pakhomov AB, Krishnan KM. Brownian magnetic relaxation of water-based cobalt nanoparticles. J Appl Phys 2006;99:08H107.
229. Connolly J, St Pierre T. Proposed biosensors based on the time dependent properties of magnetic fluids. J Magn Magn Mater 2001;225:156–160.
230. Kötitz R, Weitschies W, Trahms L, Brewer W, Semmler W. Determination of the binding reaction between avidin and biotin by relaxation measurements of magnetic nanoparticles. J Magn Magn Mater 1999;194:62–68.
231. Nelson KL, Runge VM. Basic principles of MR contrast. Top Magn Reson Imag 1995;7:124–136.
232. Hendrick RE, Haacke EM. Basic physics of MR contrast agents and maximization of image contrast. J Magn Reson Imag 1993;3:137–148.
233. Runge VM, Stewart RG, Clanton JA. Paramagnetic agents for contrast-enhanced NMR imaging: A review. Amer J Roentgenol 1983;141:1209–1215. [PubMed: 6606318]
234. Weinmann HJ, Brash RC, Press WR. Characteristics of gadolinium-DTPA complex: A potential NMR contrast agent. Amer J Roentgenol 1984;142:619–624. [PubMed: 6607655]
235. Runge VM, Clanton JA, Herzer WA. Intravascular contrast agents suitable for magnetic resonance imaging. Radiology 1984;153:171–176. [PubMed: 6433402]
236. Kirsch JE, John K. Basic principles of magnetic resonance contrast agents. Top Magn Reson Imag Mar;1991 3(no. 2):1–18.
237. Fahlvik AK, Klaveness J, Stark DD. Iron oxides as MR imaging contrast agents. J Magn Reson Imag 1993;3:187–194.
238. Wang YXJ, Hussain SM, Krestin GP. Superparamagnetic iron oxide contrast agents: Physicochemical characteristics and applications in MR imaging. Eur Radiol 2001;11:2319–2331. [PubMed: 11702180]
239. Weissleder R, Elizondo G, Stark DD. Superparamagnetic iron oxide: Enhanced detection of focal splenic tumors. Radiology 1990;175(no. 2):489–493. [PubMed: 2326474]
240. Shen T, Weissleder R, Papisov M, Bogdanov A Jr, Brady TJ. Monocrystalline iron oxide nanoparticles (MION): Physiochemical properties. Magn Reson Med 1993;29:599–604. [PubMed: 8505895]

241. Sjogren CE, Johansson C, Naevestad A, Sontum PC, Briley-Saebo K, Fahlvik AK. Crystal size and properties of superparamagnetic iron oxide (SPIO) particles. Magn Reson Imag 1997;15:55–67.

242. Lauffer RB. Paramagnetic metal complexes as water proton relaxation agents for NMR imaging: Theory and design. Chem Rev 1987;87:901–927.

243. M. Gonzales, E. Shapiro, Y. C. Lee, A. Koretsky, and K. M. Krishnan, in preparation.

244. Na HB, Song IC, Hyeon T. Inorganic nanoparticles for MRI contrast agents. Adv Mater 2009;21:2133–2148.

245. Shapiro EM, Koretsky AP. Convertible manganese contrast for molecular and cellular MRI. Mag Reson Med 2008;60:265–269.

246. Tucciarone J, Chuang K, Dodd SJ, Silva AC, Pelled G, Koretsky AP. Layer specific tracing of corticocortical and thalamocortical connectivity in the rodent using manganese enhanced MRI. NeuroImage 2009;44:923–931. [PubMed: 18755280]

247. Hamm B, Staks T, Taupitz M. Contrast enhanced MR imaging of liver and spleen. Reson Imag 1994;4:659–668.

248. Josephson L, Lewis J, Jacobs P, Hahn PF, Stark DD. The effects of iron oxide on proton relaxivity. Magn Reson Imag 1988;6:647–653.

249. Bengele HH, Palmacci S, Rogers J, Jung CW, Crenshaw J, Josephson L. Biodistribution of an ultrasmall superparamagnetic iron oxide colloid, BMS 180549, by different routes of administration. Mag Reson Imag 1994;12:433–442.

250. Harika L, Weissleder R, Poss K, Papisov MI. Macromolecular intravenous contrast agent for MR lymphography: Characterization and efficacy studies. Radiology 1996;198:365–370. [PubMed: 8596833]

251. De Cuyper M, Joniau M. Magnetoliposomes formation and structural characterizations. Eur Biophys J 1988;15:311–319. [PubMed: 3366097]

252. Bulte JWM, Hoekstra Y, Kamman RM. Specific MR imaging of human lymphocytes by monoclonal antibody-guided dextran-magnetite particles. Magn Reson Med 1993;29:32–37. [PubMed: 7678318]

253. Bulte JWM, De Cuyper M, Despres D, Brooks RA, Frank JA. Preparation, relaxometry, and biokinetics of PEGylated magnetoliposomes as MR contrast agent. Magn Mater 1994;194:204–209.

254. Unger E, Needleman P, Cullis P. Gadolinium-DTPA liposomes as a potential MRI contrast agent. Invest Radiol 1988;23:928–932. [PubMed: 3203995]

255. Kabalka GW, Davis MA, Holmberg EG. Contrast enhancement agents for the liver. Mag Res Med 1991;19:406–415.

256. Fritz T, Unger E, Wilson-Sanders S, Ahkong QF, Tilcock AC. Detailed toxicity studies of liposomal gadolinium-DTPA. Invest Radiol 1991;26:960–968. [PubMed: 1835967]

257. Heyn C, Bowen CV, Rutt BK, Foster PJ. Magnetic resonance in medicine. Magn Reson Med 2005;53:312–320. [PubMed: 15678551]

258. Nunn AD, Linder KE, Tweedle MF. Can receptors be imaged with MRI agents? Q J Nuclear Med 1997;41(no. 2):155–162.

259. Romanus E, Hückel M, Groß C, Prass S, Weitschies W, Bräuer R, Weber P. Magnetic nanoparticle relaxation measurement as a novel tool for in vivo diagnostics. J Magn Magn Mater 2002;252:387–389.

260. Gleich B, Weizenecker J. Tomographic imaging using the nonlinear response of magnetic particles. Nature 2005;435:1214–1217. [PubMed: 15988521]

261. Liang, ZP.; Lauterbur, PC. Principles of Magnetic Resonance Imaging. Piscataway, NJ: IEEE Press; 2000.

262. Weizenecker J, Gleich B, Borgert J. Magnetic particle imaging using a field free line. J Phys D: Appl Phys 2008;41:105009.

263. Gleich B, Weizenecker J, Borgert J. Experimental results on fast 2D-encoded magnetic particle imaging. Phys Med Biol 2008;53:N81–N84. [PubMed: 18367783]

264. Weizenecker J, Borgert J, Gleich B. A simulation study on the resolution and sensitivity of magnetic particle imaging. Phys Med Biol 2007;52:6363–6374. [PubMed: 17951848]

265. Roschmann P. Radiofrequency penetration and absorption in the human body: Limitations to high-field whole-body nuclear magnetic resonance imaging. Med Phys 1987;14(no. 6):922–931. [PubMed: 3696080]

266. Ferguson RM, Minard KR, Krishnan KM. J Magn Magn Mater 2009;321:1548–1551. [PubMed: 19606261]

267. Minard KR, Wind RA. Picoliter 1 H NMR spectroscopy. J Magn Reson 2002;154:336–343. [PubMed: 11846593]

268. Minard KR, Wind RA. Solenoidal microcoil design. Part I: Optimizing RF homogeneity and coil dimensions. Concepts Magn Reson 2001;13:190–210.

269. Ferguson RM, Khandhar A, Minard KR, Krishnan KM. Size-optimized magnetite nanoparticles for magnetic particle imaging, in. Proc Int Workshop on MPI. in press.

270. Pellegrino T, Manna L, Kudera S, Liedl T, Koktysh D, Rogach AL, Keller S, Raldler J, Natile G, Parak WJ. Hydrophobic nanocrystals coated with an amphiphilic polymer shell: A general route to water soluble nanocrystals. Nano Lett 2004;4(no. 4):703.

271. Yu WW, et al. Nanotechnology 2006;17:4483.

272. Khandhar A, Ferguson M, Krishnan KM. Characterization of hydrophobic magnetite nanoparticles coated with amphiphilic polymers: A standardized approach to designing nanoparticles for biomedical applications. Biomaterials. submitted for publication.

273. Chieh JJ, Yang SY, Jian ZF, Wang WC, Horng HE, Yang HC, Hong CY. Hyper-high-sensitivity wash-free magnetoreduction assay on biomolecules using high- T_c superconducting quantum interference devices. J Appl Phys 2008;103:014703.

274. Baselt DR, Lee GU, Natesan M, Metzger SW, Sheehan PE, Colton RJ. A biosensor based on magnetoresistance technology. Biosens Bioelectron 1998;13:731. [PubMed: 9828367]

275. Edelstein RL, Tamanaha CR, Sheehan PE, Miller MM, Baselt DR, Whitman LJ, Colton RJ. The BARC biosensor applied to the detection of biological warfare agents. Biosens Bioelectron 2000;14:805. [PubMed: 10945455]

276. Osterfeld SJ, Yu H, Gaster RS, Caramuta S, Xu L, Han SJ, Hall DA, Wilson RJ, Sun S, White RL, Davis RW, Pourmand N, Wang SX. Multiplex protein assays based on real-time magnetic nanotag sensing. Proc Nat Acad Sci 2008;105(no. 52):20637. [PubMed: 19074273]

277. Safarik I, Safarikova M. Use of magnetic techniques for the isolation of cells. J Chromatography B 1999;722:33.

278. Watson JHP. Magnetic filtration. J Appl Phys 1973;44:4209.

279. Gijs MAM. Magnetic bead handling on-chip: New opportunities for analytical applications. Microfluid Nanofluid 2004;1:22.

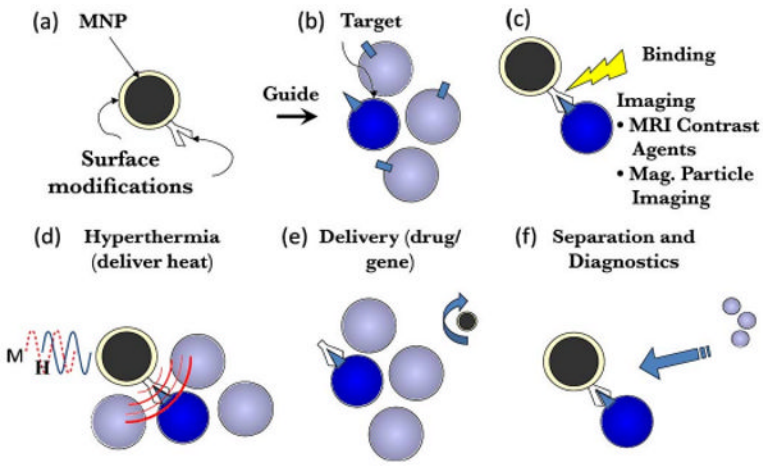

Fig. 1.

Magnetic nanoparticles in biomedicine. (a) Prior to use, the surface of the magnetic nanoparticles must be modified to provide both biocompatibility and functionality (specific binding and targeting moieties). (b) They can then be guided to the targeting location either using tailored magnetic field gradients or by injecting into the appropriate vasculature. (c) After localization at the target, the magnetic properties of the particles provide novel functionality. This could be as contrast agents for established imaging methods such as MRI or the development of new imaging modalities such as Magnetic Particle Imaging. (d) The dynamic relaxation of the nanoparticles, when subject to an alternating magnetic field can be used for therapeutics (hyperthermia), imaging (magnetic particle imaging) or diagnostics (biosensing). (e) The functionalized molecule on the surface could be a drug that can be released in response to external stimuli such as pH, temperature or an alternating magnetic field. (f) Moving the particles with magnetic field gradients allows for magnetic targeting, delivery and *in vitro* separations and diagnostics; the latter can be effective in ultra-immunoassays where only small quantities of blood (such as in infants) can be drawn to concentrate the signal.

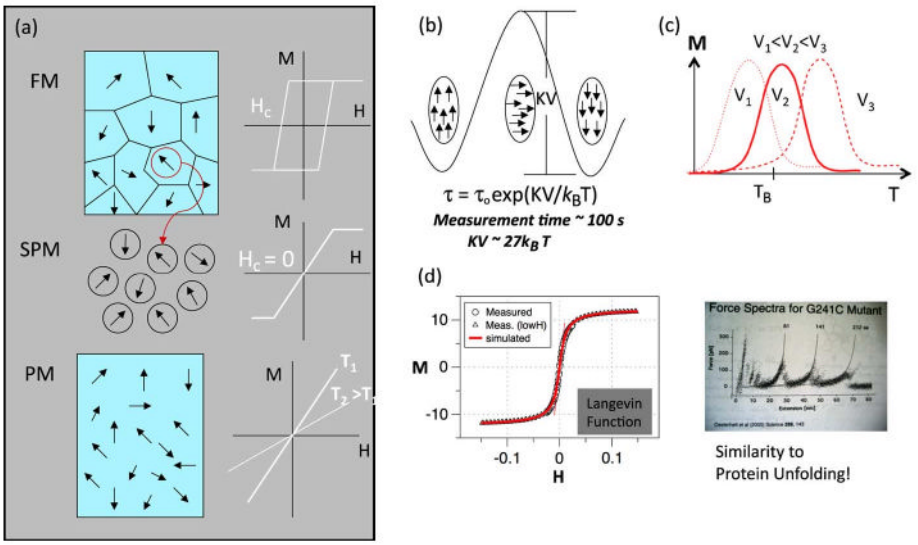

Fig. 2.

(a) Materials show a wide range of magnetic behavior. At one end are the non-interacting spins in paramagnetic materials (bottom) characterized by a linear susceptibility that is inversely dependent on the temperature (Curie law). At the other end, we have ferromagnetic materials (top), characterized by exchange interaction, hysteretic behavior and a finite coercivity, H_c. If we now reduce the size of the ferromagnetic material we may ultimately reach a size where thermal energy ($k_BT = 4 \times 10^{-21}$ J, at 300 K) can randomize the magnetization, such that when there is no externally applied field the magnetization measured in a finite time interval (typically, 100 s) is zero. Such materials show no coercivity and behave as paramagnets with a large moment, or as superparamagnets. (b) The randomization of the magnetization takes place by excitation over an energy barrier given by the product of the anisotropy constant, *K*, and the volume, *V*. Note that the relaxation time, τ, depends exponentially on the energy barrier, *KV*, and hence to reproducibly control the magnetic behavior of superparamagnetic nanoparticles, narrow size distributions are required. (c) Superparamagnetic nanoparticles are defined in terms of a characteristic size, D_{sp}, or a characteristic temperature called the blocking temperature, T_B, such that, for a given measurement time, a sharp division from superparamagnetic to ferromagnetic behavior can be observed. (d) The magnetic response, M (*H*), characteristic of a superparamagnetic material is described by Langevin functions. The M.(*H*) data is for magnetite particles prepared for magnetic particle imaging (Section VI-E) and also shows the good fit of the data to the Langevin function. Note that the Langevin function is also used to describe the force-displacement behavior of proteins and the protein unfolding dynamics [33] of importance in biology. This is because both phenomena arise from energy barriers and classical statistical mechanics.

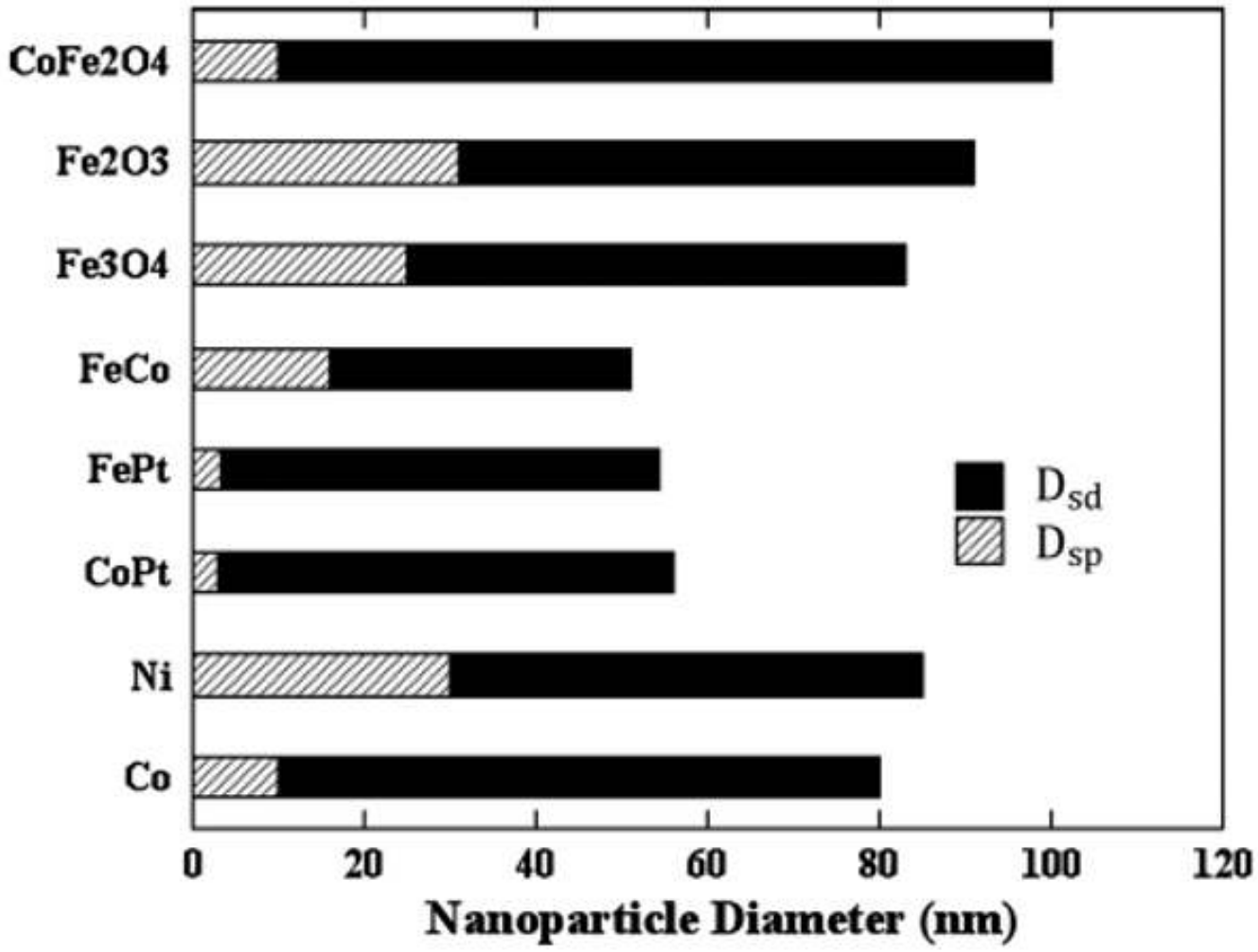

Fig. 3.

On the nanometer length scale magnetic materials, at a given temperature, show distinctly different behavior as a function of size; most noticeably, this is observed in nanoparticles. For diameters, $D < D_{sp}$, they exhibit superparamagnetism; for $D > D_{sd}$, they split into multiple domains to minimize their overall energy and in between, $D_{sp} < D < D_{sd}$, they are ferromagnetic *and* single domain. These characteristic sizes depend on their intrinsic properties (saturation magnetization, M_s, anisotropy constant, K, and exchange stiffness, A) and can easily be calculated. Critical sizes for the observation of superparamagnetism, D_{sp} and single-domain, D_{sd} behavior in a variety of common ferromagnetic fine particles are shown. A measurement time of 100 s is assumed in all cases.

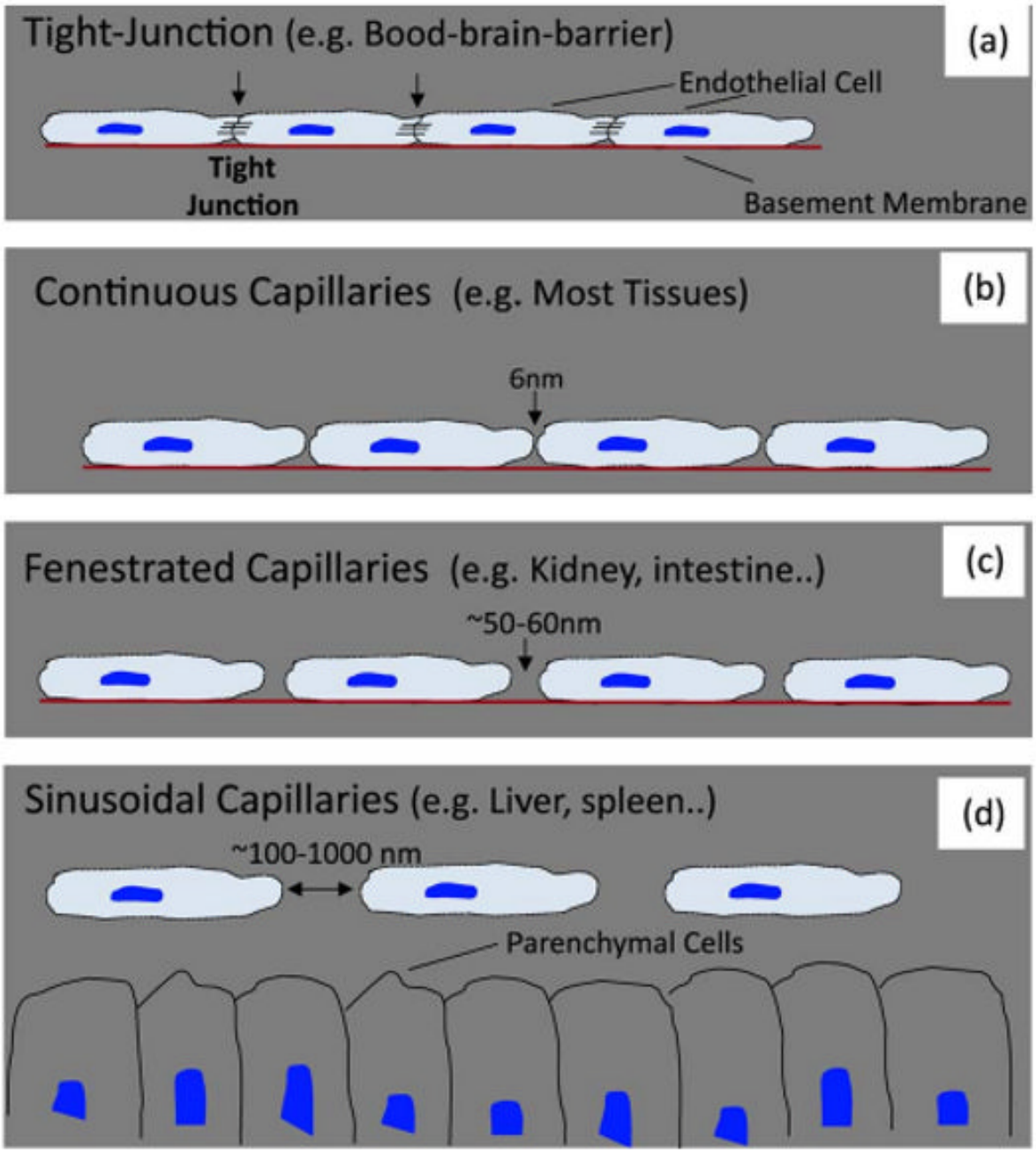

Fig. 4.

Different classes of blood capillaries. (a) Tight-junction capillaries found in the blood-brain-barrier (BBB). The "gaps" between the endothelial cells are extremely small; in many ways this is how the brain protects itself against infection. On the other hand, penetration of the BBB may be possible with extremely small (~2 nm) nanoparticles. (b) Continuous capillaries found in most tissues; (c) fenestrated capillaries, includes kidney, intestine and some endocrine and exocrine glands; (d) sinusoidal capillaries include liver, spleen and bone marrow. The last two are part of the filtration system where the kidneys remove objects below a certain size (~50 nm) and the liver/spleen prevent objects than a certain size from circulation, thus setting both

an upper and lower bound. Note that, if the nanoscale magnetic package is less than 50 nm it can be passively targeted to the kidney. Adapted from Okuhata (1999) [48].

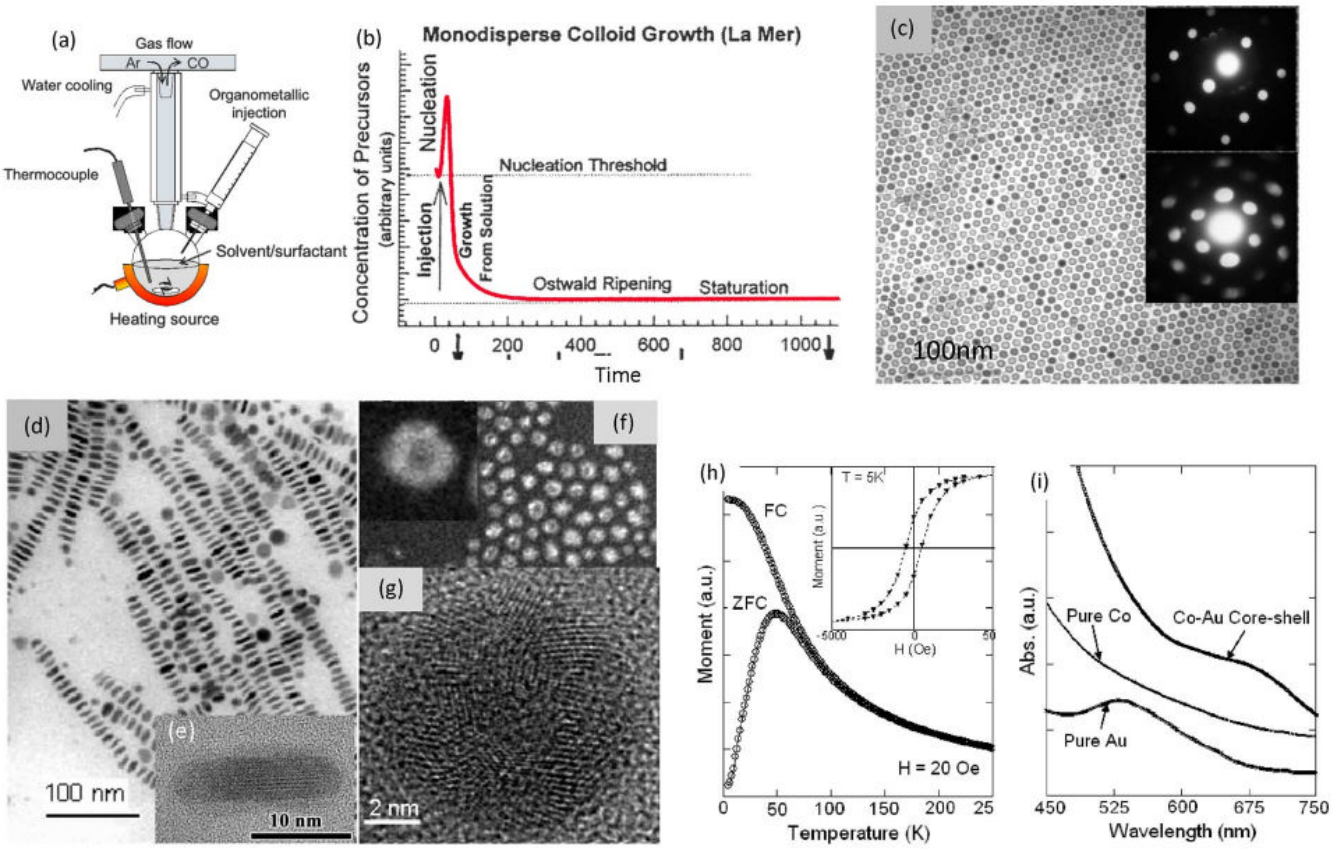

Fig. 5.

(a) The La Mer synthesis of nanoparticle by injecting metal-organic precursors in a coordinating solvent containing surfactants. (b) This causes a temporally discrete nucleation event and under appropriate conditions, is followed by size-selective focused growth. As a result, highly monodisperse nanoparticles are produced (figure from Murray, Norris and Bawendi, JACS, 1993). (c) Spherical ε – Co nanocrystals; inset shows SAD patterns (d) hcp cobalt nanodisks; (e) inset shows a HREM micrograph with the basal plans (*c*-axis) normal to the nanodisks. The shape anisotropy prefers their magnetization in plane while the magnetocrystalline anisotropy favors a magnetization normal to the plane of the disks. (f) 9 nm diameter $Co_{core}Au_{shell}$ nanoparticles: z-contrast TEM image, (g) high resolution TEM image showing heterogeneous nucleation of multiple Au grains around the Co core; (h) ZFC/FC magnetic measurements of $Co_{core}Au_{shell}$ nanoparticles, inset 5 K hysteresis; (i) UV-visible spectra showing a characteristic optical signature, i.e., a shift in the Au absorption towards the infrared when compared to pure gold nanoparticles.

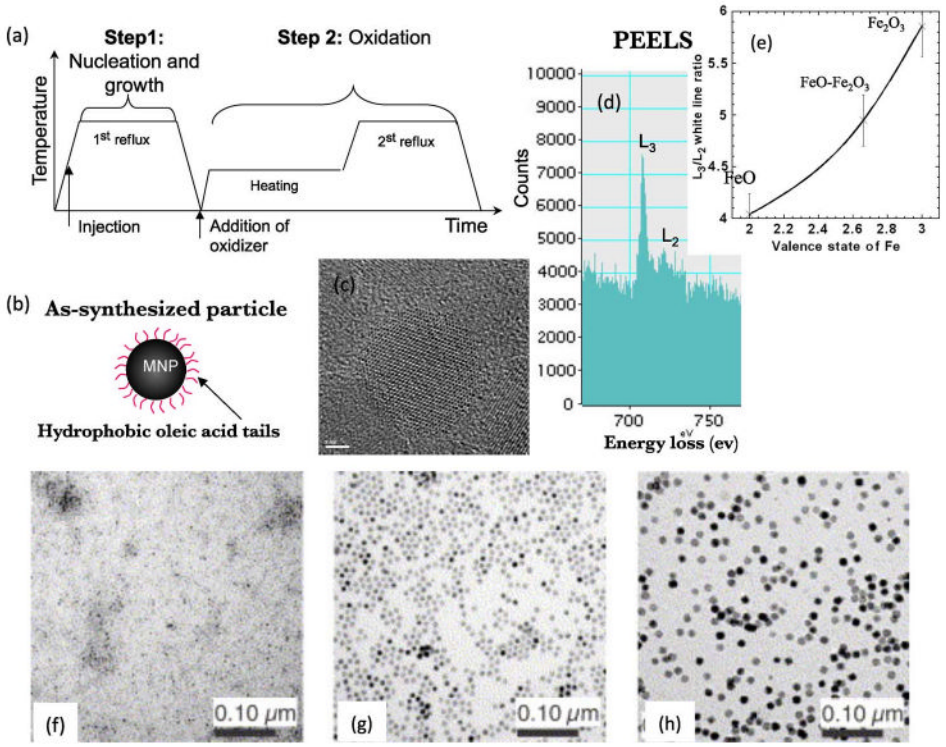

Fig. 6.

(a) Synthesis of magnetite is a two-step process: first Fe nanoparticles are synthesized and then subsequently oxidized to form Fe_3O_4. (b) The as-synthesized particles are coated with a layer of surfactant (oleic acid) making them hydrophobic but stable in non-polar solvents. (c) HREM micrograph confirms the synthesis of high quality, defect free nanocrystals. (d) An electron energy loss spectrum. (e) The ratio of the Fe L_3/L_2 edges is ~4.8 and corresponds to Fe_3O_4 (magnetite) [92]. Magnetite nanoparticle size shown as a function of molar ratio of oleic acid to iron pentacarbonyl; (f) 2 nm particles made in a 1:1 synthesis (g) 7 nm particle made in 2:1 synthesis (h) 11 nm particles made in a 3:1 synthesis [93].

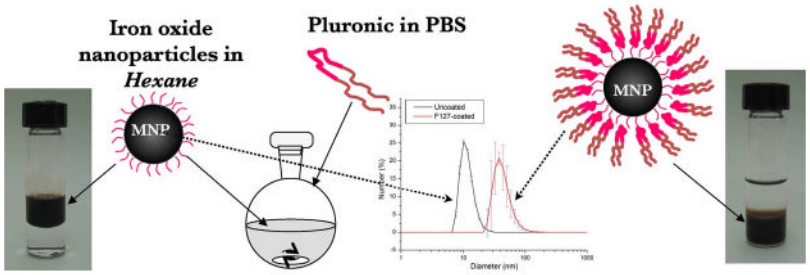

Fig. 7.

Dynamic Light Scattering (DLS) measurements of 9 nm diameter magnetite particles before (left/black) and after (right/red) coating with Pluronic F127. The configuration of the coated particle is also shown. The coating of pluronic is ~ 23 nm and the equivalent increase in the hydrodynamic volume of the nanocrystals is confirmed by the DLS measurement.

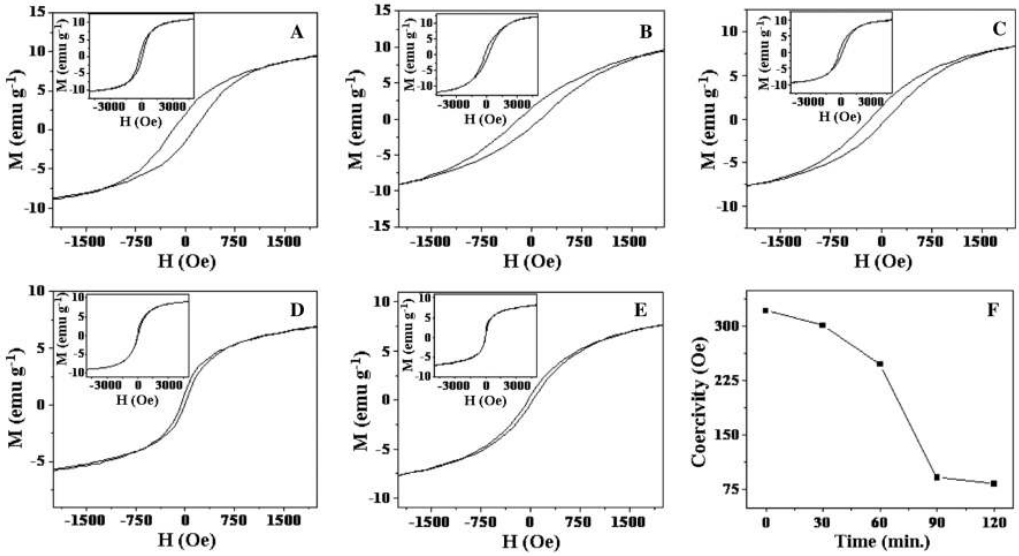

Fig. 8.

(a)–(e) show the magnetization vs. field (*M* vs. *H*) hysteresis loops at 300 K for Co@Au reaction mixture in the displacement reaction at time 0, 30, 60, 90 and 120 min, respectively. The insets of all the main figures (a)–(e) show the hysteresis curves at full scale of the high field region at 300 K. (f) Shows the plot of coercivity (H_C) measured from the hysteresis loops of figures (a)–(e) vs. time (T).

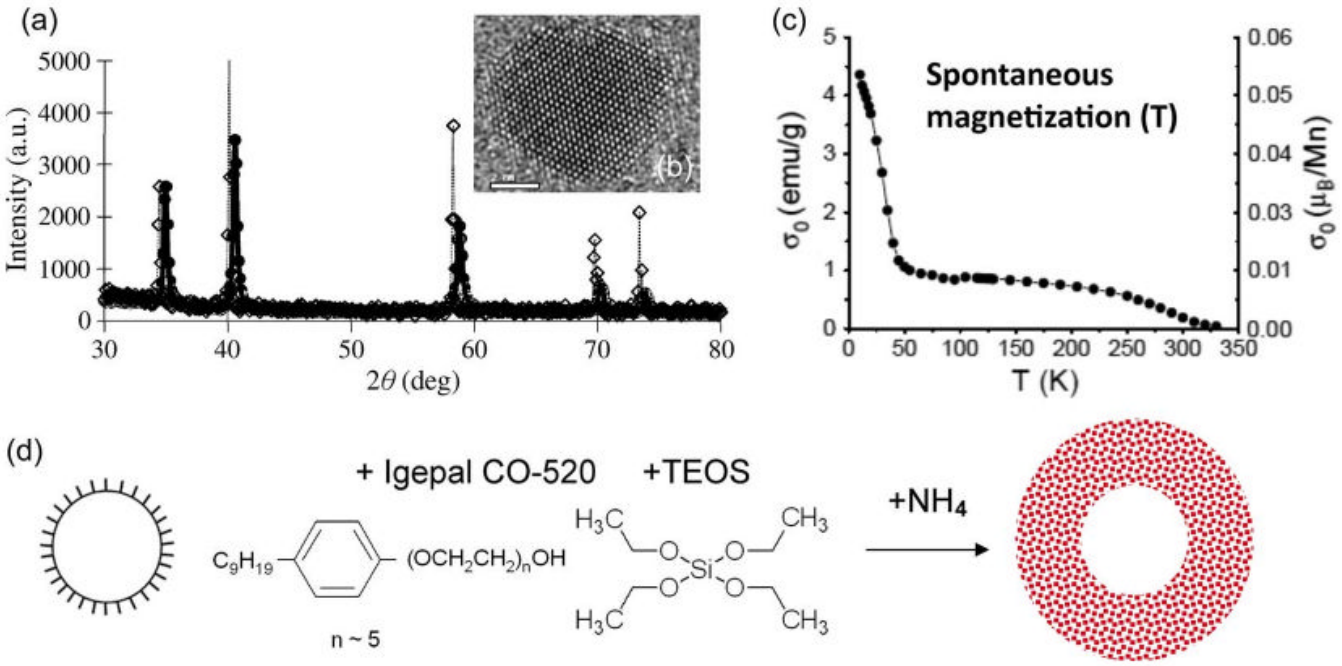

Fig. 9.

(a) X-ray $\theta - 2\theta$ scan from bulk and nanoparticles of MnO. Note that the Bragg peaks from the nanoparticles have larger 2θ than for the bulk, indicating a smaller lattice parameter. (inset) A high-resolution electron micrograph showing a defect free MnO nanoparticle, ~10 nm in diameter. (b) The temperature dependence of the spontaneous magnetization showing that the MnO nanoparticles are ferromagnetic up to ~300 K and (c) synthesis of MnO nanoparticles with a silica shell of controlled thickness.

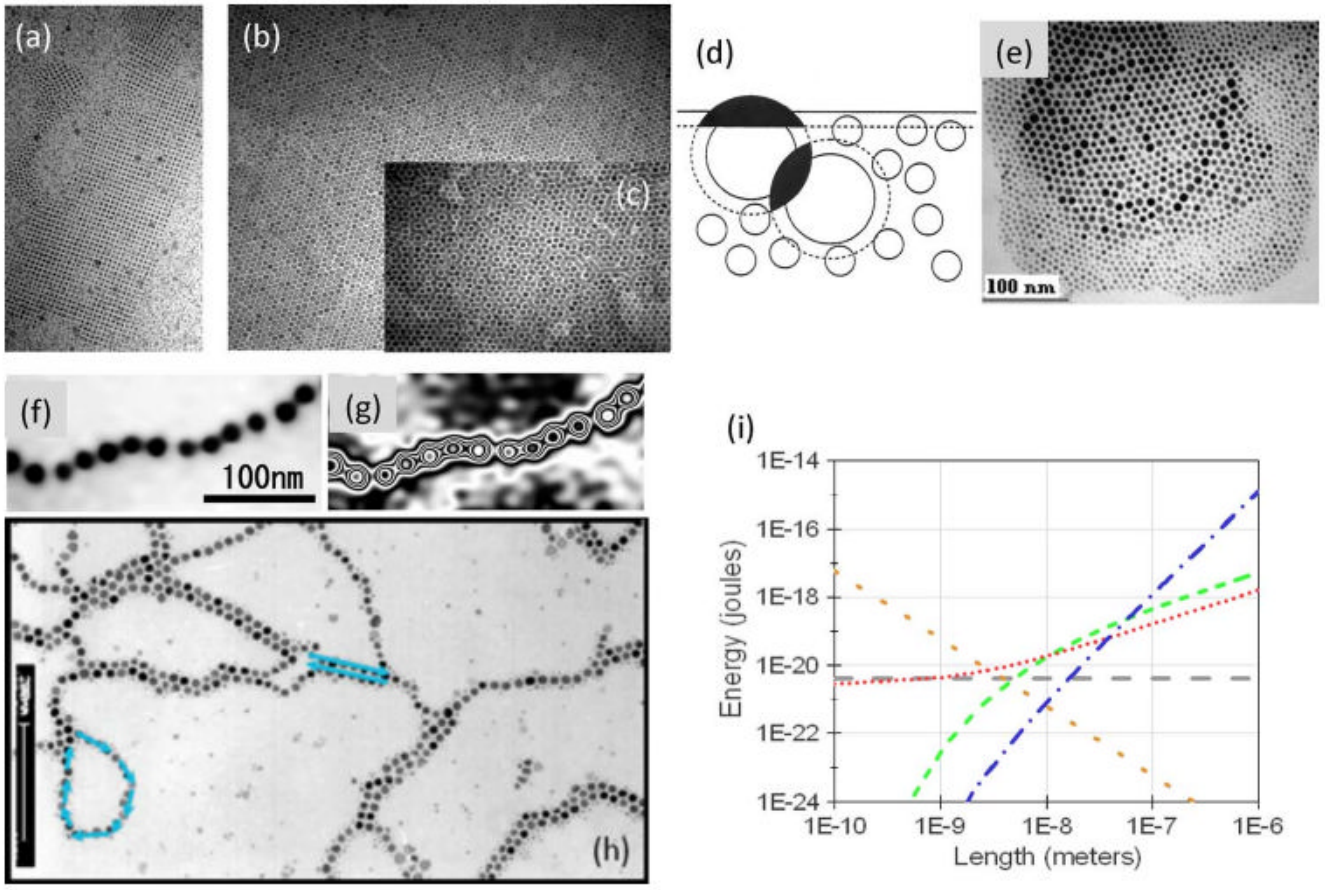

Fig. 10.

Self-assembly of cobalt nanoparticles by the controlled evaporation of the solvent as a function of nanoparticle size: (a) 4 nm, (b) 9 nm, 1 monolayer, (c) 9 nm, 2 monolayers. (d) Schematic representation of nanoparticles with a bimodal size distribution. When large particles touch each other or when they wet the surface first, additional volume (shown in black) is available elsewhere for the small particles to occupy and increase their vibrational entropy. Such entropy-induced wetting is a result of a fictitious displacement force. (e) Experimental verification of (d) using a bimodal distribution of 4 nm and 9 nm Co particles. (h) Larger particles are ferromagnetic and to minimize the magnetostatic energy they form closed loops and chains. (f) & (g) These can be experimentally verified by electron holography measurements. (i) The energies of all these self-assembly processes converge to the value of k_BT ($\sim 10^{-21}$ J) at room temperature. Hence, change in a single parameter (size) can give rise to an interesting array of self-assembly behavior [133].

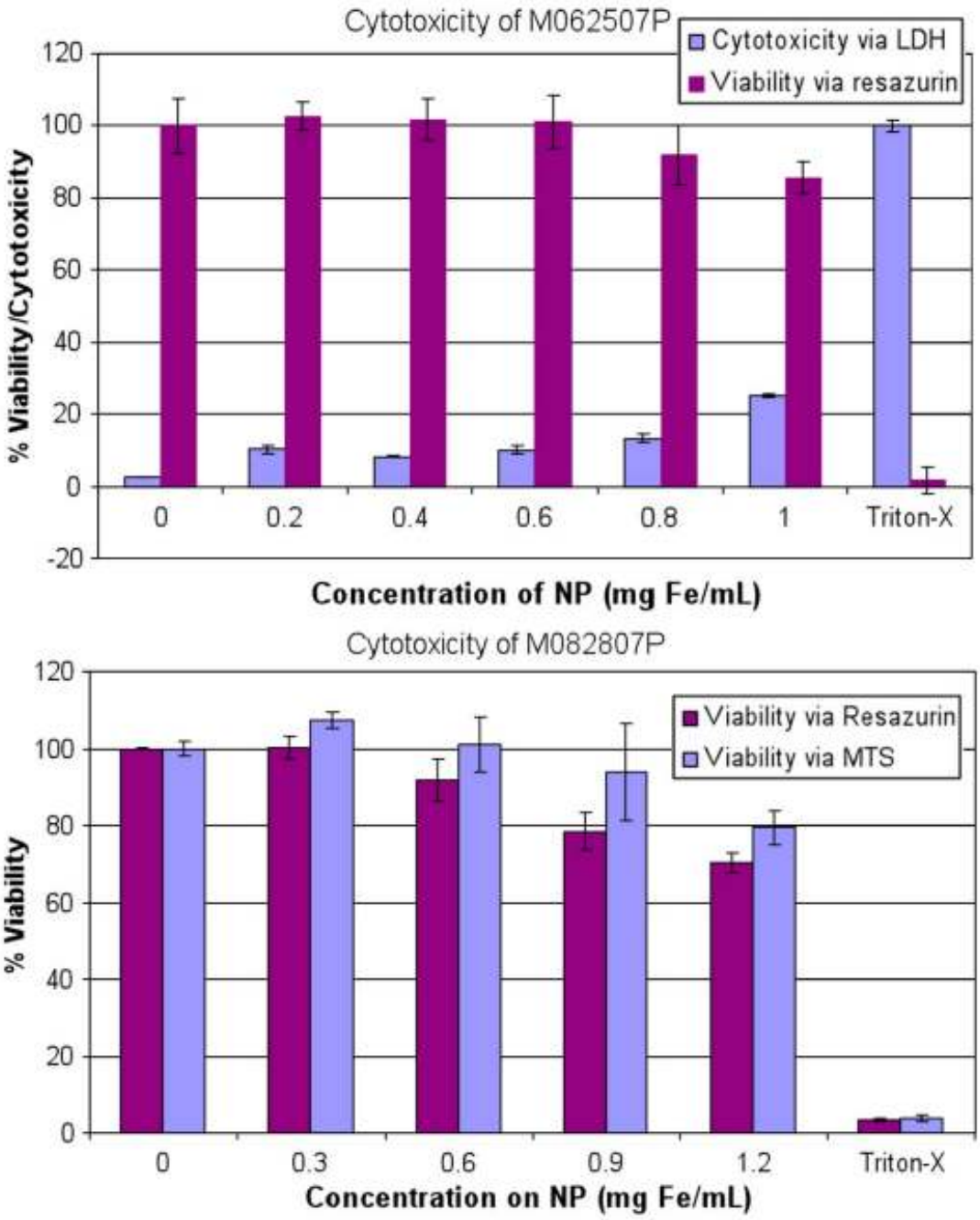

Fig. 11.

(left) Assays for viability with resazurin and cytotoxicity with LDH and (right) viability with resazurin and MTS assays. Results are for Pluronic F127 coated magnetite nanoparticles, 10 nm in diameter.

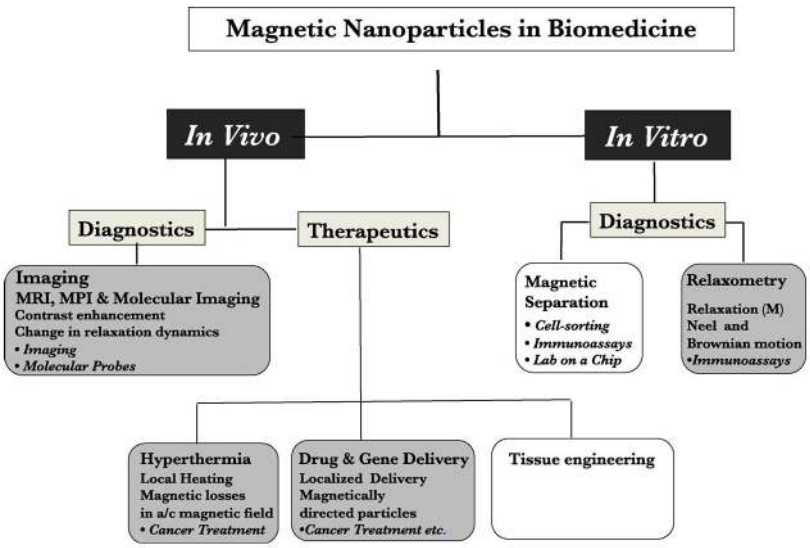

Fig. 12.

Magnetic nanoparticles in biomedicine broadly classified as *in vitro* and *in vivo* applications in diagnostics/imaging and therapeutics. Only the four highlighted topics, deriving from our own work, are discussed in Section VI of this paper.

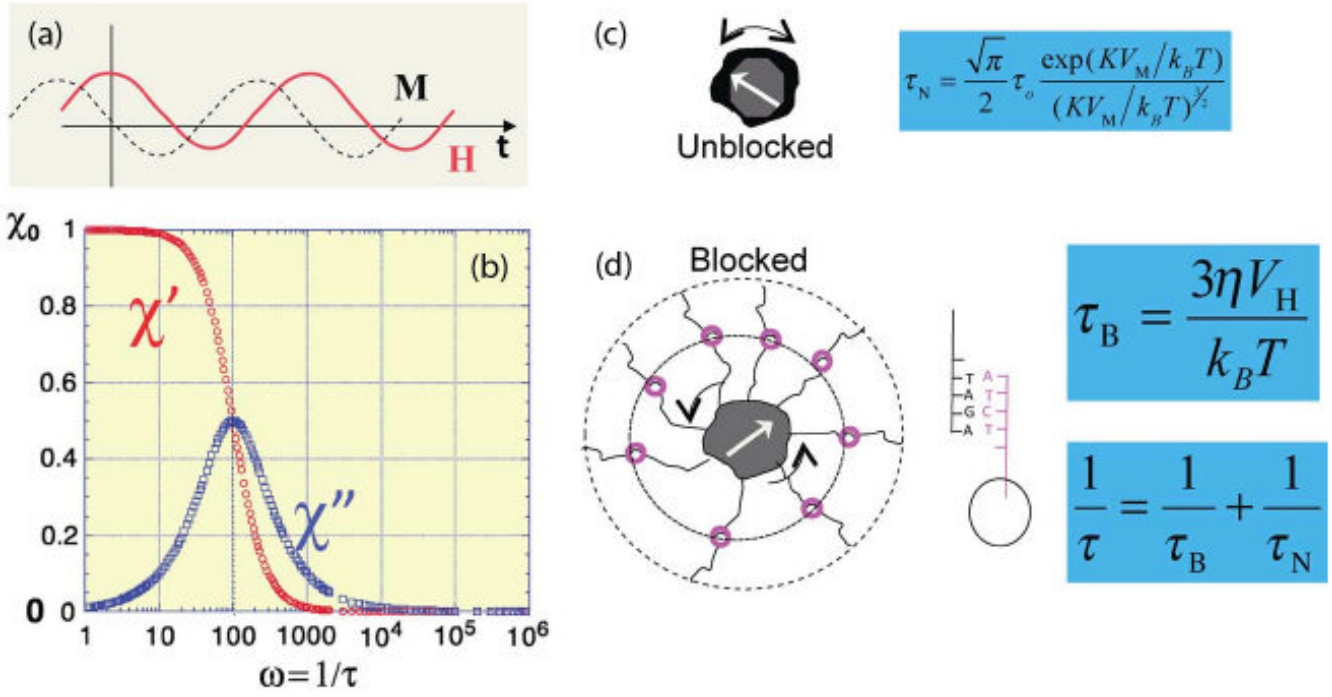

Fig. 13.

Response of magnetic nanoparticles to an ac field. (a) The magnetization, M, lags in phase behind the applied field, H. (b) The real part, χ', or the in-phase component and the imaginary part, χ'', or the loss component of the susceptibility as a function of frequency, v. Note that χ'' is a maximum when the angular frequency $\omega(=2\pi v) = 1/\tau$ where τ is the relaxation time. (c) In unblocked nanoparticles, the relaxation is achieved by Néel rotation of only the magnetic moment and (d) in larger, blocked particles the relaxation is through the physical Brownian rotation of the entire particles. Now the relaxation time depends on non-magnetic parameters such as the viscosity,η, of the medium and the hydrodynamic volume, V_H. The latter is sensitive to specific binding and changes in τ_B with size (V_H) can be used as a diagnostic method for specific binding assays. For example the nanoparticle can be functionalized for antibody-antigen or complementary-DNA (shown) detection.

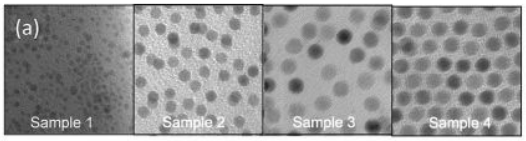

Sample	D_{TEM} (nm)	D_{Chantr} (nm)	σ	Conc. (m%)	χ_o
1	5	4.6	0.075	0.202	0.93
2	10	8.5	0.15	0.283	4.96
3	14	11.2	0.21	0.0867	12.31
4	12.8	9.6	0.22	0.252	7.98

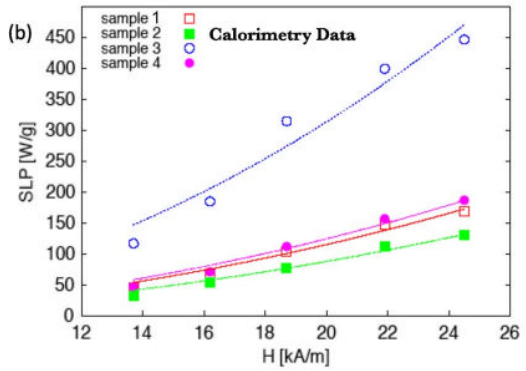

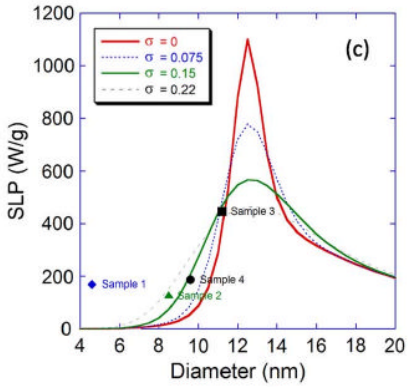

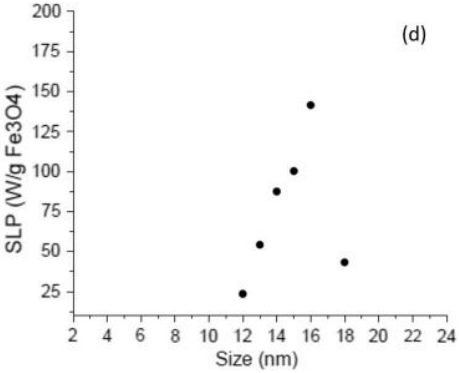

Fig. 14.

(a) Magnetite nanocrystals of four different sizes were used in this experiment. Table shows the sizes measured by TEM and from fittings of the magnetization curves to yield, D_{Chant} and a size distribution, σ, based on the assumption of a log-normal size distribution. (b) Specific loss power vs. ac-field amplitude at a frequency of 400 kHz. (c) SLP as a function of particle size for $H_0 = 24.5$ kA/m. Plots are calculated for various polydispersity indexes. SLP of samples 1–4 are plotted for comparison with theoretical values. (d) A more recent measurement [212] using a dedicated, commercial [213] hyperthermia measurement system and an optical pyrometer, shows a clear peak in the SLP as a function of particle size. The data is measured for Fe_3O_4 nanoparticles, at a frequency of 376 kHz and field amplitude of 14 kA/m.

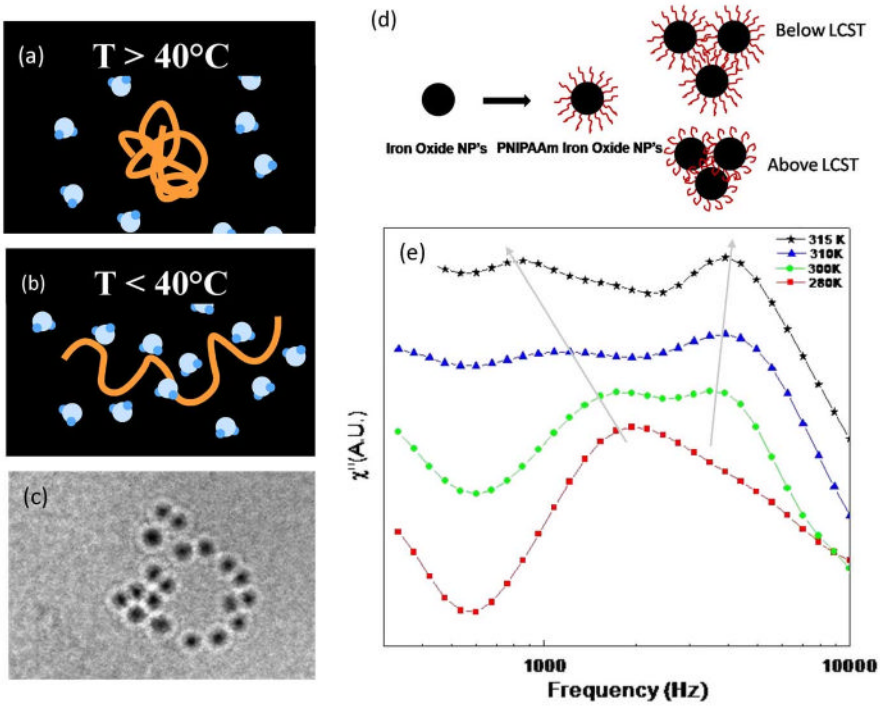

Fig. 15.

A typical temperature sensitive polymer, p-NIPAAM shows a conformal change at a critical temperature, LCST. For example, (a) at T > LCST(= 40°C) the polymer is collapsed but (b) is open at T < LCST. (c) p-NIPAAM functionalized magnetite nanoparticles. (d) Pictorial representation of the behavior of p-NIPAAM functionalized magnetite nanoparticles below and above LCST. Note that when the p-NIPAAM collapses for T > LCST the nanoparticles become less hydrophilic and agglomerate. (e) The physical change in size can be monitored by ac susceptibility measurements. The peak at higher frequency shifts to larger values with increasing temperature corresponding to the shrinking of the nanoparticle V_H; however, the particles now become hydrophobic and then agglomerate as reflected in the emerging peak at lower frequencies.

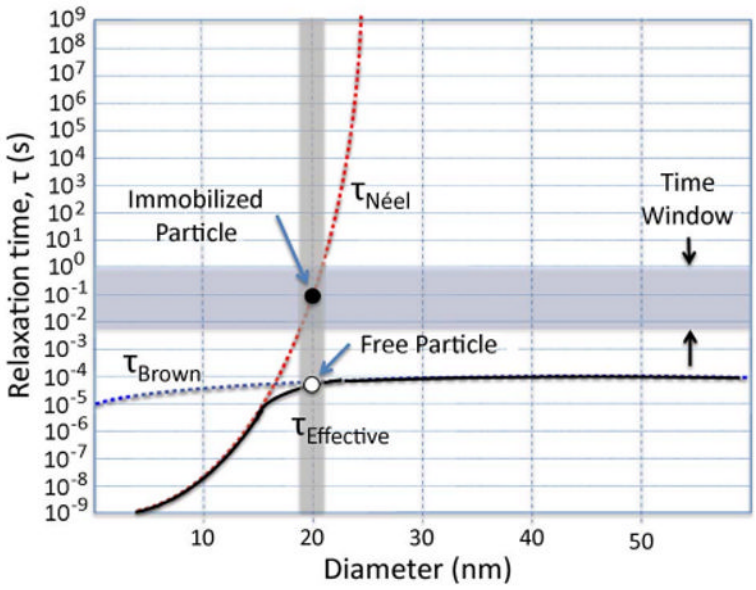

Fig. 16.

The dependence of the Brownian, Néel and effective relaxation time on the particle diameter. The time window is set by the measurement. A coating thickness of 15 nm, anisotropy constant, $K = 20$ kJ/m^3 and T = 300 K is assumed. (Adapted from Kotitz *et al.*) [230].

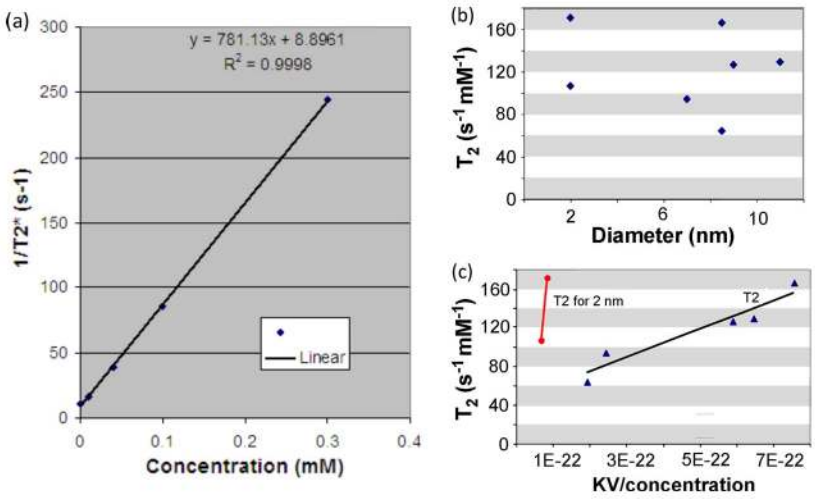

Fig. 17.

(a) Linear dependence of the relaxivity with the concentration of contrast agents (magnetite, 9 nm diameter) (b) relaxivity ($mM^{-1}s^{-1}$) of monodispersed, ferrimagnetic iron oxide nanoparticles as a function of size; note that there is no obvious scaling with size (c) relaxivities (same data) scale linearly as a product of anisotropy constant and the volume.

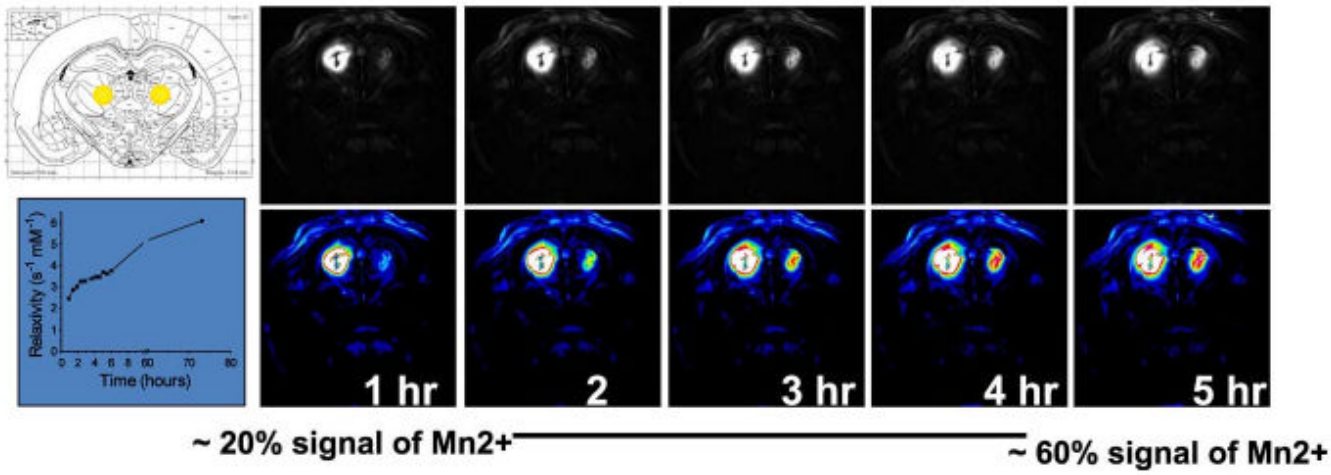

Fig. 18.

The stereotactic atlas represents where the particles were injected. (Top-left corner) The yellow spots are the expected injection sites, which are ventral posteromedial thalamic nuclei (VPM). The relaxivity change with time plot shows that Mn^{2+} was released from MnO@SiO_2 in the acetate buffer solutions (pH 5.0). (Bottom-left corner) The right part of this figure shows the *in vivo* signal intensity change with time. Spots in the right side of images are the injection sites of MnO@SiO_2 particles and left side are the control $MnCl_2$ solutions. It clearly shows that particles slowly dissolved and the signal intensity increased with time.

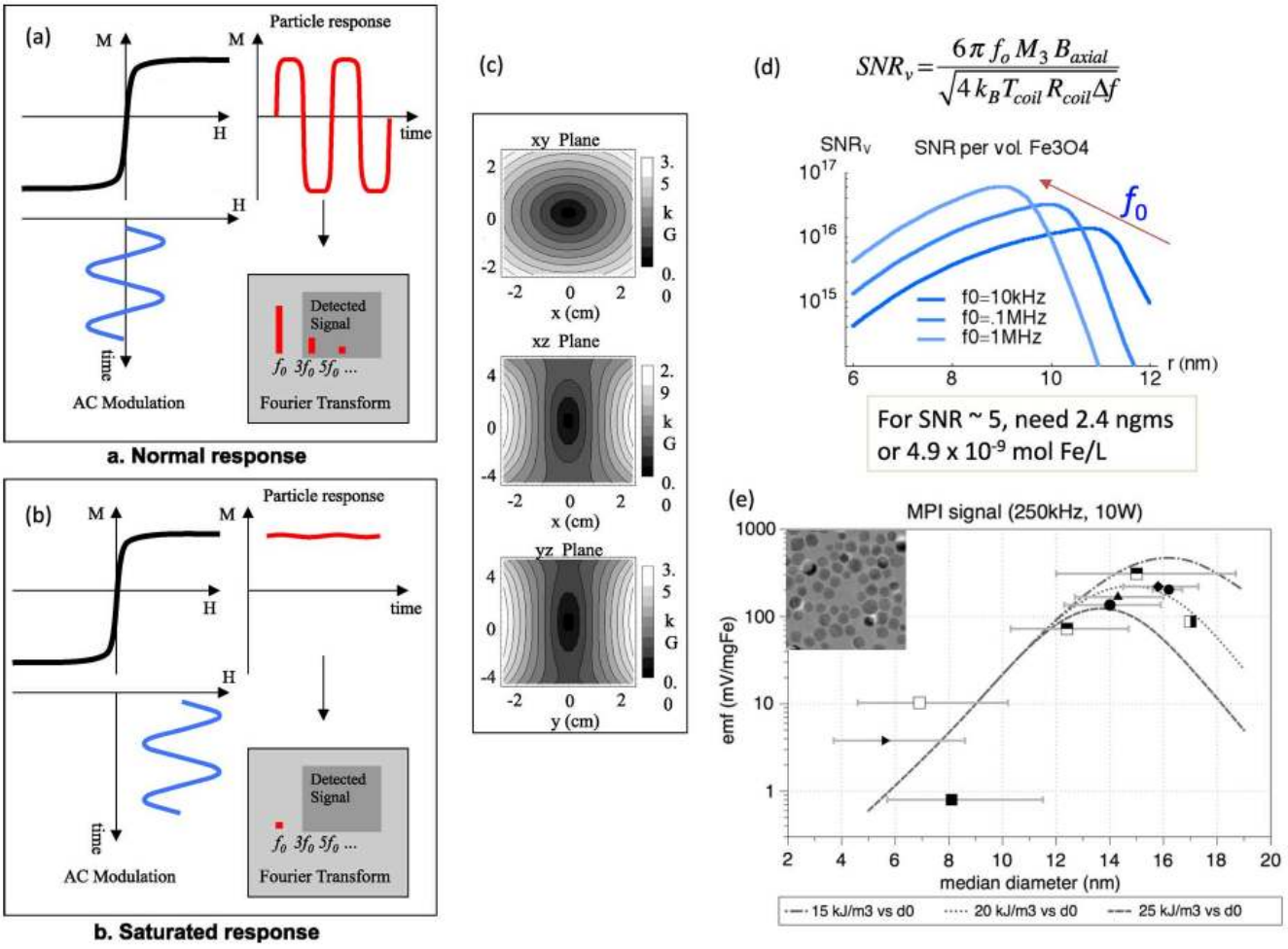

Fig. 19.

Response of magnetic particles to external magnetic field. (a) Normal response to an oscillatory, AC modulation field. (b) Saturated response when a static field, H_A is superimposed on the AC modulation field. Now, the strong harmonics arising from the non-linear response, observed earlier in (a), are suppressed. (c) An assembly of permanent magnets designed to apply the selection field. A single point is space is designed to be the zero field point. (d) MPI performance for magnetite NMPs. K is fixed at 25 kJ/m^3: SNR per volume of magnetite, plotted as a function of nanoparticle size at several drive frequencies (f_o). (e) Experimental MPI performance for magnetite NMP samples of increasing size showing a maximum signal at 15 nm diameter. Also shown are several simulated curves for different K values, with experimental data most closely matching $K \sim 20$ kJ/m^3.

TABLE I

Relaxivities ($mMol^{-1}s^{-1}$) of Our Nanoparticles as a Function of Size With Comparison to Three Commercially Available Iron Oxide Formulations: Combidex, Feridex and Bangs. Note the Excellent Performance Overall and Especially Those of the 2 nm Particles, Which May Be Able to Penetrate the Blood-Brain-Barrier [243]

	Fe_3O_4 (2nm)	Fe_3O_4 7 nm	Fe_3O_4 11 nm	Fe_3O_4 15 nm	Combidex	Feridex (Endorem)	Bangs
R_1	0.63	1.39	0.5	0.268	1.27	2.61	1.63
R_2	209.8	269.0	348.0	313.7	79.1	166.8	78.9
R_2*	354.3	880.0	671.9	466.3	93.9	247.5	380.4

TABLE II

A: Comparison of Different Biomedical Imaging Methods (Modified From Massoud and Gambhir [16])

	Radiation Used	Spatial Resolution	Temporal Resolution	Sensitivity	Quantity of contrast agent used	Summary / Comments
Positron Emission Tomography (PET)	High Enery γ-rays	1-2 mm	10sec to minutes	10^{-11}-10^{-12} Mole/L	Nanograms	Sensitive Quantitative Needs cyclotron
Single Photon Emission Tomography	Low Energy γ-rays	1-2 mm	minutes	10^{-10}-10^{-11} Mole/L	Nanograms	Many available probes
Computed Tomography	X- rays	50-200 μm	minutes	Not well characterized	Not Applicable	Good for bone, tumor but nor for soft tissues
Magnetic Resonance Imaging (MRI)	Radiowaves	25-100μm	Minutes to hours	10^{-3}-10^{-5} Mole/L	Micrograms to Milligrams	Highest resolution; Morphological and functional imaging Low sensitivity Slow
Magnetic Particle Imaging (MPI)	**Radiowaves**	200-500 μm	Seconds to minutes	10^{-11}-10^{-12} Mole/L	Nanograms	**Quantitative Good sensitivity Fast Good resolution No tissue contrast**